Atomistics of Dislocation Mobility in Silicon: Core Structure and Mechanisms

by

João F. Justo Filho

Submitted to the Department of Nuclear Engineering
in partial fulfillment of the requirements for the degree of

Doctor of Philosophy

at the

MASSACHUSETTS INSTITUTE OF TECHNOLOGY

June 1997

Author .....
Department of Nuclear Engineering
February 25, 1997

Certified by.....
.....
Sidney Yip
Professor of Nuclear Engineering
Thesis Supervisor

Certified by....
.....
Vasily V. Bulatov
Research Associate of Mechanical Engineering
Thesis Supervisor

Accepted by.....
.....
Efthimios Kaxiras
Reader, Professor of Physics - Harvard University

Accepted by.....
.....
Jeffrey P. Freidberg
Chairman, Departamental Committee on Graduate Students

Atomistics of Dislocation Mobility in Silicon: Core Structure and Mechanisms

by

João F. Justo Filho

Submitted to the Department of Nuclear Engineering
on February 25, 1997, in partial fulfillment of the
requirements for the degree of
Doctor of Philosophy

Abstract

The mobility of partial dislocations in the {111} glide set of silicon is studied using empirical potentials combined with atomistic simulations. Using a new empirical potential, this study focuses on several mechanisms of kink and jog motion of partial dislocations.

To study mechanisms of kink motion, a new empirical potential for silicon is developed, which provides a considerable improvement over existing empirical models in describing local structures. The model comprises of a two- and three-body expansion and incorporates the chemical and physical trends of bonding as local coordination changes. This is done by including coordination dependent terms in both the two- and the three-body interactions. The parameters are fitted to a large database of *ab initio* calculations, including bulk and defect properties. For dislocations, which are not explicitly included in the database, the new potential gives a full description of core properties of partial dislocations, while no other empirical model is able to provide such description. It correctly describes the core reconstruction of both 30°- and 90°-partial dislocations, and anti-phase defects (APD).

This new model, combined with energy minimization methods, is used to study the glide mechanisms of partial dislocations. The work focuses on the atomistic processes of kink creation and propagation of 30°- and 90°-partial dislocations for both reconstructed and unreconstructed configurations. The role of core effects in dislocation mobility is revealed by the comparison between the formation and migration energies between these two situations. For an unreconstructed dislocation the activation energy for the dislocation motion is considerably smaller than the one for a reconstructed dislocation for both the 30°- and 90°-partials. Therefore, the unreconstructed bonds ease the motion of a dislocation. The study of the interaction of kinks with anti-phase defects shows that the APD's play an important role in the mechanisms of kink motion. These defects bind with the kinks and change the kinetics of the kink motion. For 30°-partial dislocations, we find an intrinsic asymmetry between

the kinks forming a double kink (DK). Each type of kink (in this DK) has a different structure and consequently a different formation energy and mobility.

The process of intersection of a mobile dislocation with a static forest dislocation is examined in full atomistic detail in silicon using atomistic simulations. The formation of defects (kinks and jogs) in the dislocations is observed as result of strong core-core interactions, and such defects start to form even before the geometrical point of intersection. This picture of intersection provides information about the relevant atomistic mechanisms involved in the intersection. For example, core reconstruction is found to play an important role in the process. Methodologically, this study demonstrates the feasibility of obtaining key parameters of dislocation forest interactions, including energy barriers for forest cutting.

Thesis Supervisor: Sidney Yip
Title: Professor of Nuclear Engineering

Thesis Supervisor: Vasily V. Bulatov
Title: Research Associate of Mechanical Engineering

Acknowledgements

I would like to express my gratitude to all those who contributed to this thesis work. I am thankful to Prof. Sidney Yip who was always source of inspiration and guidance. He introduced me to the exciting field of atomistic simulations and not only helped in developing this thesis but also taught me how to be a scientist. I am thankful to Dr. Vasily Bulatov who guided me through all phases of the development of this thesis. His help and interest was fundamental in this work. I am grateful to Prof. Ali Argon for serving in my thesis commitee, for helpful discussions, and insightful suggestions. I am grateful to Prof. Efthimios Kaxiras from Harvard University for his collaboration on this research and for serving in my thesis commitee.

I would like to acknowledge the financial support from Brazilian Agency Conselho Nacional de Desenvolvimento e Pesquisa (CNPq) and Center for Materials Science and Engineering (CMSE-MIT).

I am thankful to all the friends and colleagues. Thanks to Dr. Lisa Porter, Li Ju, and Martin Bazant (Harvard) for discussions and suggestions. Thanks to my friends Anacleto Figueiredo, Lucy Assali, and Welles Morgado.

I am deeply indeped to my parents for their encoragement and support all the way in my studies. This thesis is dedicated to my wife Silvia Brunini, for her love, continuous support, encouragement, and help in this work.

Contents

1 Introduction **13**

1.1 Motivation and Background 13

1.2 Problem Statement and Scope of the Thesis 15

2 Introduction to Dislocations **19**

2.1 Dislocations and Plasticity 19

2.2 Dislocations in Semiconductors 21

2.3 Core Properties of Dislocations in Semiconductors 24

3 Atomistic Simulation Techniques Applied to Dislocations **30**

3.1 Introduction 30

3.2 A Dislocation in an Atomistic Simulation 31

3.3 Molecular Dynamics and Energy Minimization Methods 33

3.4 Finding Reaction Paths and Activation Barriers 36

4 Potential Function for Silicon **41**

4.1 Introduction 41

4.2 Survey of Existing Empirical Models for Si 42

4.2.1 The Stillinger-Weber Potential 43

4.2.2 The Tersoff Potential 44

4.2.3 Other Empirical Potentials 45

4.3 New Empirical Potential for Si 47

4.3.1 Functional Form 47

4.3.2 Fitting Procedure and Database 50
4.4 Tests of the New Potential 51
4.5 Thermal and Vibrational Properties 54
4.6 Core Properties of Dislocations in Si 58
4.7 Conclusions 60

5 Dislocation Core Reconstruction and Its Effect on Dislocation Mobility **79**
5.1 Introduction 79
5.2 The Model and Numerical Details 81
5.3 Results and Discussion 83
5.3.1 Core reconstruction 84
5.3.2 Kink formation energy 85
5.3.3 Left-right dislocation asymmetry 87
5.3.4 The effects of 2×1 core reconstruction on kinks in 30^o partial 90
5.3.5 Kink-soliton complexes 91
5.3.6 Kink migration energies 93
5.4 Summary 96

6 Core Effects in Dislocation Intersection **109**
6.1 Introduction 109
6.2 Methodology 110
6.3 Results and Discussion 113
6.4 Summary 116

7 Conclusions **124**

A Force Expression for the New Empirical Potential **128**
A.1 Energy Calculation 128
A.2 Force Calculation 130

List of Figures

2-1 $[1\bar{1}0]$ projection of a diamond cubic lattice. Line s represent shuffle planes (between planes labelled by letters of the same type). Line g represent glide planes (between planes labelled by letters of the different type). 26

2-2 Atomic structure in the core of a 90^o-partial dislocation on the (111) plane. (a) symmetric and (b) asymmetric reconstructed configurations. 27

2-3 Atomic structure in the core of a 30^o-partial dislocation on the (111) plane. (a) unreconstructed and (b) reconstructed configurations. . . . 28

2-4 Anti-phase defect (APD) for the (a) 30^o-partial and (b) 90^o-partial dislocation. 29

3-1 Cell geometry used in the simulations of dislocations. 39

3-2 Box cell with the three vectors a, b, and cthat define the box shape. 40

4-1 Two body interaction term $V_2(r)$ at different coordinations for the new potential, compared to the SW two-body term. 66

4-2 $G(\theta)$ of the three-body interaction as function of angle, compared to the SW and Tersoff (T3) angular terms. 67

4-3 Three-body interaction term V_3 as function of angle for a set of three atoms at distances 2.35 $\mathring{A}$ compared to SW term. 68

4-4 Individual coordination function $f(r)$, that determines the contribution of each neighbor to the effective coordination Z. 69

4-5 Cosine of the optiomal angle $\tau(Z)$ as function of coordination. 70

4-6 Energy of the concerted exchange path for DFT, SW, Tersoff and this potential. 71
4-7 Cross section of the Generalized Stacking Fault energy surface for DFT, SW, and this potential. (a) < 112 > and (b) < 110 > directions. . . . 72
4-8 Phonon dispersion curve of Si at $0K$ for the SW potential. 73
4-9 Phonon dispersion curve of Si at $0K$ for the Tersoff potential. 74
4-10 Phonon dispersion curve of Si at $0K$ for this new potential. 75
4-11 Heat capacity C_V as function of temperature obtained from the quasi-harmonic approximation for Tersoff, SW, and this model. 76
4-12 Thermal expansion coefficient as function of temperature obtained from the quasi-harmonic approximation for Tersoff, SW, this model, and experimental results. 77
4-13 Density of the system as function of temperature for SW, Tersoff, and this model as compared to experimental results. 78

5-1 Double kink in a 30^o-partial dislocation. 102
5-2 Double kink in a 90^o-partial dislocation. 103
5-3 Projection of the simulation cell in the the {111}glide plane for calculation of the single kink formation energy. 104
5-4 Structure of left complex (LC) (a) and right complex (RC) (b). . . . 105
5-5 Lowest energy path for the motion of LR kink in 90^o partial dislocation. 106
5-6 Lowest energy path for the motion of LR kink in 90^o partial dislocation. 107
5-7 Lowest energy path for the motion of LR kink in 90^o partial dislocation. 108

6-1 Cell construction for the intersection process. Dislocation 1 with Burgers vector b_1 and dislocation line vector ξ_1 is created in glide plane 1, similarly dislocation 2 in glide plane 2, before the intersection (a) and in the process of intersection (b). In a cartesian coordinate system, the dislocation dipole 1 is in the XZ plane and dislocation 1 lies in Z-direction. 118
6-2 Thompson's tetrahedron. 119

6-3 Scattering process of two dislocation represented in Thompson's tetrahedron. (a) $30^o - 30^o$ partial dislocation process, and (b) $90^o - 90^o$ partial dislocation process. 120

6-4 Defects formed in dislocation 1 in the 30^o-30^o (a,b) and 90^o-90^o (c,d) intersection processes. In the present geometry, d_x and d_y give the in-plane and out-of-plane components respectively. Distances are given in Angstrons. 121

6-5 Final configurations for (a) the 30^o-30^o and (b) the 90^o-90^o intersection processes in dislocation 1 in glide plane 1. The core atoms are represented in black. 122

6-6 The 30^o-30^o interaction process as two dislocations just intersect. The figure shows the evolution of the dislocation core of dislocation 1 (a) before and (b,c) after intersection with dislocation 2 in another glide plane. Two different final results are shown, (b) the defect is formed by breaking a reconstruction bond and (c) the defect is formed between two different reconstruction bonds. The core atoms are represented in black. 123

List of Tables

4.1 Parameters for the Stillinger-Weber model. 61

4.2 Parameters for the Tersoff model. 61

4.3 Best fit parameters for this new model. 62

4.4 Diamond cubic bulk properties from DFT calculations, SW, Tersoff, tight-binding and this model. 62

4.5 Energy and lattice parameters for high symmetry structures. 63

4.6 Elastic constants (given in unit of $Mbar$) for the diamond cubic structure. 63

4.7 Relaxed and unrelaxed formation energies of point defects (in eV). *Ab initio* results are unrelaxed configurations. 64

4.8 Phonon frequencies (in THz) for transverse acoustic $TA(X)$, tranverse optical $TO(X)$, longitudinal optical and acoustic $LOA(X)$, and longitudinal-transverse optical $LTO(\Gamma)$. 64

4.9 Grüneisen parameters from experiment, SW, Tersoff, and this model. 65

4.10 Reconstruction energy and APD energy for core structures of partial dislocations. 65

5.1 Reconstruction effects on energetics of core defects in 30^o-partial dislocation. 98

5.2 Reconstruction effects on energetics of core defects in 90^o-partial dislocation. 99

5.3 Topological charges, formation and migration energy of the core defects in 30^o-partial dislocation. 100

5.4 Topological charges, formation and migration energy of the core defects in 90^o-partial dislocation. 101

6.1 Scattering processes between two dislocations, based on Tompson's Tetrahedron for two dislocations in the planes shown in Fig. 6-1 . K and J denote respectively the kink and jog formed in a dislocation as result of the intersection. 117

6.2 Comparison of simulation results for defect formation with the value expected theoretically (d^{th}). Here the x- and y-components give the in-plane and out-of-plane contributions respectively in the defect on dislocation 1. 117

Chapter 1

Introduction

1.1 Motivation and Background

Silicon has been a material of great technological and fundamental interest over the last few decades [1, 2]. Due to the strongly directional covalent bonding between the atoms, it crystallizes in the diamond cubic lattice structure. Silicon has a band gap of 1.2 eV, and is primarily used as a basis material for microelectronics.

Despite the previous extensive studies on silicon, which resulted in improved understanding of fundamental physics of semiconductors, there are many issues in silicon technology which are still not well understood from the fundamental point of view. One of the areas of major concern is material processing. Typical chips have millions of working transistors, which should work properly with high level of precision. The more the technology evolves, the smaller the working parts become, and the subtleties of the physical processes in the chips become more critical. The fabrication of such devices involves a combination of conditions (such as level of impurities and defects) which require high level of control.

Of the problems of major concern in processing, we can mention self-diffusion, diffusion of dopants, gettering, and crystal growth. For example, very little is known about the diffusion in silicon. Although theoretical calculations have provided im-

portant insights into this process, the experimental data shows large discrepancies in the diffusion coefficient [1]. The major problem here is to correlate experimental and theoretical analysis. While theoretical modeling has studied simple processes, the problem is that in the experiments several effects act simultaneously (doping, clustering of defects, level of purity, etc). Consequently, we still do not know enough about the nature of diffusivity in order to control it.

Gettering is another important aspect of silicon technology. Gettering relates to the removal of unwanted impurities from the active region of the device. This is done by creating attractive centers for the defects (impurities) somewhere else in the wafer. Consequently, there will be an increase in the density of "good" material in the the active region, improving the device efficiency. However, the physical processes underlying gettering are not well understood.

To improve the quality of the electronic devices, one needs to extend the understanding of the phenomena involved in their processing. Although these phenomena are already complex, because they involve several processes simultaneously, there are other effects which should also be accounted for. In particular, extended defects (dislocations) play a role in most of such technologically important processes, including diffusion, gettering, and crystal growth. Consequently, some of the uncertainty in the experimental data mentioned above stems from the lack of understanding of the role of dislocations in the material processing [3].

Dislocations alter both electronic and mechanical properties of semiconductors. Sometimes they are detrimental to the devices, sometimes they are useful. An example of the detrimental effects of dislocations is their interactions with point defects. Dislocations attract point defects providing conditions for defect clusterizing, which may be detrimental to the device. On the other hand, in the case of gettering, dislocations play a role in improving the quality of the semiconducting wafer. Dislocations, introduced by scratching in the back of the wafer, may serve as attractive sites for the unsaturated impurities, improving the device performance.

In terms of the electronic properties, experimental evidence [4], supported by theoretical calculations [5], shows that only a few percent of atoms in the dislocation

core have dangling bonds, responsible for the in-gap states. At the same time, in terms of the mechanical properties, dislocation motion (and plasticity) is controlled by the processes in the dislocation core [7]. Furthermore, there is a strong electro-mechanical coupling in semiconductors, meaning that the electronic properties affect mechanical behavior, and vice versa. This coupling is directly observed in some semiconductors which present photoplastic behavior. Consequently, determining the important phenomena inside the dislocation core [6, 7] is crucial for understanding the nature of electromechanical coupling, and can be useful for better control of the device quality.

Since dislocations in silicon essentially do not move at operation conditions, at low temperature (a few hundreds Kelvin), mobility was not considered a topic of great importance until recently. However, it was found that not only dislocations move at high temperature, but also they multiply. All this dynamic characteristic of dislocation inside the semiconductor gives the material a ductile behavior, but at the same time may be detrimental to the electronic properties of the device. Dislocations move in the crystal by formation and propagation of kinks. It is expected, therefore, that dangling bonds may be left unsaturated, and/or point defects may be created, as dislocations move through the crystal. Besides, in the crystal growth process, dislocations are formed as a result of the mismatch between epitaxial planes and play an important role in the physical properties of the interface. Understanding and controlling dislocation formation and motion, therefore, is necessary for improving device quality.

1.2 Problem Statement and Scope of the Thesis

A considerable challenge in the area of materials processing is to develop theoretical models which can serve as guidance for experimentalists [8]. Because of the large number of physical (and chemical) processes involved simultaneously, it is imperative to have a reliable theoretical model which includes most of these effects in a realistic

fashion. This complicated task may be pursued in part by computer simulations at an atomistic level. Simulations, therefore, may serve as a bridge between theory and experiment by providing key parameters which can be useful for the understanding of the materials and processes.

In materials science, the goal of atomistic simulations is to provide understanding of the microscopic phenomena, and identify relevant atomic mechanisms and properties of interest. This theoretical approach requires several essential elements: reliable models to describe the interatomic interactions, powerful methods to solve the equations of motion, and adequate computational resources. The primary goal of this thesis is to address some of these issues, by developing methodology for predictive modeling of microscopic mechanisms in semiconductors using computer simulations.

The scope of this thesis is to perform a detailed study of the microscopic mechanisms of dislocation mobility in silicon using atomistic simulations and empirical potentials. This is performed in three parts. First we develop a new empirical potential for silicon. Then, we use this new empirical potential to study dislocation mobility by the mechanisms of kink formation and propagation. Finally, we study the core effects in dislocation intersection.

One of the major limitations of atomistic simulations, specially for semiconductors, is the accuracy of the potential function describing interatomic interactions. It is desirable to use first principles quantum-mechanical methods [9], but they require large computational effort. Therefore, applications of these methods are limited to relatively small systems. On the other hand, empirical potentials can handle much larger systems, although at the cost of lacking the accuracy of the description of interatomic interactions. Therefore, it is imperative to have a model which is simultaneously reliable and computationally efficient to describe the interatomic interactions in semiconductors. Considering this, and the fact that our final goal is to study complex processes inside the dislocation core, we developed a new empirical potential for silicon. The new empirical potential for Si includes two- and three-body interaction terms. The functional forms are theoretically motivated by the chemical and physical trends in atom-atom bonding as a function of the local coordination. Another aspect

of major concern is the choice of the database used for finding the best set of parameters in the interaction terms. We have chosen to use a reasonably small set of *ab initio* results, emphasizing bulk structures and defects. The resulting description is a considerable improvement over other empirical models in treating bonding in local structures substantially differing from the perfect tetrahedral coordination.

The new empirical model is then used to study core properties of partial dislocations in silicon. The description of the core properties of partial dislocations in the {111} glide set is in excellent agreement with *ab initio* results. The new model correctly describes core reconstructions and antiphase defects in both 30^o- and 90^o partial dislocations, for example, the asymmetrical reconstruction of the 90^o partial dislocation. Neither Stillinger-Weber nor Tersoff potentials, two of the most used empirical potentials, are capable of dealing with such details of dislocation core properties.

This empirical potential appears to be reliable in the applications involving dislocations. We, therefore, use this new model to study motion of both 30^o and 90^o partial dislocations in silicon. Our goal is to identify the leading atomistic mechanisms of double kink formation and migration. This is performed by using energy minimization methods to identify the stable kinked configurations. Then, by computing the reaction path connecting two stable kinked configurations, we identify the mechanisms of kink mobility. Specifically, we find that the core reconstruction plays a major role in the mobility of a dislocation, providing a mechanism of additional resistance to dislocation motion in Si. In the case of the 30^o partial dislocation, two kinds of kinks are identified, left and right, which have different structures, formation energies, mobilities and interactions with antiphase defects. These results corroborate with earlier studies [7] performed using the Stillinger-Weber potential.

Another important aspect of dislocation properties is the mechanism of dislocation intersection. Our goal is to use atomistic simulations to examine the atomic mechanisms inside the dislocation core as two dislocations are brought together and intersect. We find that the intersection of two dislocations (at close encounter) is another manifestation of core properties of the dislocation. The formation of the jogs resulting from intersection can be viewed as a convolution of two dislocation densities

distributed in two non-parallel glide planes. These defects (jogs) start to form even before the two dislocations have their geometric center intersecting.

This thesis is organized as follows. Chapter 2 gives an introduction to dislocations in semiconductors. Chapter 3 discusses the methodology used in this study of dislocation mobility in semiconductors. Chapter 4 presents the new empirical potential for silicon, including a discussion on the theoretical motivation for the functional form and tests for several structures and properties. Chapter 5 presents results for the study of the mechanisms of dislocation mobility based on the kink formation and propagation. Chapter 6 presents a study of the atomistic mechanisms involved in dislocation intersection in silicon. Finally, Chapter 7 presents some final remarks and prospects for future work.

Chapter 2

Introduction to Dislocations

The response of a material to applied stress has been a topic of great interest from both fundamental and technological point of view [10]. How a material deforms under applied load? How the mechanical properties are affected by the temperature? Why the material behavior changes from ductile to brittle at certain conditions? Most of these physical properties of crystalline materials are related, to a certain extent, to the presence of extended defects, called dislocations. In this chapter we present an introductory review on the properties of dislocations and its relation to materials plasticity. Then we focus on the core properties of dislocations in semiconductors.

2.1 Dislocations and Plasticity

Early theoretical models for the material resistance to applied loading [11, 10] failed to describe the magnitude of the stress required for a crystal to deform plastically. The calculated critical shear stress (the minimal stress required for the material to deform) was found to be orders of magnitude $(10^4 - 10^5)$ larger than the one observed experimentally. This puzzling contradiction was explained by Orowan, Polanyi, and Taylor who independently in the 1930's [12] suggested that the low mechanical strength of the materials results from the presence of dislocations. These extended defects play a

key role in the mechanisms of plastic deformation, and consequently, in the mechanical behavior of materials. As dislocations move in a crystal, in response to external load, the material deforms as result of this motion.

A dislocation is a line defect in the crystal which has a a region around its geometric center called dislocation core. Within the core the atoms have a specific geometry which is distinctly different from that of the perfect crystal, whereas outside the core the atoms have coordination similar to the perfect crystal. The influence of a dislocation on the physical properties of the material is determined by its long range, elastic strain fields. For distances larger than the core radius (r_c) from the dislocation center, the influence of a dislocation is well described by continuum elasticity theory [10]. On the other hand, inside the core, interactions are strongly dependent on the atomic structure, and the elastic theory becomes inaccurate. In this non-linear region, in which elasticity theory breaks down, an atomistic model which describes the details of the crystal lattice becomes indispensable.

Dislocations can have edge, screw or mixed character depending on their geometries. This dislocation character is defined by the angle between the Burgers vector $\underline{b}$ and the dislocation line vector $\underline{\xi}$. Here, the Burgers vector is defined as the discontinuity in the displacement field caused by the presence of a dislocation in the crystal (measured in units of distance). The dislocation line vector is a unit vector tangential to the dislocation line. If the Burgers vector $\underline{b}$ is perpendicular to the dislocation line vector $\underline{\xi}$, the dislocation is defined as an edge dislocation, if $\underline{b}$ is parallel to $\underline{\xi}$, it is a screw dislocation. For any other angle between $\underline{b}$ and $\underline{\xi}$, the dislocation is said to have a mixed character.

Dislocations create long-range stress fields and large strain energies. The stress field of a dislocation, calculated using elasticity theory [10], is inversely proportional to the distance from the dislocation center. The self-energy of any straight dislocation is given by:

$$E = \frac{Kb^2}{4\pi} \ln \frac{r}{r_c} \quad , \tag{2.1}$$

where r is the distance from the dislocation, r_c is the core radius, $b = |\underline{b}|$ is the

magnitude of the Burgers vector, and K is a constant called energy factor, which is equal to μ for screw dislocations and to $\mu/(1-\nu)$ for edge dislocations. Here μ is the shear constant, and ν is the Poison's ratio. This solution is accurate only for distances larger than the core radius, which is usually of the same order of magnitude as b.

Using Equation 2.1, in which the the self-energy of a dislocation is proportional to b^2, one might deduce a very important stability criterion. A dislocation splits into other two dislocations if this results in a lowering of the total energy. For example, a dislocation with Burgers vector $\underline{b}_1$ can split into two dislocations with Burgers vectors $\underline{b}_2$ and $\underline{b}_3$ if the following inequality is satisfied:

$$\underline{b}_1^2 > \underline{b}_2^2 + \underline{b}_3^2 \quad , \tag{2.2}$$

i.e., a dislocation would spontaneously dissociate only if there is an energy gain for such process, otherwise the dislocation is stable against dissociation. As will be shown in the next section, dislocation dissociation is favorable in semiconductors, and that will have an important effect in the mechanical and electronic properties of the material.

2.2 Dislocations in Semiconductors

Since the discovery of dislocations, most investigations have been focused on the role of dislocations in plastic deformation of metallic materials. However, over the last few years, dislocations in semiconductors have attracted considerable interest [13, 4] for several reasons. It was found that dislocations not only affect the mechanical properties of a crystal but also its electronic properties. In semiconductors, it is experimentally observed [4], and verified by theoretical calculations [5], that the dislocation core may be responsible for the appearance of energy levels in the band gap. Therefore, dislocations can provide conductive paths, which are detrimental to the

electronic properties of the device. Furthermore, the dislocation core may contain electronically active centers, interacting with intrinsic and extrinsic defects.

The properties of dislocations depend on the nature of the material bonding. Although directionality of atomic bonding is somewhat relevant in metallic structures, it is of greatest importance in semiconductors. This strong bonding directionality has important effects on dislocation properties, where dislocation cores are generally narrower in semiconductors than in metallic systems.

As consequence of the strong bond directionality, dislocation mobility is considerably lower in semiconductors than in metals. Besides, motion of dislocations in semiconductors is affected by their electronic properties. For example, photoplasticity has been observed in some semiconductors (GaAs), in which dislocations move faster under incident light [14]. These and other unusual effects are all different manifestations of a strong electro-mechanical coupling ubiquitous in semiconductors.

To understand the characteristics of dislocations in semiconductors, we first provide a description of the geometry of the diamond cubic lattice, and then, dislocations in such lattice geometry. Tetravalent semiconductors crystallize in the diamond cubic (DC) structure, which is composed of two interpenetrating face-centered cubic (FCC) lattices. Figure 2-1 shows the diamond cubic lattice projected normal to the $[1\bar{1}0]$ direction, with $\{111\}$ planes stacked in the sequence AaBbCcAa .... Each atom in the DC lattice is bonded to four nearest neighbors by sp^3 covalent bonds. In that structure, there are two distinct $\{111\}$ glide planes, as shown in figure 2-1. The shuffle plane, represented by letter s in the figure, is defined as the imaginary plane between planes of the same letter index (Aa, for example), and cuts atomic bonds that are perpendicular to the $\{111\}$ plane. The glide plane, represented by g in the figure, is between two neighboring planes of different indexes (aB, for example) and cuts the bonds in the closed-packed planes.

Perfect (or full) dislocations have Burgers vector $a/2 < 110 >$ and glide in the $\{111\}$ slip planes. Here a is the interatomic distance. Also, dislocations in semiconductors show strong preference to be oriented along a low-index direction (for example, $< 110 >$) on the glide plane of the crystal, in order to lower the dislocation

self-energy.

In the case of tetravalent semiconductors, there are two types of full dislocations in the glide plane: the screw and the 60^o-full. Screw dislocations have Burgers vector which is parallel to the dislocation line vector, while 60^o-full dislocations have Burgers vector forming a 60^o angle with the dislocation line vector. Although dislocations can form in the glide or shuffle planes, the dislocations in the glide plane are believed to be more important in the deformation processes [10, 15]. Full dislocations in the glide set can dissociate into partial dislocations, to minimize energy. The 60^o-full dislocation dissociates into a 30^o-partial and a 90^o-partial, while a screw dislocation dissociates into two 30^o-partials. Here, the 90^o-partial (edge) dislocation has a Burgers vector perpendicular to the dislocation line vector, and the 30^o-partial has a Burgers vector making an angle of 30^o with the dislocation line vector. The dissociation can be expressed by:

$$60^o\text{-full} \rightarrow 30^o\text{-partial} + 90^o\text{-partial} \tag{2.3}$$

$$\text{full screw} \rightarrow 30^o\text{-partial} + 30^o\text{-partial} \ . \tag{2.4}$$

Between the two partial dislocations, formed as a result of dissociation, there is a low-energy stacking fault. The equilibrium distance between the two partials is determined by the balance of the attractive force resulting from the stacking fault and the $1/r$ elastic field repulsion.

Dislocations in the shuffle set, on the other hand, have a more complicated structure. In the shuffle plane there is no low-energy stacking fault, and dissociation of full dislocations of shuffle set is not possible. Furthermore, motion of partial dislocations in the shuffle set is thought to be hindered because it involves mass transport (movement of vacancies or interstitials) [10].

2.3 Core Properties of Dislocations in Semiconductors

Elasticity theory gives an accurate description of the long-range interactions between dislocations. In the region close to the dislocation center (dislocation core), where discrete atomic structure becomes important, the simple notion of the material as a continuum field is no longer valid, and one has to consider the atomic details inside the dislocation core.

Core properties, as was mentioned earlier, affect strongly the mobility of the dislocations. In the case of semiconductors, the mobility is sensitive to the electronic state of the crystal. To understand this coupling between electronic and mechanical properties of the material, one needs to consider the microscopic structure of the dislocation core.

Atoms in the diamond cubic structure have four nearest neighbors connected by the covalent bonds. On the other hand, broken (dangling) bonds can be expected to appear inside the dislocation core. These unsaturated bonds in the dislocation core should be electrically active, resulting in the formation of electronic levels in the gap. These gap levels, localized at the dislocation core, may act as carrier traps or preferred sites for impurities. However, experimental results show that only a few per cent [4] of the atomic sites in the dislocation core are electrically active. This points to a possible rehybridization of dangling bonds inside the dislocation core that recovers tetravalent bonding. This rehybridization process, called core reconstruction, lowers the energy of the system. Therefore, dislocations are expected to be reconstructed in equilibrium.

The reconstruction energy (E_{rec}) of the dislocation core is defined as the gain in energy per unit length of a dislocation on going from an unreconstructed configuration to a reconstructed configuration.

$$E_{rec} = \frac{E_T(rec) - E_T(unr)}{L} \quad , \tag{2.5}$$

where $E_T(rec)$ and $E_T(unr)$ are the free energies of the system at reconstructed and unreconstructed configurations respectively, and L is the length of the dislocation.

Figure 2-2 shows the atomic arrangement in the atomic layers adjacent to a $\{111\}$ glide plane with a 90^o-partial dislocation. Configuration (a) shows the unreconstructed state and (b) the reconstructed state. Atoms in the dislocation core of configuration (a) shift in the direction parallel to the dislocation, and recover the fourfold bonding coordination.

Figure 2-3 shows (a) the unreconstructed state and (b) the reconstructed state of a 30^o-partial dislocation in a $\{111\}$ glide plane. Here the atoms recover the fourfold bonding coordination by forming pairs, similar to the dimerization of atoms on the $\{111\}$ silicon surface. In the case of 30^o-partial dislocations, reconstruction doubles the repeat distance along the dislocation. This doubling of the repeat distance in the core of a 30^o-partial dislocation has been studied recently [7], and it has been shown to affect in the mobility of dislocation.

As consequence of reconstruction of the partial dislocations a new kind of point defect, resulting from the symmetry breaking inside the core, becomes possible. This defect, called antiphase defect (APD) or soliton, is an irregularity in the reconstruction of the dislocation core, in which one atom remains in threefold coordination. An APD example is shown in figure 2-4, (a) in a 90^o-partial and (b) in a 30^o-partial dislocation. The existence of these defects is consistent with experimental results, which show that a few percent of the core center of dislocations remain electrically active. These APD have important effects in the dislocation mobility as shown recently by V. V. Bulatov, *et. al.* [7].

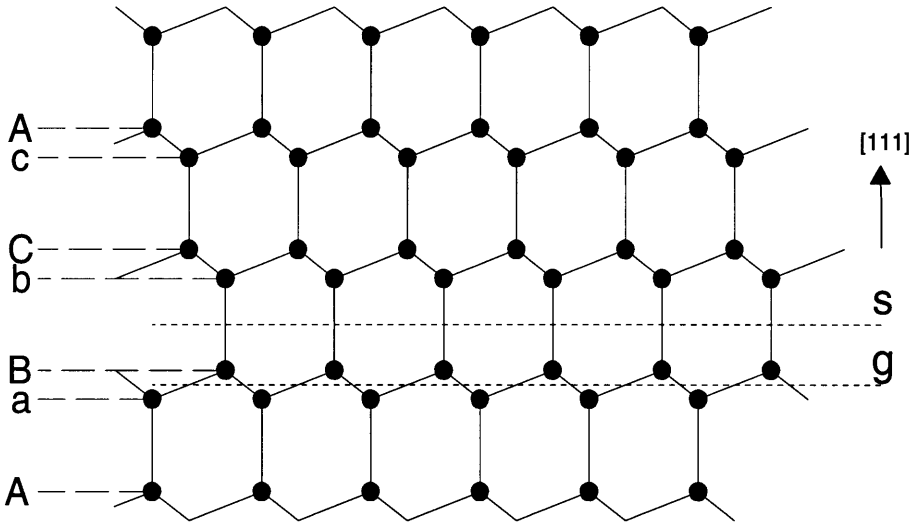

Figure 2-1: $[1\bar{1}0]$ projection of a diamond cubic lattice. Line s represent shuffle planes (between planes labelled by letters of the same type). Line g represent glide planes (between planes labelled by letters of the different type).

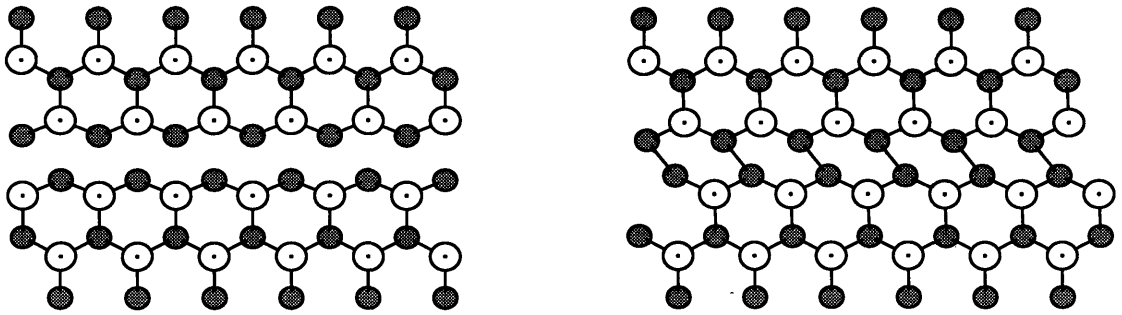

Figure 2-2: Atomic structure in the core of a 90°-partial dislocation on the (111) plane. (a) symmetric and (b) asymmetric reconstructions.

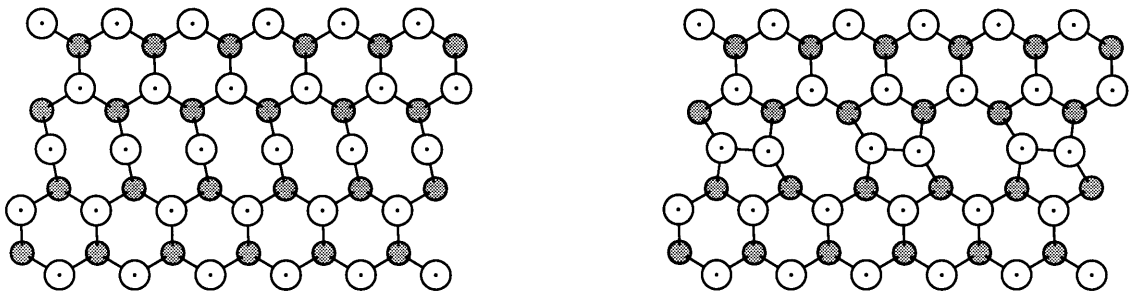

Figure 2-3: Atomic structure in the core of a 30°-partial dislocation on the (111) plane. (a) unreconstructed and (b) reconstructed configurations.

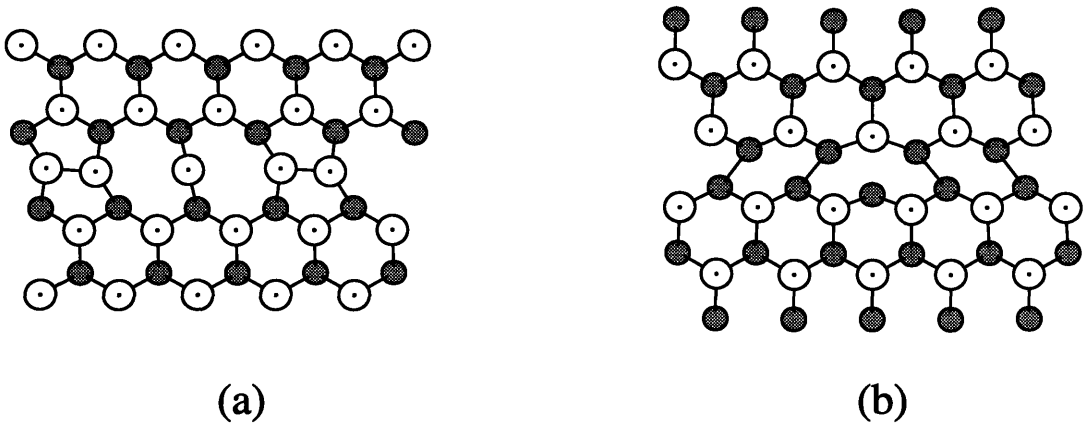

Figure 2-4: Anti-phase defect (APD) for the (a) 30^o-partial and (b) 90^o-partial dislocation.

Chapter 3

Atomistic Simulation Techniques Applied to Dislocations

3.1 Introduction

With the development of fast and affordable hardware, combined with reliable models for description of interatomic interactions, computer atomistic simulations are increasingly used in investigations of microscopic properties and processes. Simulations have been widely used as a unique tool in areas ranging from chemistry to materials science, from physics to biology, providing an understanding of the fundamental processes in complex systems at the atomic and molecular level. The first atomic-scale simulations used Monte Carlo (MC) methods, and later molecular dynamics (MD) [16]. Following the early success, other methods, such as energy minimization techniques, were also developed.

Although methods of atomistic simulations reached a high level of sophistication and efficiency, several important issues, such as interatomic potential, boundary conditions and thermodynamical ensembles, should be addressed. The critical problem involving calculations at atomistic level is the reliability of the physical description of the interatomic and electronic interactions. *Ab initio* methods, based on quantum

mechanics, provide full details of the electronic and atomic interactions, but they require considerable computational effort. Consequently, simulations at this level of detail are limited to systems containing up to a few hundreds of atoms. Classical methods, based on empirical potentials, are much more expedient but at the cost of a poorer description of the interatomic interactions. The reliability of empirical models will be discussed in Chapter 4.

In this chapter, we consider several technical aspects involved in an atomistic simulation. Section 3.2 discusses setting up the simulation cell for each specific calculation performed here. Section 3.3 presents various aspects of molecular dynamics and energy minimization methods. Section 3.4 describes the techniques to identify transition states using energy minimization methods.

3.2 A Dislocation in an Atomistic Simulation

In this section we discuss the cell geometry and the boundary conditions used through the simulations, which are fundamental for obtaining meaningful results.

Atomistic simulations of dislocations require careful considerations of boundary conditions (BC). To avoid spurious effects, periodic boundary conditions (PBC) are used throughout the simulations. Using these BC means that the simulation cell, called the primary cell, is replicated in all three directions to simulate a bulk material. These boundary conditions have certain advantages in applications involving dislocations, which can be explained by the characteristics of dislocation-dislocation interactions. Dislocations interact with each other by long-range stress fields which are well described by continuum elasticity theory [10]. Using PBC, one can simulate an infinite dislocation in the crystal, avoiding the always complicated interaction of a dislocation with a free surface [10, 17]. On the other hand, the advantageous feature of the boundary conditions comes with a price. First, due to the nature of PBC, it is impossible to introduce a single dislocation in the simulation cell. Therefore, dislocations in a simulation always come in pairs (which we call a dislocation dipole).

Second, when using PBC, dislocations in the primary cell interact with dislocation images in the neighboring cells, and, since dislocations interact with each other by long-range fields, this introduces undesired external stresses. Distortions resulting from interactions of a dislocation in the primary cell with its images may be reduced by introducing a different structure for the simulation cell, in which the cell is constructed to provide a quadrupole dislocation arrangement [18]. We choose to use large primary cells instead, which also minimizes the interactions of the dislocations with their images.

Figure 3-1 shows the geometry of the primary cell used in our simulations. As discussed in the previous chapter, dislocations in semiconductors lie along the $<110>$ directions in the $\{111\}$ planes, and the simulation cell uses this geometry. The simulation cell has the structure of a square box, with the X, Y and Z axes chosen to be in the directions $[11\bar{2}]$, [111], and $[\bar{1}10]$, respectively. Dislocations, then, lie in the plane normal to [111] vector (XZ-plane) and the dislocation line is parallel to $[\bar{1}10]$ (Z-direction). As a consequence of the PBC, the dislocations exit and re-enter (in Z-direction) the cell in the same point, so that the dislocations are straight and essentially infinite.

In the simulation cell, dislocations are always introduced in pairs (dislocation dipole) due to the PBC conditions. A dislocation dipole in a [111] glide plane is created by making a cut and shifting the atoms in the planes aB as shown in Figure 2-1: the atoms in the atomic plane just above the cut are shifted from their original positions by half Burgers vector, while the atoms in the plane just below the cut are shifted by the same half Burgers vector, but in the opposite direction. For partial dislocations, the introduction of the dipole creates a stacking fault between the two dislocations, represented by the shaded area in Figure 3-1.

To minimize the effects of the interaction of dislocations with their images, we create the dipoles in which the distance between the two dislocations is half of the size of the cell in that direction (X-direction). The number of atoms used in the simulations varied for each specific application. For studies of dislocation core properties, we have found that 3000 atoms are enough to avoid core-core overlap. In this structure,

the distance between dislocations in the primary cell is approximately $30\mathring{A}$, which is large enough to avoid such core-core interactions. For other applications, such as kink motion, cells up to 22500 atoms were used.

3.3 Molecular Dynamics and Energy Minimization Methods

Molecular dynamics (MD) and energy minimization methods (conjugate gradient relaxation and simulated annealing) are used extensively throughout this work. Most of the calculations involving dislocations are performed using energy minimization methods. On the other hand, for other systems, as described in Chapter 4, molecular dynamics is also employed.

Molecular dynamics is a technique to describe the time evolution of a N particle system with well-defined potentials under finite temperature conditions and/or finite external stress. In an MD simulation, the trajectories for the $3N$ atomic degrees of freedom are generated by numerical integration of Newton's equations of motion. The basic output of an MD simulation run includes time-dependent positions and velocities of the particles, forces, and stresses. The MD approach has been extensively used in atomistic simulations to study a variety of systems including solid, liquid and amorphous phase [16, 83].

In statistical mechanics language, the MD simulation describes a trajectory in a $6N$-dimensional phase space comprised of positions and momenta of all particles in the system. To compute properties of the system, such as vibrational, transport and thermodynamical quantities, one samples over the phase space, and takes averages of these quantities. By constraining the trajectory in the phase space to a hyper-surface, one can explore different ensembles, such as microcanonical ensemble (NVE), canonical ensemble (NVT), isothermal-isobaric ensemble (NPT), and the isoenthalpic-isotension ensemble ($NH\tau$).

In the *microcanonical ensemble* (NVE) the quantity conserved is the internal en-

ergy E and volume V. The canonical ensemble (NVT) is established by constraining the kinetic energy to a certain temperature T. This is achieved by rescaling particle velocities at every step in the MD simulation. Although there are other more sophisticated techniques of constant temperature simulations, such as the Andersen [20] and the Nosé [21] methods, the simple velocity rescaling was found adequate for our calculations.

Calculations at constant stress or constant pressure ensembles may be performed with the method proposed by Parrinello and Rahman [22] and later modified by Ray and Rahman [23]. Using this method, the shape and the size of the periodically repeated simulation cell may change in response to the internal or external stresses. Consider three vectors $\underline{a}$, $\underline{b}$, and $\underline{c}$ as the borders of the simulation cell, as shown in Figure 3-2. They form the 3×3 matrix ("metric matrix") $H = (\underline{a}, \underline{b}, \underline{c})$. The position of any particle i ($\underline{r}_i$) is written in terms of the metric matrix by:

$$\underline{r}_i = H\, \underline{s}_i \tag{3.1}$$

where $\underline{s}_i$ is the vector of the reduced coordinates of particle i with each component ranging from -0.5 to 0.5 . The whole system evolves according to equations of motion for the reduced coordinates ($3N$ degrees of freedom), and equations of motion for the components of the metric matrix (9 degrees of freedom). In particular, the system responds to external stress by deforming the simulation cell. By simultaneously applying temperature rescaling and the Parrinello-Rahman method, we generate the (NPT) or ($N\tau T$) ensembles [24].

While molecular dynamics is a powerful tool to study thermal properties at the atomistic level, energy minimization methods provide a tool to study static properties ($T = 0$). In an energy minimization simulation, the goal is to find a state in the configurational space which corresponds to an energy minimum. In this category of methods, the conjugate gradient (CG) and the simulated annealing (SA) [25] methods have been the most widely used.

For problems involving dislocation mobility, we choose energy minimization meth-

ods rather than the traditional molecular dynamics for several reasons. Although molecular dynamics simulations have been extensively used to study dislocation mobility in metals [26], it has been shown [6, 27] to be ineffective for dislocation mobility in semiconductors. Simulation of dislocation motion in semiconductors involves breaking of strong covalent bonds. Consequently, dislocation mobility is relatively low [3] in semiconductors compared to metals. Dislocation motion involves formation and propagation of kinks which have activation energies of the order of 1 eV (this topic will be discussed in Chapter 5). Therefore, the mechanisms of kink formation and propagation in semiconductors are in the category of rare events, i.e., the time scale for those events is much longer than a typical time scale of an MD simulation [28]. An alternative way to study the mechanisms of dislocation mobility in semiconductors would be using energy minimization methods, such as conjugate gradient and simulated annealing methods.

The conjugate gradient (CG) method is designed for finding a local minimum of a function (of many variables) through the steepest descent algorithm [25]. The system is brought to the nearest energy minimum, in this case by moving the atoms in the direction of the forces. Our simulations using the conjugate gradient method are performed at constant stress [22] in the space of $3N + 9$ degrees of freedom, $3N$ from the atomic relative coordinates plus 9 parameters characterizing the shape of the simulating cell, as shown in the Section 3.2. Although the conjugate gradient method is very powerful and computationally efficient, it is suitable for finding only local minima. Starting the simulation at a certain configuration, the CG always drives the system downhill to the closest equilibrium state, which is not necessarily the one of interest. For finding other relevant minima, which are not in the immediate neighborhood of the starting configuration, we used the simulated annealing method.

The method of simulated annealing (SA) [29] is designed for searching the global minimum of the energy, and is effective even when the desired minimum is hidden among many local metastable states. Considering the $3N$-dimensional configurational space, the basic idea of the simulated annealing method is to explore the complex topography of the energy landscape in order to find the global minimum. This is

done using Metropolis sampling [25] by starting with a certain high temperature T, and sampling for long enough so that the relevant part of the configurational space is explored. The search at each temperature will move uphill and downhill by energies of the order of k_BT, where k_B is the Boltzman constant. Then, by subsequently decreasing the temperature according to a specific annealing schedule, the system is brought to a minimum. Although such a procedure does not guarantee finding the very lowest minimum of energy, it finds reasonably low minima if an appropriate annealing sequence is used [25].

3.4 Finding Reaction Paths and Activation Barriers

As mentioned earlier in this chapter, molecular dynamics is not suitable for simulations of dislocation motion in semiconductors. To overcome this methodological limitation, in this section we describe an alternative approach to study dislocation mobility. In the previous section, we described the techniques of finding the equilibrium configurations by energy minimization methods. In this section, we describe a technique to obtain information about the kinetics of dislocation motion using energy minimization methods.

First we consider that, in principle, the energy landscape contains all the information about the rate-dependent properties of the system [7]. Therefore, the dynamic evolution of the system is well described by the low-energy paths connecting equilibrium configurations [28]. Besides, other high-energy paths connecting these equilibrium configurations give little contribution to the rate properties. Therefore, the kinetics of a certain mechanism is determined by the activation energy at the saddle-point connecting the equilibrium configurations.

Several methods have been developed for finding the transition paths (the lowest energy path connecting two energy minima) and a review of such methods is given elsewhere [30]. The calculation of the lowest energy path between two known minima

is very challenging, so that a definitive approach is still to be developed. There are several methods which have been successful, to a certain extent, in finding the optimal path between two known minima [30]. Among those methods the one due to Elber and Karplus [31] is the only systematic way for finding such a path. This method has been recently applied to transitions of point defects in silicon [32, 33]. Although the method can provide reasonably reliable results for the transition path, it is computationally expensive because the calculation involves not only the two equilibrium configurations, but an entire sequence of intermediary states connecting these equilibrium configurations.

We use an alternative way to compute the reaction path connecting two equilibrium configurations. This approach, based on conjugate gradient methods, is considerably more efficient than the EK method.

Consider the energy landscape in a $(3N + 9)$-dimensional space of a N-particle system in a Parrinello-Rahman scheme [22], as described in the previous section. Now consider that a specific transition process corresponds to a path connecting two known minima in that $(3N + 9)$-dimensional space. These two minima correspond to the $(3N + 9)$-vectors $\underline{X}_\alpha$ and $\underline{X}_\beta$ and are reached by specific energy minimization simulations. The line connecting the two minima is $\underline{X}_{\beta\alpha} = \underline{X}_\beta - \underline{X}_\alpha$, and the unit vector connecting the two minima is defined as:

$$\underline{\eta}_{\beta\alpha} = \frac{\underline{X}_\beta - \underline{X}_\alpha}{\|\underline{X}_\beta - \underline{X}_\alpha\|} \quad . \tag{3.2}$$

Now, we use a series of constrained conjugate gradient minimizations to drive the system, starting in the state $\underline{X}_\alpha$ to the state $\underline{X}_\beta$. This is done by using configuration $\underline{X}_\alpha$ as the starting point and displacing the system in direction of $\underline{X}_{\beta\alpha}$ in the $(3N+9)$-dimensional space, which gives configuration $\underline{X}_1$. Then a conjugate gradient relaxation is performed for configuration $\underline{X}_1$ in a sub-space with the constrain that the projection in the direction $\underline{X}_{\beta\alpha}$ is kept constant. This condition is achieved by

removing the forces parallel to the vector $\underline{\eta}_{\beta\alpha}$ as:

$$\underline{g}' = \underline{g} - (\underline{g} \cdot \underline{\eta}_{\beta\alpha})\underline{\eta}_{\beta\alpha} \quad , \tag{3.3}$$

where $\underline{g}$ is the total force in the $(3N+9)$-dimensional space, and $\underline{g}'$ is the force in the subspace normal to $\underline{\eta}_{\beta\alpha}$.

As a result of the energy minimization in this sub-space, the system reaches the configuration $\underline{X}_1'$. Using this configuration as a starting point, we move it again in the direction of $\underline{X}_{\beta\alpha}$ to get configuration $\underline{X}_2$. Again we perform a constrained conjugate gradient minimization as described above and get the relaxed configuration $\underline{X}_2'$.

By systematically repeating the previous steps, we eventually find a low-energy path connecting the $\underline{X}_\alpha$ and $\underline{X}_\beta$. The highest energy of this path defines the activation energy for such specific transition.

The method is found to be reliable in finding the low-energy path connecting the two minima. It is used in Chapter 5 to compute the low-energy path for kink motion. In particular, the results obtained using this method are consistent with other calculations performed with more expensive and sophisticated methods [7].

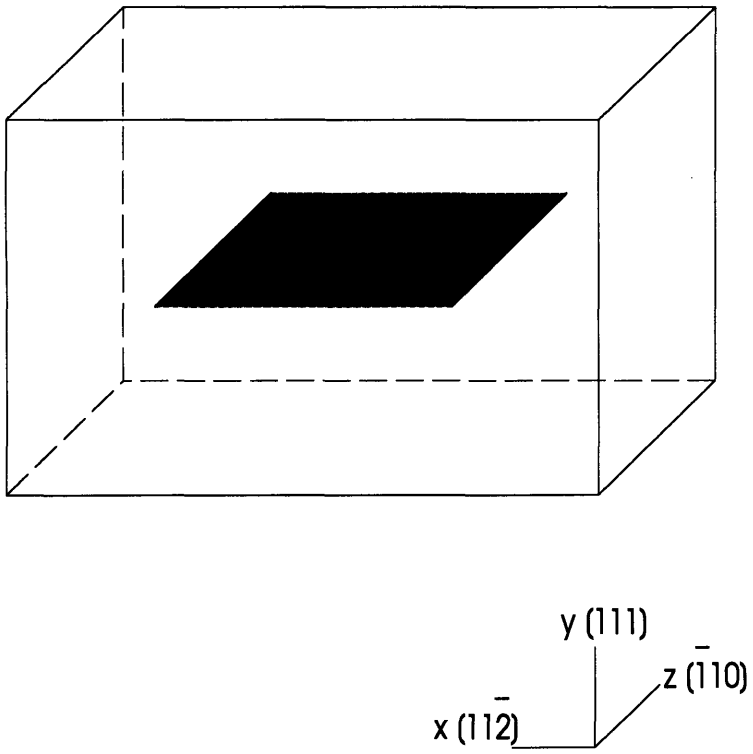

Figure 3-1: Cell geometry used in the simulations of dislocations. The shadowed region represents the stacking fault resulting from the creation of a dislocation dipole.

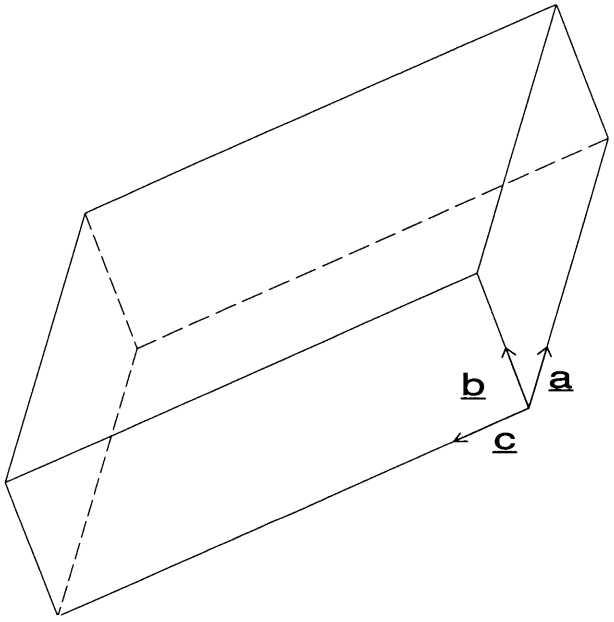

Figure 3-2: Box cell with the three vectors $\underline{a}$, $\underline{b}$, $\underline{c}$ that define the box shape. In a Parrinello-Rahman simulation these vectors obey equations of motion.

Chapter 4

Potential Function for Silicon

4.1 Introduction

First principles quantum-mechanical methods [9] have been widely used in studying microscopic properties of semiconductors. Because these methods require large computational effort, they have been applied only to relatively simple structures, while many other systems of interest, which require thousands to hundreds of thousands of atoms at time scales of 10-100 *ps*, are still out of reach. Empirical potentials, on the other hand, are computationally much less expensive than *ab initio* methods and therefore may represent a valuable tool in investigating such systems. Considering the low computational effort in an atomistic simulation using empirical methods, they may be used for exploration of relevant configurations and processes. Once these relevant structures are identified, the *ab initio* methods may be used for more precise calculations.

The theory of ionic systems and metals has been well established, and empirical models to describe such types of bonding have been successful, for example the shell model [34] for ionic materials and the embedded-atom method [35] for metals. On the other hand, a theory of covalent bonding has not been as successful, and a definitive model is still lacking.

In developing a model for covalent bonding, silicon (Si) has been a prototypical material, and several empirical potentials have been proposed over the last few years. Despite such proliferation of empirical models for covalent bonding, and in particular for silicon, none of the models has been transferable to a number of relevant systems and properties. Generally, the limitations of such models arise from a poor description of the covalent bonding, and each of these models lacks transferability, so that a good description of some configurations generally comes at the expense of the others. Therefore, there has been a great interest in developing a reliable and transferable empirical potential for Si.

In this chapter, we present a new empirical potential for Si. The new model uses a different approach from the previous models: it combines a theoretically motivated functional form and a large database of *ab initio* results for fitting. This chapter is divided as follows: Section 4.2 discusses some of the available empirical potentials for Si and their limitations. Section 4.3 introduces the new model. Sections 4.4 and 4.5 present tests for the new model for bulk and defect structures. Finally, Section 4.6 presents some concluding remarks.

4.2 Survey of Existing Empirical Models for Si

Over the last decade, dozens of empirical potentials for silicon have been developed [38-41,67,69,72]. These models have been applied to a number of different systems, and some of them were recently compared to each other [36, 37]. They differ in degree of sophistication, functional form, range of interaction, and database used for fitting. Although the functional form is important for a potential to be successful in describing a number of different structures, it has been usually chosen a priori with little or no theoretical justification. Of the empirical models developed thus far, the Stillinger-Weber (SW) [38] and the Tersoff [39, 40, 41] potentials have been the most widely used and tested ones [36]. Therefore, we first focus on these two models, to extract the physics underlying the functional form.

4.2.1 The Stillinger-Weber Potential

The Stillinger-Weber potential includes two and three-body cluster expansion terms and was fitted to experimental properties of diamond cubic (DC) and molten silicon [38].

$$U^{SW} = \sum_{i<j} V_2^{SW}(ij) + \sum_{(i<j<k)} V_3^{SW}(ijk), \tag{4.1}$$

where $V_2^{SW}(ij)$ is the interaction between atoms i and j, $V_3^{SW}(ijk)$ is the interaction for atoms i, j and k centered at atom i.

The pair-potential is a sum of attractive and repulsive interaction terms. This term is given by:

$$V_2^{SW} = A\left(\frac{B}{r^4} - 1\right)\exp\left[\sigma/(r_{ij} - a)\right] \qquad r < a\ , \tag{4.2}$$

where $r_{ij} = |\underline{r}_j - \underline{r}_i|$ and a is the cut-off distance. The two-body interaction comprises a strong short-range repulsive force and a longer range attractive force. Figure 4-1 shows the SW two-body interaction. The potential is short-ranged, having the cut-off just short of the second-nearest neighbor distance, i.e. at $3.77\mathring{A}$.

The three-body interaction is introduced to describe strong angular dependent forces and makes the bonding stable at the tetrahedral angle. This term is given by:

$$V_3^{SW} = \lambda(cos\theta_{jik} + 1/3)^2 \exp\left[\gamma/(r_{ij} - a) + \gamma/(r_{ik} - a)\right] \quad r < a\ , \tag{4.3}$$

where θ_{jik} is the angle formed by the $\underline{r}_{ij}$ and $\underline{r}_{ik}$ vectors. Figure 4-2 shows the SW three-body angular term as a function of the angle θ, while Figure 4-3 shows the three-body interaction energy for three atoms at distances $2.35\mathring{A}$ from each other, as a function of the angle. The minimum of this angular term is at the tetrahedral angle $\theta_o = 109.47^o$. Therefore, the three-body interaction penalizes the structures with angles other than θ_o with a considerable positive energy contribution.

The SW potential has six free parameters: A, B, σ, γ, λ, a, which are listed in Table 4.1.

The SW potential has been used to study lattice dynamics [42], point defects [43, 32], liquid [38, 44], amorphous state [45, 46], surfaces reconstruction [47, 48, 49], (100) stepped surfaces [50], epitaxial growth from liquid [51, 52], and the Si bulk phase diagram [44]. The model was extended to germanium (Ge) [53, 54], GaAs [55], CdTe [56], and Si-F systems [57]. An extension of the SW model has been recently proposed for interactions of oxygen in Si [58].

4.2.2 The Tersoff Potential

The Tersoff potential is described by a sum of pseudo-pairwise interactions, including a many-body bond order term [59]. It was fitted to density functional theory (DFT) results for several Si polytypes [39, 40, 41]. The total energy is given by a two-body term depending on the angles between bonds:

$$U^T = \sum_{i,j}{}' \, V_2^T(ij) \quad , \tag{4.4}$$

where:

$$V_2^T(ij) = f_c(r_{ij}) \left[A \, a_{ij} \exp\left(-\lambda_1 r_{ij}\right) - B \, b_{ij} \exp\left(-\lambda_2 r_{ij}\right) \right] \quad , \tag{4.5}$$

$$a_{ij} = \left[1 + \alpha^n \eta_{ij}^n\right]^{-1/2n} \quad , \tag{4.6}$$

$$b_{ij} = \left[1 + \beta^n \zeta_{ij}^n\right]^{-1/2n} \quad , \tag{4.7}$$

and

$$\eta_{ij} = \sum_{k \neq i,j} f_c(r_{ik}) \exp\left[\lambda_3^3 (r_{ij} - r_{ik})^3\right] \quad , \tag{4.8}$$

$$\zeta_{ij} = \sum_{k \neq i,j} f_c(r_{ik}) g(\mu_i) \exp\left[\lambda_3^3 (r_{ij} - r_{ik})^3\right] \quad , \tag{4.9}$$

$$g(\mu_i) = 1 + \left(\frac{c}{d}\right)^2 - \frac{c^2}{d^2 + (h - \mu_i)^2} \quad , \tag{4.10}$$

with $\mu_i = cos\theta_{jik}$ and f_c the cut-off function

$$f_c(r) = \begin{cases} 1 & \text{if } r < R - D \\ \frac{1}{2} - \frac{1}{2}\sin\left[\frac{\pi(r-D)}{2D}\right] & \text{if } R - D < r < R + D \\ 0 & \text{if } r > R + D \end{cases} . \tag{4.11}$$

The potential has eleven free parameters which are listed in Table 4.2.

The Tersoff potential has three versions, usually referred to as T1 [39], T2 [40], and T3 [41]. It has been used to study lattice dynamics [42], clusters [60], point defects [40, 41], liquid and amorphous states [41], crystal stability [61], thermomechanical properties [62], and surface reconstruction [49, 40, 41]. This potential has also been extended to carbon [63], and multicomponent systems (Si-C, Si-Ge) [64, 65]. More recently, the model has been extended for hydrogen in Si [66].

4.2.3 Other Empirical Potentials

The SW and Tersoff models for Si have functional forms with enough flexibility to describe a number of different configurations so that they have been the most widely used and tested of all empirical models. Although they have been extensively used, there are still questions about the transferability [36], as these two models have been shown to be reliable only in configurations close to perfect diamond cubic bonding. Several other models have tried to improve the description of configurations far from the equilibrium, and consequently improve transferability. These models describe the interatomic interaction with the same ideas already incorporated into the SW and Tersoff potentials, but using different functional forms, higher order (up to five-body) expansion terms, increasing the number of fitting parameters, or a larger database.

The Khor and Das Sarma potential [67] was suggested as a universal interatomic potential for tetrahedrally bonded semiconductors. It has been tested mainly for surfaces, including (100) and (111) reconstructions [67] and more recently for a stepped (111) surface [68]. It has not been tested for bulk point defects, or other defect

structures.

The Kaxiras and Pandey (KP) [69] potential was fitted to the DFT calculations of the concerted exchange (CE) mechanism of self-diffusion [70]. The model was successful in predicting static properties of DC structure and the complete path of the concerted exchange. However for point defects the formation energies are too low [36]. It has also been used to study the free energy of the CE mechanism [71].

The Mistriotis, Flytzanis and Farantos (MFF) [72] potential is a modified version of the SW potential, which includes a higher order expansion (four-body terms). The parameters for the potential were fitted to DFT calculations of clusters and the experimental melting temperature. The model was applied to clusters and melting [72], but has not been extensively tested otherwise.

The Bolding and Andersen potential [60] is a sophisticated model which was developed as a generalization of the Tersoff potential. The model includes up to five-body interaction terms and over thirty free parameters. These parameters were fitted to a large database including *ab initio* calculations of bulk and cluster properties. It provides very good description of small clusters, but the formation energies of point defects are not in agreement with DFT calculations. Besides, this model does not provide a good description of elastic properties. Since this model includes five-body interaction terms, it is more computationally expensive than the SW and Tersoff models.

All these models did not provide considerable improvement in the description of local configurations compared to SW and Tersoff, showing that the use of more sophisticated functional forms or larger databases does not necessarily provide a better description of local bonding.

4.3 New Empirical Potential for Si

4.3.1 Functional Form

Considering the lack of transferability of the existing models in describing covalent bonding, it is of interest to develop a new model with the following ingredients: improved description of local structures, theoretically motivated functional form, small number of fitting parameters, and computationally efficient evaluations.

The potential discussed here builds on the earlier work, which elaborated some of the elements of this model [76, 74].

The new model consists of two- and three-body interactions as given by:

$$U = \sum_{\substack{i,j \\ (i \neq j)}} V_2(ij, Z_i) + \sum_{\substack{i,j,k \\ (i<j<k)}} V_3(ijk, Z_i) \quad , \tag{4.12}$$

where $V_2(ij, Z_i)$ is a pair interaction between atoms i and j, and $V_3(ijk, Z_i)$ is a three-body interaction between atoms i, j and k centered at atom i (with coordination Z_i).

First, we define Z_i, the effective coordination of atom i, by:

$$Z_i = \sum_m f(r_{im}) \quad , \tag{4.13}$$

where $f(r_{im})$ is a cut-off function that gives the contribution of each neighbor m to the coordination Z_i, and is given by:

$$f(r) = \begin{cases} 1 & \text{if } r < c \\ e^{\frac{\alpha}{1-1/x^3}} & \text{if } c < r < b \\ 0 & \text{if } r > b \end{cases} \quad , \tag{4.14}$$

where $x = \frac{(r-c)}{(b-c)}$. Figure 4-4 shows the function $f(r)$. A neighbor of atom i at a distance $r < c$ is considered a full neighbor, while the neighbors between c and b give only a partial contribution to Z_i. An atom father than b gives null contribution to

coordination. For the diamond cubic configuration, the coordination function 4.14 gives $Z_i = 4$.

The two-body term $V_2(ij, Z_i)$ was chosen to have a SW-like form, but one which includes a screening (bond-order) term in the attractive interaction [73]. This term is meant to describe the known effect of screen bonding, i.e., as coordination increases the attractive interaction is screened out. This term has the same behavior as the attractive interaction in the Tersoff potential [39], and is motivated by other theoretical considerations [74] in which the attractive interaction was found to be proportional to $1/\sqrt{Z}$ for large coordinations ($Z \geq 4$), where Z is the coordination number [75]. For low coordinations ($Z < 4$) the bond-order term departs from the $1/\sqrt{Z}$ dependence [74]. To remove the unphysical divergence of the term $1/\sqrt{Z}$ at low coordinations, we choose an exponential function instead.

The resulting two-body term is given by:

$$V_2(ij, Z_i) = A \left[\left(\frac{B}{r_{ij}} \right)^{\rho} - e^{-\beta Z_i^2} \right] e^{\sigma/(r_{ij}-a)} \quad . \tag{4.15}$$

It should be pointed out that due to the coordination dependence in the two body interaction, $V_2(ij, Z_i) \neq V_2(ji, Z_j)$, and the sum over neighbors is different from that of the SW sum. Figure 4-1 shows $V_2(r, Z)$ for several coordinations compared to the SW two-body potential V_2^{SW}.

The three-body term is represented by separable radial $R(r_{ij}, r_{ik})$ and angular $G(\theta_{jik}, Z_i)$ functions:

$$V_3(ijk, Z_i) = R(r_{ij}, r_{ik})\ G(\theta_{jik}, Z_i) \tag{4.16}$$

The radial function is exponential, equivalent to the SW radial function:

$$R(r_{ij}, r_{ik}) = e^{\gamma/(r_{ij}-b)} e^{\gamma/(r_{ik}-b)} \tag{4.17}$$

However, the point of significant departure from the SW model is that the angular function is coordination dependent. This introduces two new features compared to

the previous empirical potentials: both the equilibrium angle and the flattening of the angular part become dependent on the coordination Z. The angular function is given by:

$$G(\theta_{jik}, Z_i) = \lambda \left[1 - e^{-Q(Z_i)(\cos(\theta_{jik})+\tau(Z_i))^2}\right] \tag{4.18}$$

where $\tau(Z_i)$ and $Q(Z_i)$ control respectively the equilibrium angle and the flattening of the three-body function for coordination Z_i. The angular functional form used in our model has certain similarity with the one used in the the three-body interaction of the MFF potential [72].

The coordination dependence of τ is theoretically motivated by different hybridization of atomic orbitals for atoms in different environments [76]. When a silicon atom is two-fold coordinated, it forms bonds along two orthogonal p-states, keeping the s-state fully occupied, so that the equilibrium angle is expected to be $\theta_{eq}(2) = 90^o$. When the atom is three-fold coordinated, it forms a sp^2 hybridization, with the expected equilibrium angle $\theta_{eq}(3) = 120^o$. When it is four-fold coordinated, there will be a sp^3 hybridization with the usual equilibrium angle $\theta_{eq}(4) = 109.47^o$ (tetrahedral angle). For six-fold coordination, the equilibrium angle is expected to be along the p-orbitals, and $\theta_{eq}(6) = 90^o$.

Considering these four equilibrium points (for $Z = 2, 3, 4, 6$), and taking $\tau(Z)$ in the form:

$$\tau(Z) = u_1 + u_2(u_3 e^{-u_4 Z} - e^{-2u_4 Z}) \tag{4.19}$$

one can determine the best set of parameters for $u_n (n = 1, 2, 3, 4)$ which fits these points. The parameters are: $u_1 = -0.165799$, $u_2 = 32.557$, $u_3 = 0.286198$, and $u_4 = 0.66$. Figure 4-5 shows a plot of $\tau(Z)$. For $Z_i = 4$, $\tau(4) = 1/3$, and it reduces to the SW equilibrium angle.

Another function in Equation 4.18, $Q(Z) = Q_0\, e^{-\mu Z}$, controls the angular strengthening (or weakening) of bonding as a function of coordination. As coordination increases, the three-body angular function becomes flatter, representing a transition from covalent to metallic bonding.

Figure 4-2 shows the angular part $G(\theta)$ compared to the SW one. Figure 4-3 shows

the three-body term $V_3(ijk, Z_i)$ for different coordinations compared to the SW three-body potential $V_3^{SW}(ijk)$. The SW angular term $G_{SW}(\theta_{jik}) = \lambda_{SW}(\cos(\theta_{jik}) + 1/3)^2$ penalizes configurations with angles smaller than 90^o with a large positive contribution to $V_3^{SW}(ijk)$. On the other hand, the angular term of this new model essentially gives a constant positive contribution at small angles. This is the major departure from the Stillinger-Weber model. In the SW model, configurations departing from the diamond cubic structure are strongly penalized in the three-body interaction, and as consequence the potential is too stiff. In our model, these structures are penalized in both the two and three body interactions.

We also choose to have cut-offs for the two- and three-body interactions, a and b respectively, to be different. Overall, the potential has thirteen adjustable parameters: A, B, ρ, β, σ, a, b, c, λ, γ, Q_o, μ and α.

The Z-dependent terms in the two and three-body iterations will introduce an extra loop in each force calculation. In the case of the three-body loop, it will introduce a four-body loop, making force evaluation more expensive compared to the SW potential. On the other hand, this four-body loop needs to be performed only for those neighbors l of atom i which $\frac{\partial f(r_{il})}{\partial r_{il}} \neq 0$. This happens only when the atoms are in the narrow range $c < r < b$, i.e. only to a small number of the neighbors. Therefore, force evaluations using this new model potential take computer time comparable to force evaluations using the SW potential.

4.3.2 Fitting Procedure and Database

The fitting database is an important ingredient for the development of an interatomic potential. The choice of the database, to some extent, determines the range of configurations in which the model is expected to be reliable. Several previous models [40, 41, 77] had their parameters fitted to high symmetry structures such as face-centered cubic, body-centered cubic, and hexagonal close-packed. Here, we choose not to include such high symmetry configurations since these structures have little in common with more relevant structures. The only regular lattice included in the

database is the DC structure, forced to have the lowest energy. The rest of the database is chosen to include more relevant structures and properties, such as unrelaxed *ab initio* results for bulk properties (cohesive energy and lattice parameter of DC structure), concerted exchange path [70], point defects (vacancy, interstitial tetrahedral and hexagonal), generalized stacking fault energies (GSF) [78], and experimental elastic constants [79]. By fitting to this rich set of configurations and properties we ensure that the potential spans many of the relevant local configurations which eventually broadens the transferability of the model.

The fitting procedure consisted of the following steps. First, we define an object function Φ to be optimized

$$\Phi = \sum_k \left[\frac{R_k - R_k^o}{\sigma_k} \right]^2 \quad . \tag{4.20}$$

The sum runs over all k configurations (or properties) included in the database. The R_k^o is the *ab initio* (or experimental) property, and R_k is the same property computed with this model. σ_k gives the weight of the configuration (or property) k in Φ. To find the best set of parameters which minimizes Φ, we performe simulated annealing optimizations by allowing the thirteen parameters to change simultaneously. Table 4.3 gives the best set of parameters found for this model.

4.4 Tests of the New Potential

In this section, we present the results obtained using the best set of parameters (Table 4.3) for several Si structures (and properties). These results are compared to *ab initio* data (where available) and other empirical potential results.

Table 4.4 gives the diamond cubic structure and the lattice parameter compared to SW [38], Tersoff (T3) [41], tight-binding (TB) [80], and DFT/LDA calculations. For this structure, all empirical models agree very well with the more accurate LDA and TB calculations. Table 4.5 compares results for other high symmetry structures

obtained using this model, *ab initio*, and other empirical models. Although such structures are not included in the database, the new model potential describes them reasonably well.

Most of the existing empirical potentials give poor (or marginally acceptable) description of elastic properties of DC crystal, which directly affects description of the crystal deformation. The shear constant (C_{44}), for example, is crucial for the description of long range elastic interactions [36] and is underestimated by most of these models. Table 4.6 compares elastic constants predicted by this model, computed using the homogeneous deformation method [81], to other empirical potentials and experimental results. Table 4.6 also includes other elastic properties, such as the second shear constant ($C_{11}-C_{12}$) and the Cauchy discrepancy ($\Delta C = C_{12}-C_{44}$), two important parameters in crystal stability analysis [82]. The SW and Tersoff models [36] give a positive value for ΔC in disagreement with the experimental (negative) value, while the TB method overestimates it. This model predicts elastic constants in excellent agreement with the experimental values.

The fitting database also includes unrelaxed structures of point defects, such as vacancy (V), and interstitial in the tetrahedral (I_T) and hexagonal (I_H) configurations. Since point defects involve large lattice relaxations and rebonding, they represent a first test for the transferability of the model in describing local structures. Table 4.7 shows formation energies for the unrelaxed and relaxed structures of vacancy, interstitial tetrahedral, hexagonal and the $< 110 >$ split interstitial for *ab initio*, SW, Tersoff, TB and this model. The formation energies for the relaxed structures, obtained by energy minimization using a conjugate gradient method, are also presented in the table. Although the SW and Tersoff potentials give a marginally acceptable description of the relaxed structures, they clearly do not provide a good description of the energy change upon relaxation. For this model, on the other hand, the relaxation energies are in a closer agreement with the relaxation energies from *ab initio* calculations.

The concerted exchange (CE) process [70] is also included in the database since it has been identified as a competing mechanism for self-diffusion in Si. Most of the

empirical potentials do not give a satisfactory description of the CE path [69]. Figure 4-6 shows the energy calculated along the unrelaxed CE path [69] from LDA calculations, SW, Tersoff and this new potential. The results obtained using this model agree reasonably well with those from DFT calculations, and considerably better than those using SW or Tersoff potentials. For the activation energy of the concerted exchange path, which is an important configuration for calculation of transition rates, this model gives 6.10 eV as compared to 5.47 eV from DFT calculations, 7.80 eV from SW, and 6.50 eV from Tersoff. The activation energy for the relaxed path is 4.08 eV in this model which is in excellent agreement with *ab initio* value of 4.30 eV [70].

The database also included several unrelaxed configurations of the generalized stacking fault (GSF) energy surface, i.e. three points of the the glide set and three points of the shuffle set [78] of the $\{111\}$ glide plane. Figure 4-7 shows the cross sections of glide set GSF surface along the $< 110 >$ and $< 112 >$ directions, compared to DFT and SW calculations. The new model potential is in very good agreement with LDA calculations for the $< 112 >$ cross section, although it underestimates the energy for the $< 110 >$ cross section. Because the potential is short-ranged (the cut-off does not reach the third-neighbors), it gives zero stacking fault energy, compared to the experimental value of 0.006 $eV/\mathring{A}^2$. The SW and Tersoff models, which are also short-ranged, give zero stacking fault energy as well. The TB model [83], on the other hand, gives 0.005 $eV/\mathring{A}^2$, in a better agreement with DFT and experimental results.

Therefore, this new model presents a considerable improvement over existing empirical models in describing bulk structures, elastic constants, point defects, and generalized stacking fault energies.

4.5 Thermal and Vibrational Properties

In the Section 4.4, we have tested the applicability of the new model to zero temperature properties. However, thermomechanical properties are strongly dependent on the temperature of the system. In this section, we test applicability of the new model to finite-temperature thermal properties [84], such as thermal expansion coefficient and the vibrational properties of the crystal.

Thermal properties in semiconductors represent a stringent test for any empirical model due to the singular nature of these properties. While most materials expand with increasing temperature, semiconductors such as Si and Ge have negative thermal expansion coefficient at low temperatures. This unusual negative expansion is believed to be related to the negative Gruneisen parameters [11, 85] of the transverse acoustic (TA) phonons near the Brillouin-zone boundary. A negative thermal-expansion coefficient in Si at temperatures $T < 150K$ has been observed experimentally [86, 87] and confirmed by *ab initio* calculations [88].

To compute vibrational properties and the thermal expansion coefficient we use the quasi-harmonic approximation [11, 88]. The normal modes are obtained by diagonalizing the force-constant matrix:

$$D_{i\alpha j\beta} = \frac{\partial^2 U}{\partial r_{i\alpha} \partial r_{j\beta}} \tag{4.21}$$

where U is the interatomic potential energy, indices i and j ($i, j = 1, 2, ..., N$) denote atom number, α and β denote Cartesian components ($\alpha, \beta = x, y, z$). The phonons are the eigenvectors of the force-constant matrix.

Table 4.8 gives the phonon frequencies for the four modes, transverse acoustic at X, $TA(X)$, transverse optic at X, $TO(X)$, the longitudinal optic and acoustic at X, $LOA(X)$, and the longitudinal-transverse optic at Γ, $LTO(\Gamma)$, for this potential, SW, Tersoff, and TB, as well as the experimental data. The new model overestimates all the phonon frequencies. In particular the frequency of the transverse acoustic mode at X is almost twice the experimental value. This new model gives only a

reasonable description of the phonon frequencies, comparable to the results using SW and Tersoff potentials. Figures 4-9, 4-8, and 4-10 present the phonon dispersion curves for the SW, Tersoff and this model as compared to the experimental data. All three empirical models overestimate TA modes at large wavevectors, again because all these potentials are short-ranged [89].

Next, we use the quasi-harmonic approximation to estimate thermal properties, such as heat capacity and thermal expansion coefficient, at finite temperatures. Within the quasi-harmonic approximation [88, 62], the internal energy is given by:

$$E = U_o + \frac{1}{2}\sum_{k,n}\hbar\omega_n(k) + \sum_{k,n}\frac{\hbar\omega_n(k)}{\exp\left(\frac{\hbar\omega_n(k)}{k_BT}\right)-1}\ , \tag{4.22}$$

where U_o is the static lattice energy, and $\omega_n(k)$ is the phonon frequency of mode n and wave vector k.

Using the same approximation, the free energy of the crystal is given by:

$$F = U_o + \frac{1}{2}\sum_{k,n}\hbar\omega_n(k) + k_BT\sum_{k,n}\ln\left[1-\exp\left(\frac{-\hbar\omega_n(k)}{k_BT}\right)\right]\ . \tag{4.23}$$

The specific heat is then:

$$C_V(T) = \sum_{k,n}C_{vn}(k,T) = \sum_{k,n}\frac{\hbar\omega_n(k)}{V}\frac{d}{dT}\left[\exp\left(\frac{\hbar\omega_n(k)}{k_BT}\right)-1\right]^{-1} \tag{4.24}$$

where $C_{vn}(k,T)$ is the contribution of mode n to the specific heat, and V is the volume.

The Grüneisen parameter is calculated as:

$$\gamma_n(k) = -\frac{d[\ln\omega_n(k)]}{d[\ln V]}\ , \tag{4.25}$$

and the thermal expansion coefficient α may be written as:

$$\alpha(T) = \frac{1}{3B(T)}\sum_{k,n}\gamma_n(k)C_{vn}(k,T)\ , \tag{4.26}$$

where $B(T)$ is the Bulk modulus at temperature T.

Figure 4-11 shows the heat capacity, as computed by equation 4.24, for Tersoff, SW, and this model, compared to experimental results [90]. All models give a very good agreement with experiment.

The Grüneisen parameters are computed from Equation 4.25 and the results presented in Table 4.9. This model provides a poor description of the Grüneisen parameters. Specifically, it underestimates the contribution of the optic modes. The SW model overestimates the contribution of the TA modes but underestimates that of the optic modes. The Tersoff potential overestimates the contribution of all the modes, and the TB method gives the best agreement overall.

The thermal expansion coefficients for this model, SW, and Tersoff are computed using Equation 4.26 and the results are shown in Figure 4-12. This model gives a good description of the thermal expansion coefficient at very low temperatures ($T < 200K$), even providing negative value for α, while the Tersoff and the SW models give a positive contribution in that range of temperature. At higher temperatures, this model underestimates α, the Tersoff model overestimates it, and the SW model gives the best description of α.

We can relate the description of the thermal expansion coefficient to the Grüneisen parameters. It is widely accepted [88, 85] that the TA modes give a major contribution to the behavior of the thermal expansion coefficient, specially at low temperatures where the negative thermal expansion coefficient is due to negative values for γ in the TA mode. The Grüneisen parameters for the TA mode $\gamma_{TA}(X)$ are overestimated by all the empirical models. However, the results also show that the optic modes play an important role in the thermal expansion. This becomes clear if one analyses the case of the SW potential. That model gives a very good description of the thermal expansion coefficient, however it simultaneously overestimates the contribution of the acoustic modes and underestimates the contribution of the optic modes: the first compensates the second, and the model gives a good overal description of α. In the case of our empirical model, the underestimation of the thermal expansion coefficient is directly related to the underestimation of the optic modes. In conclu-

sion, both the acoustic and optic modes play a central role in the description of the thermal expansion coefficient. Therefore, when designing an empirical model, the thermal expansion coefficient is not a robust test for the description of the thermal and vibrational properties. Instead one needs to examine the Grüneisen parameters.

We have so far shown results of the thermal properties by using the quasi-harmonic approximation. However, this approximation is accurate only at low temperatures. As temperature increases, higher-order terms become important, and the approximation breaks down. The quasi-harmonic approximation only gives a lower bound for the thermal expansion coefficient. Molecular dynamics simulations, on the other hand, provide a direct measurement of the thermal expansion coefficient. Therefore, to test our model in the high temperature limit, we performe molecular dynamics simulations at constant temperature and stress using the Parrinello-Rahman method [22] for a system of 216 particles. Starting at low temperatures, we heat up the system and let it equilibrate. Figure 4-13 shows the density of the diamond cubic crystal (in unit of $\mathring{A}^{-3}$) as function of the temperature for this new empirical potential compared to SW and Tersoff potentials, and experimental values. In the region of high temperatures ($T > 500K$), this new model gives a reasonably good description of the density of the material. The Tersoff potential overestimates the thermal expansion and therefore, the system contracts too fast. The SW potential gives the best description of the material density in that temperature range. From the MD simulations, we can conclude that this new potential gives a reasonably good description of the density, and consequently of the thermal expansion coefficient, in the high temperature limit.

We conclude that this new model gives a reasonably good description of the phonon frequencies compared to other empirical models, but it gives poor description of the Grüneisen parameters. For the limit of low temperatures, this new model predicts the negative thermal expansion coefficient which is verified by experimental measurements.

4.6 Core Properties of Dislocations in Si

In the previous sections, we presented tests of this new model for several bulk structures. In this section, we test the applicability of the model to the core properties of dislocations. Specifically, we study the ability of the model to describe reconstruction, the gain in energy as result of reconstruction, and the geometry of the reconstructed core.

Several *ab initio* [18, 91, 92] and tight-binding calculations [83, 93] have been performed for dislocations in silicon. Although such calculations are feasible only for small systems, with a few hundreds of atoms, they provided important information about the core properties of dislocations. On the other hand, calculations involving dislocations require much larger cells owing to the long range interaction of the stress fields, and therefore only less expensive methods, such as empirical potentials, are feasible for such systems. Empirical models have been used to study several aspects of dislocations in silicon [7, 94, 95], however, no single model proved reliable for the description of both long range interactions [94] and the core properties [6] of dislocations. In particular these models do not describe the reconstruction of the dislocation cores [6]. For example, the SW potential predicts correct core reconstruction only for the 30^o-partial dislocation, whereas the Tersoff potential predicts correct reconstruction only for the 90^o-partial. Therefore, the properties related to the dislocation core are a stringent test for the new potential.

In this section, the dislocation properties are examined using energy minimization methods [7] at constant stress [22] for a system of 3600 atoms. The periodic box vectors are chosen to be along $[11\bar{2}]$, $[111]$, and $[\bar{1}10]$. We examine the core reconstruction of the 30^o and 90^o-partial dislocation, and compare the results with those using *ab initio* methods and empirical potentials.

Figure 2-2 shows (a) unreconstructed and (b) reconstructed core structure of a 90^o-partial dislocation. As presented in Chapter 2, the reconstruction energy is the energy difference (per unit length of dislocation) between configurations (a) and (b). Table 4.10 compares the reconstruction energy (in $eV/\mathcal{B}$, where $\mathcal{B}$ is the repeat period

along the dislocation, $\mathcal{B} = 3.84\mathring{A}$) using this model, SW, Tersoff, TB and *ab initio* calculations. Configuration (b) is neither stable nor metastable for the SW potential, i.e. the SW model does not support reconstruction for 90^o-partials [6]. On the other hand, this model predicts that the asymmetric core has an energy lower by 0.80 $eV/\mathcal{B}$ than the symmetric one, in excellent agreement with *ab initio* value of 0.87 $eV/\mathcal{B}$ [18].

In this model, the reconstructed bonds at the atoms in the core of a 90^o-partial dislocation are stretched by 1.7 % compared to the interatomic bond in diamond cubic structure, while *ab initio* [18] and TB calculations give 2.6 % and 3.0 % respectively. For this model, the maximum and minimum bond angles (in the dislocation core) are respectively 145^o and 83^o, compared to *ab initio* calculations [18] ranging from 138^o to 96^o, TB [93] from 135^o to 97^o, and Tersoff [6] from 112^o to 95^o.

Figure 2-3 shows (a) unreconstructed and (b) reconstructed core of a 30^o-partial dislocation. The results for the reconstruction energy from *ab initio*, SW, Tersoff and this model are presented in Table 4.10. The Tersoff potential gives negative reconstruction energy, meaning that the unreconstructed configuration (a) would be the most stable, contrary to experimental and *ab initio* results. Although the SW model gives the correct reconstruction configuration, the reconstruction energy is twice as large as the *ab initio* result [96]. Our model, on the other hand, gives the reconstruction energy in very good agreement with the *ab initio* calculation.

For the 30^o-partial dislocation, the reconstructed bonds in the atoms at the dislocation core are stretched by 2.6%, and the maximum and minimum angles are respectively 122^o and 93^o. The *ab initio* calculations [96] give bond stretching of 4.2% at most, and angle distortion (from the tetrahedral angle) as high as 20^o.

The defects in the core reconstruction are called antiphase defects (APD). Figure 2-4 shows APD configurations in a 30^o-partial (a) and in a 90^o-partial (b), and Table 4.10 gives the APD formation energy. Since SW model does not provide reconstructed configuration for 90^o-partials, there is no APD configuration either. For 30^o-partial dislocation, SW gives an APD formation energy much larger than the *ab initio* value. The Tersoff potential gives a negative value for the APD formation energy of the 30^o-partial and a considerably smaller energy for the APD in a 90^o-partial. This

model gives the APD formation energy in good agreement with *ab initio* results for the 30^o-partial. For the 90^o-partial, there is no *ab initio* calculation available for the APD energy. Our APD energy is somewhat low compared to TB calculations [93].

This model supports reconstruction for both 30^o and 90^o partials, giving reconstruction energies in excellent agreement with *ab initio* values. The atomic distortions (bond and angular distortions) around the dislocation core also give results in very good agreement with *ab initio* calculations. For configurations with unsaturated bonds (APD) the model also predicts correct formation energies. This shows that our model has the required ingredients to describe the atomic distortions around the dislocation cores of partial dislocations.

4.7 Conclusions

In this chapter, we present a new empirical potential for silicon. The model introduces a new functional form that depicts covalent bonding using coordination dependent functions. In the two-body interaction, we introduce a bond-order term in the attractive interaction, so that as coordination increases, the attractive term is screened out. In the three-body interaction, we incorporate several coordination dependent functions to stabilize the structure for different coordinations.

The potential is fitted to a database of *ab initio* calculations that included bulk and defect properties. The resulting model presents a considerable improvement over existing models in describing local structures. Specifically, the model gives a superior description of mechanical properties and point defects in Si. For dislocations, this is the only empirical model that provides full description of the core reconstructions: it predicts the correct reconstruction for both 90^o- and 30^o-partials and the reconstruction energies are in excellent agreement with the *ab initio* results. The bond stretching and angle deformations are also in good agreement with *ab initio* results, pointing to the fact that this model not only predicts energies but also describes well the local bonding configurations.

Table 4.1: Parameters for the Stillinger-Weber model from [36].

$A = 16.31972277\ eV$	$B = 11.60319228\ \mathring{A}^4$	$\lambda = 48.61499998\ eV$
$a = 3.77118\ \mathring{A}$	$\sigma = 2.0951\ \mathring{A}$	$\gamma = 2.51412\ \mathring{A}$

Table 4.2: Parameters for the Tersoff model from [41].

$A = 1830.8\ eV$	$B = 471.18\ eV$	$\lambda = 2.4799\ \mathring{A}^{-1}$
$\mu = 1.7322\ \mathring{A}^{-1}$	$\beta = 1.099 \times 10^{-6}$	$n = 0.78734$
$c = 1.0039 \times 10^5$	$d = 16.218$	$h = -0.59826$
$R = 2.85\ \mathring{A}$	$S = 3.0\ \mathring{A}$	

Table 4.3: Best fit parameters for the new model.

$A = 12.360638\ eV$	$B = 1.6039258\ \AA$	$\rho = 1.3950202$
$a = 3.4557809\ \AA$	$b = 3.1640691\ \AA$	$c = 2.4504896\ \AA$
$\sigma = 1.3386900\ \AA$	$\lambda = 0.4610305\ eV$	$\gamma = 0.2037403\ \AA$
$Q_o = 135.14236$	$\mu = 0.7468472$	$\beta = 0.0063757$
$\alpha = 4.0000000$		

Table 4.4: Diamond cubic bulk properties from DFT calculations, SW, Tersoff (T3), tight-binding (TB) and our model. SW and Tersoff results are from [36], TB results are from [80].

	DFT	SW	T3	TB	This work
E_{DC} (eV)	-4.65	-4.63	-4.63	-4.80	-4.657
a ($\AA$)	5.43	5.43	5.43	5.46	5.43

Table 4.5: Energy and lattice parameters for high symmetry structures. DFT, SW, and Tersoff (T3) calculations are from [36]. Here we consider the face centered cubic (FCC), body centered cubic (BCC), simple cubic (SC) simple hexagonal (SH), and hexagonal close-packed (HCP) structures. $\Delta E = E_c - E_c^{DC}$, where E_c^{DC} and E_c are the cohesive energies for DC (eV/atom) and the high symmetry bulk structure respectively. $a(\mathring{A})$ is the lattice parameter.

		DFT	SW	T3	This work
SC	ΔE	0.348	0.293	0.318	0.237
	a	2.528	2.612	2.544	2.797
BCC	ΔE	0.525	0.300	0.432	0.131
	a	3.088	3.245	3.084	3.114
FCC	ΔE	0.566	0.423	0.761	0.750
	a	3.885	4.147	3.897	3.868
SH	ΔE	0.293	0.403	0.469	0.440
	a	2.639	2.833	2.699	2.740
	c/a	0.940	0.918	0.967	0.890
HCP	ΔE	0.552	0.321	0.761	0.295
	a	2.735	3.647	2.756	2.768
	c/a	1.633	0.884	1.633	1.930

Table 4.6: Elastic constants (given in unit of *Mbar*) for the diamond cubic structure. The experimental values are from [79]. SW and Tersoff (T3) results are from [36], tight-binding (TB) results are from [97].

	Expt.	SW	T3	TB	This work
C_{11}	1.67	1.61	1.43	1.52	1.72
C_{12}	0.65	0.82	0.75	0.57	0.63
C_{44}	0.81	0.60	0.69	0.90	0.72
B	0.99	1.08	0.98	0.89	0.99
$C_{12} - C_{44}$	-0.16	0.22	0.06	-0.33	-0.09
$C_{11} - C_{12}$	1.02	0.79	0.68	0.95	1.09

Table 4.7: Relaxed and unrelaxed formation energies of point defects (in eV). SW and Tersoff (T3) results are from [36], and tight-binding (TB) from [97]. Results for the LDA $< 110 >$ split are from [98]. CE activation energies are from [69].

	DFT	SW	T3	TB	This work
V	3.30	2.82	3.70	3.93	3.49
		4.63	4.10		3.94
I_T	3.70	5.25	3.45	4.42	3.91
		12.21	6.92		5.30
I_H	4.30	6.95	4.61	5.13	5.34
		17.10	8.22		6.19
$< 110 >$	3.30	4.68		3.84	2.96
CE	4.30	4.64			4.08
	5.47	7.90	6.50		6.10

Table 4.8: Phonon frequencies (in THz) for Transverse Acoustic $TA(X)$, tranverse optical $TO(X)$, Longitudinal optical and acoustic $LOA(X)$, and longitudinal-transverse optical $LTO(\Gamma)$ modes. Experimental and SW results are from [36], Tersoff (T3) results are from [62], tight-binding (TB) are from [99].

	Experiment	SW	T3	TB	This work
$\nu_{TA}(X)$	4.4	6.7	6.9	4.96	7.98
$\nu_{TO}(X)$	13.9	15.9	14.9	14.68	15.49
$\nu_{LOA}(X)$	12.3	13.1	12.2	12.33	13.69
$\nu_{LTO}(\Gamma)$	15.3	18.1	16.1	16.70	18.61

Table 4.9: Grüneisen parameters from experiment, SW, Tersoff (T3), tight-binding (TB) and this model [84].

	Experiment	SW	T3	TB	This work
$\gamma_{TA}(X)$	-1.40	-0.04	-0.20	-1.12	-0.34
$\gamma_{TO}(X)$	1.50	0.89	1.60	1.37	0.16
$\gamma_{LOA}(X)$	0.90	0.83	1.27	1.02	0.16
$\gamma_{LTO}(\Gamma)$	0.98	0.80	1.32	0.98	0.12
$\gamma_{TA}(L)$	-1.30	-0.04	-0.31		-0.34

Table 4.10: Reconstruction energy (in $eV/\mathcal{B}$) and APD energy (in eV) for core structures of partial dislocations. Here $\mathcal{B}$ is the repeat distance of a dislocation. The DFT result for reconstruction of the 90^o-partial is from [18], the 30^o-partial is from [92]. SW and Tersoff results are from [6], and TB result for the 90^o partial is from [93].

	DFT	SW	T3	TB	This work
Reconstruction					
90^o-partial	0.87	-	0.37	0.68	0.80
30^o-partial	0.43	0.81	-0.13		0.45
APD					
90^o-partial	> 0.47	-	0.37	1.31	0.65
30^o-partial	0.43	0.84	-0.13		0.48

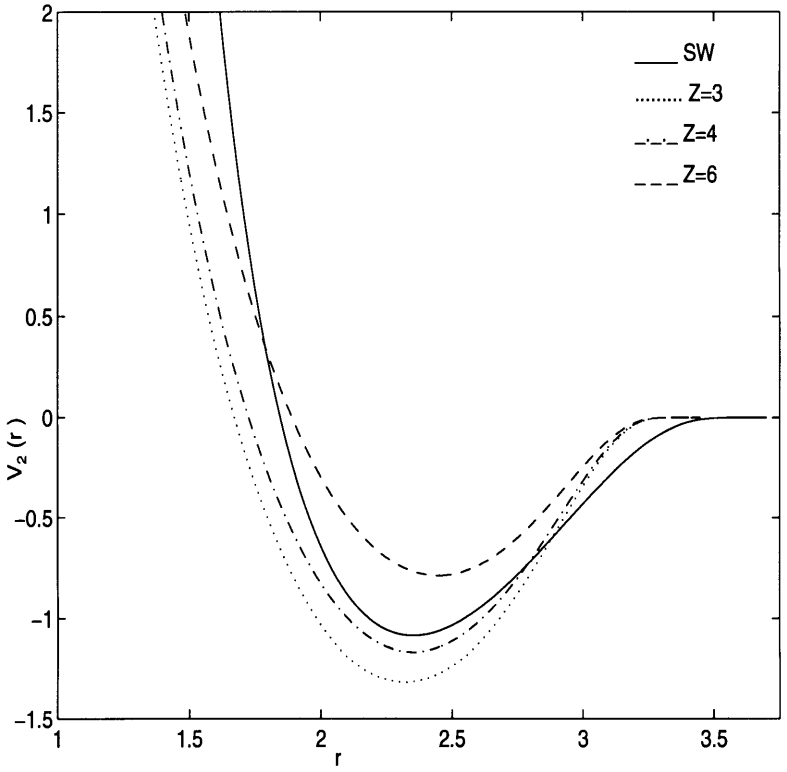

Figure 4-1: Two body interaction term $V_2(r)$ at different coordinations for the new potential, compared to the SW two-body term.

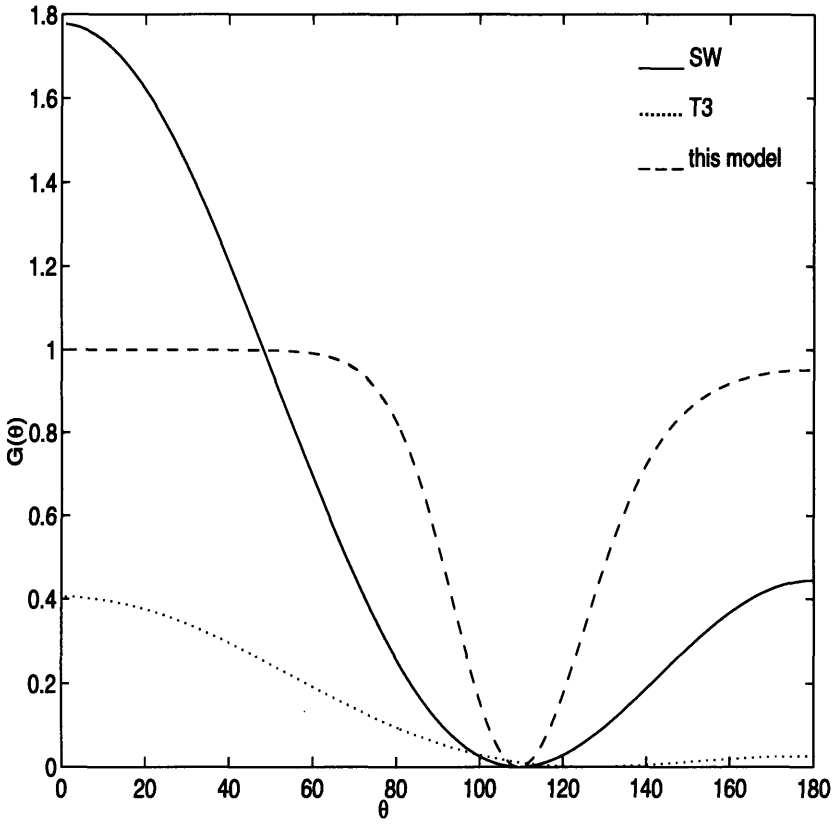

Figure 4-2: $G(\theta)$ of the three-body interaction as function of angle. The term is represented for coordination $Z = 4$ and is compared to the SW and Tersoff (T3) angular terms.

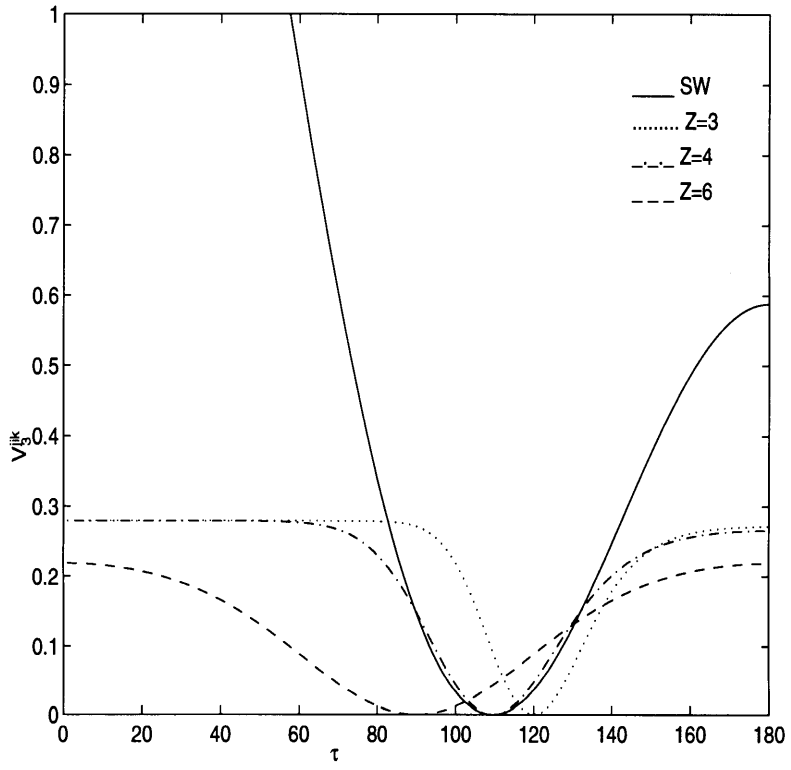

Figure 4-3: Three-body interaction term V_3 as function of angle for a set of three atoms at distances 2.35 $\mathring{A}$. The term is represented for several coordinations and compared to the SW term.

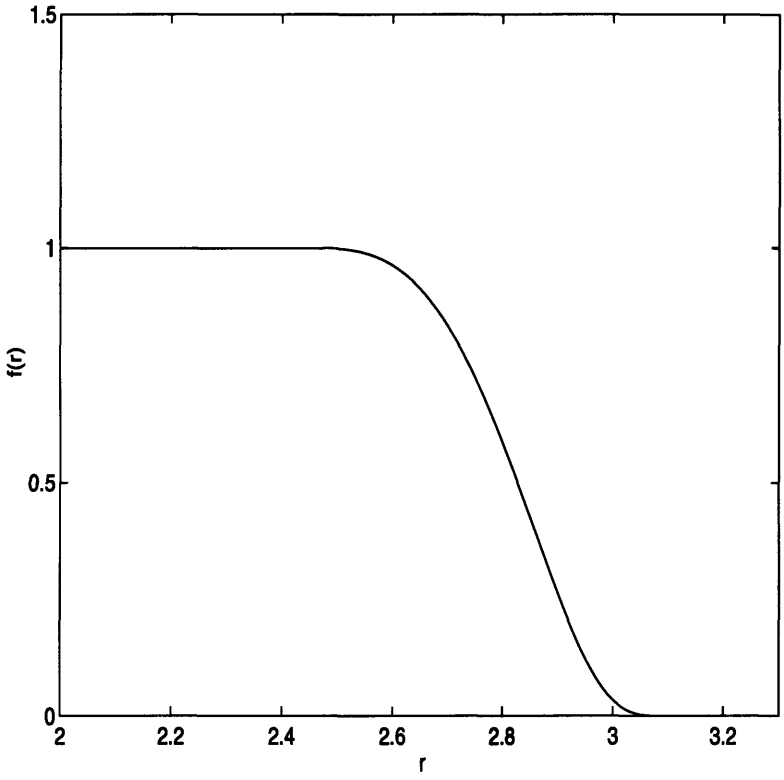

Figure 4-4: Individual coordination function $f(r)$, that determines the contribution of each neighbor to the effective coordination Z.

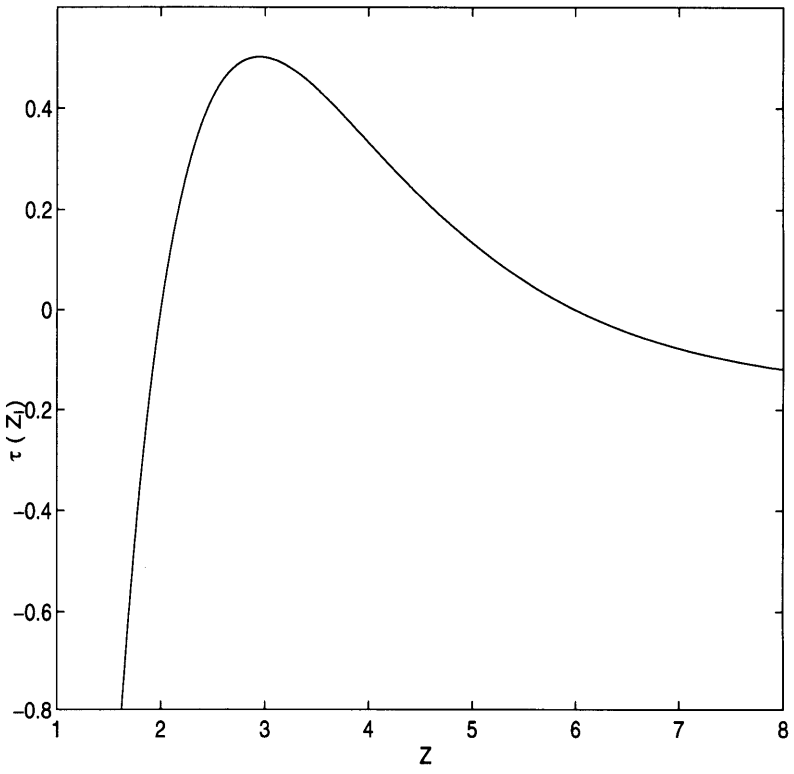

Figure 4-5: Cosine of the optiomal angle $\tau(Z)$ as function of coordination.

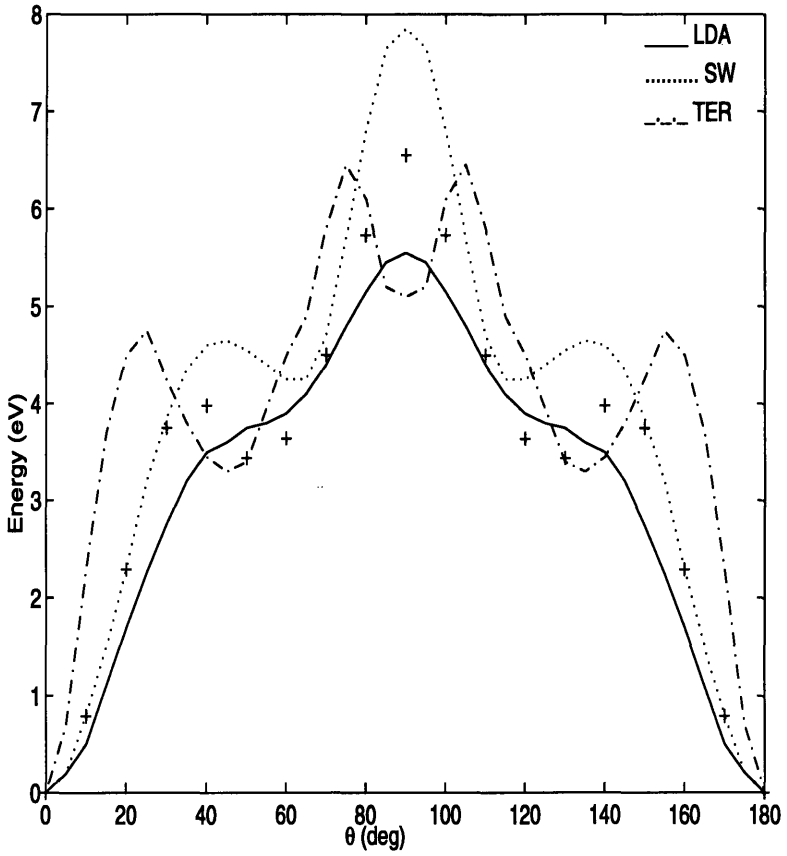

Figure 4-6: Energy of the concerted exchange path for DFT, SW, Tersoff (T3) and this potential. Results from DFT, SW and Tersoff are from [69].

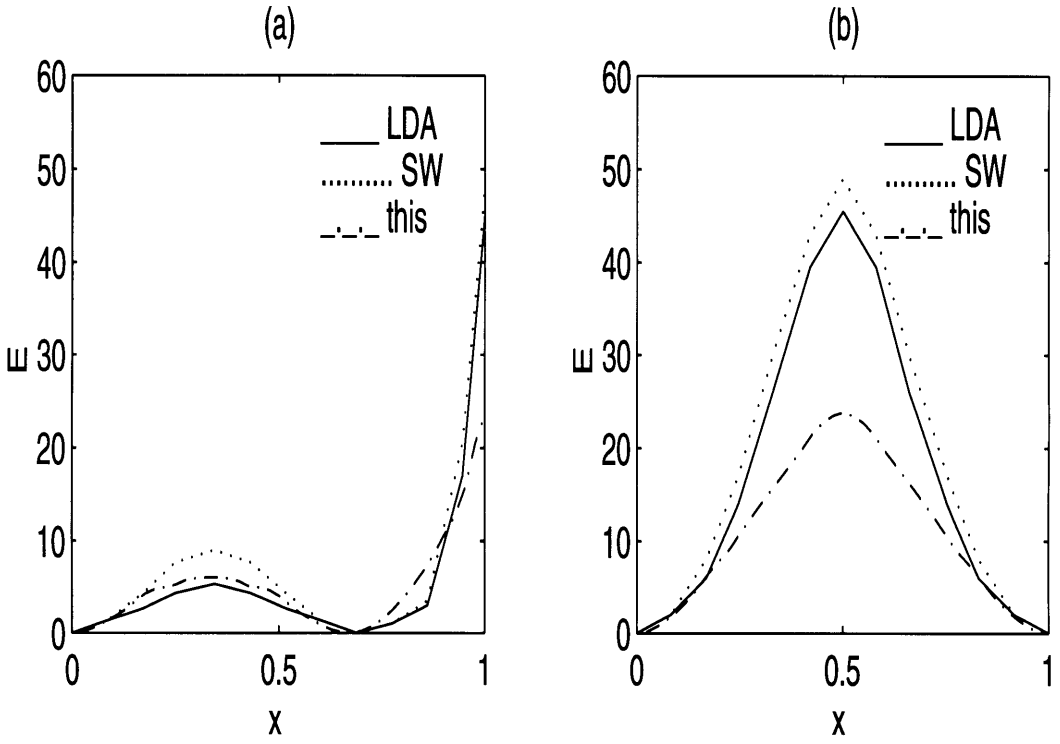

Figure 4-7: Cross section of the Generalized Stacking Fault energy surface for DFT, SW, and this potential. (a) < 112 > and (b) < 110 > directions. Results from DFT and SW are from [100].

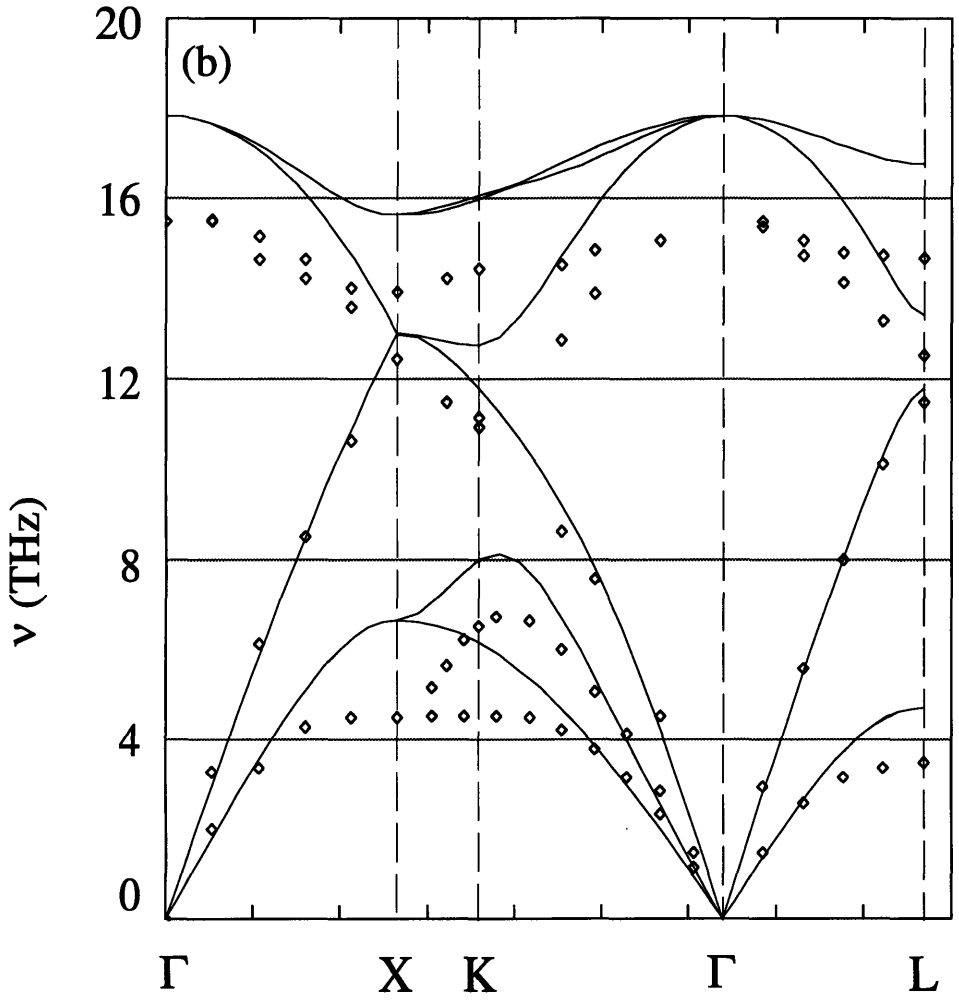

Figure 4-8: Phonon dispersion curve of Si at $0K$ for the SW potential (full line) compared to experimental results ($\diamond$).

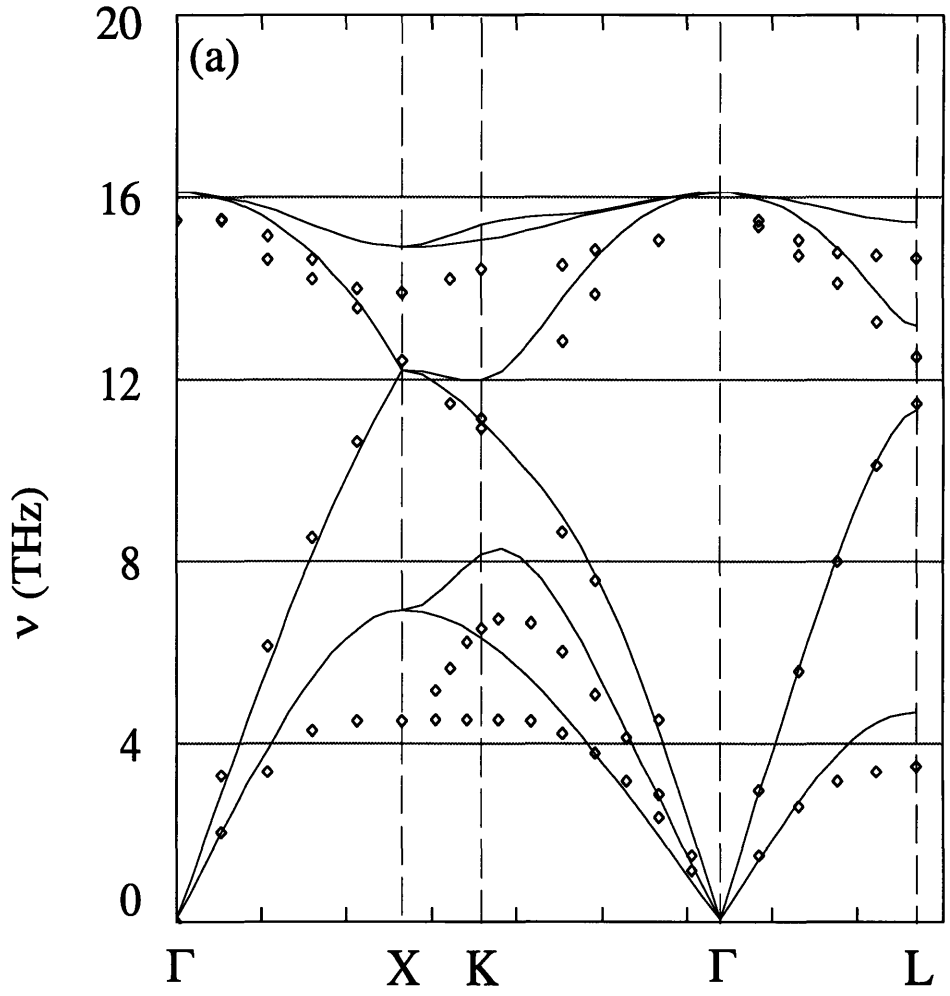

Figure 4-9: Phonon dispersion curve of Si at $0K$ for the Tersoff (T3) potential (full line) compared to experimental results ($\diamond$).

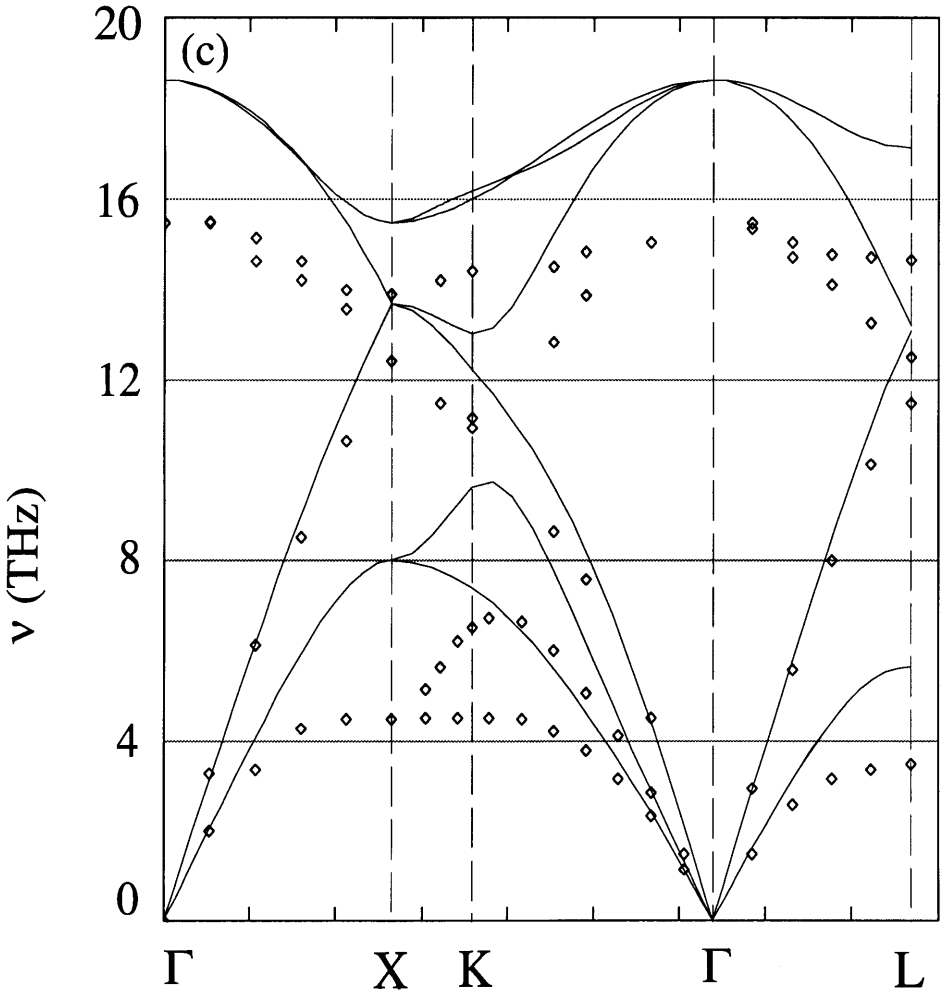

Figure 4-10: Phonon dispersion curve of Si at $0K$ for this new potential (full line) compared to experimental results ($\diamond$).

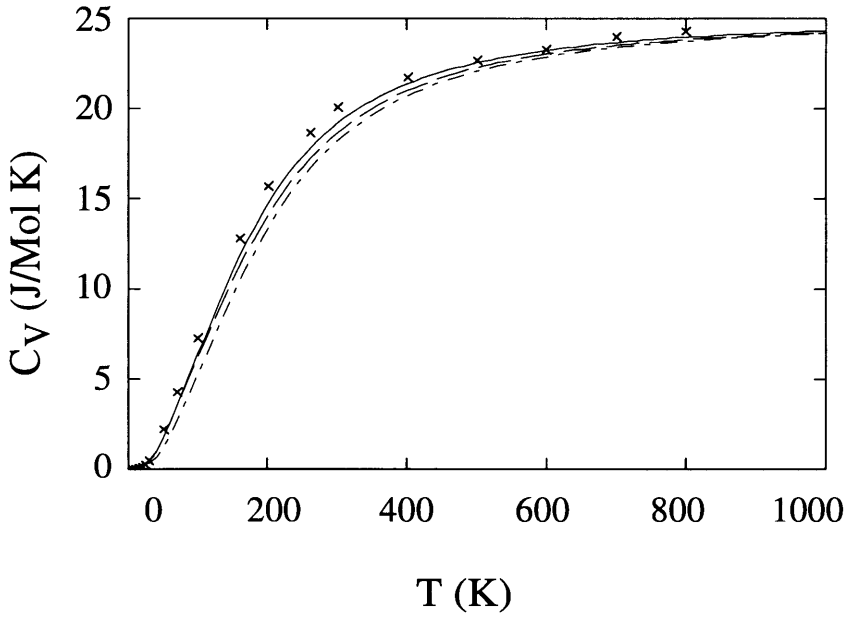

Figure 4-11: Heat capacity C_V as function of temperature obtained from the quasi-harmonic approximation for Tersoff (solid line), SW (dashed line), and this model (dot-dashed line).

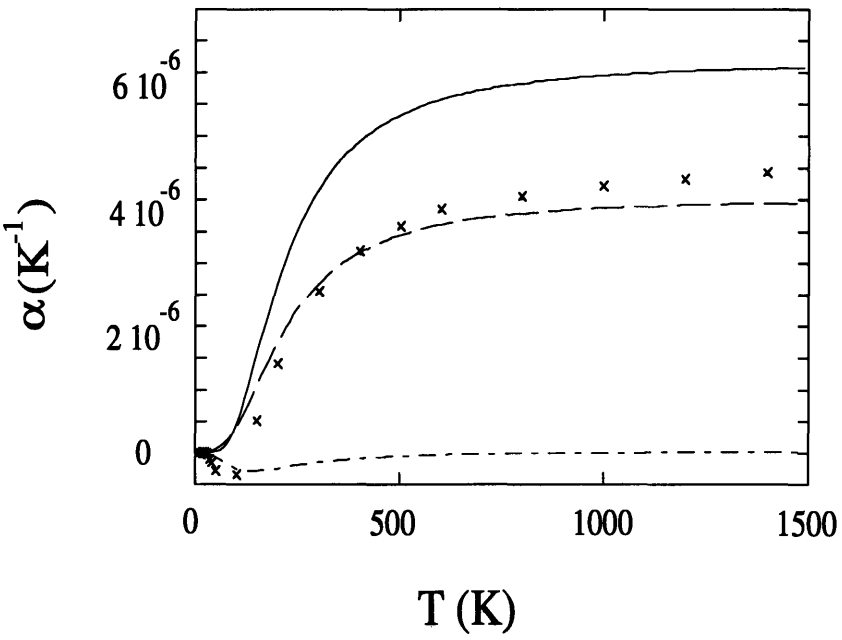

Figure 4-12: Thermal expansion coefficient as function of temperature obtained from the quasi-harmonic approximation for Tersoff (solid line), SW (dashed line), this model (dot-dashed line), and experimental results (crosses).

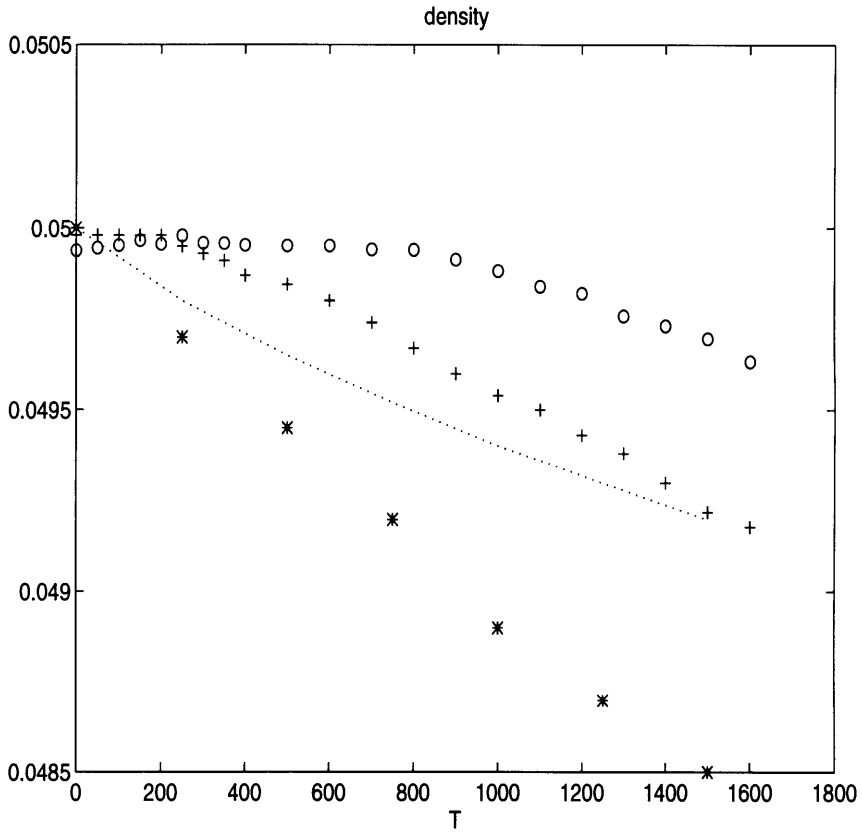

Figure 4-13: Density (in unit of $\AA^3$) of the system as function of temperature for SW (...), Tersoff (*), and this model (o) as compared to experimental results (+).

Chapter 5

Dislocation Core Reconstruction and Its Effect on Dislocation Mobility

5.1 Introduction

Due to their electric activity, dislocations in semiconductors are a source of major concern for developers of electronic devices. One of the key aspects of the device reliability is dislocation mobility. While dislocations in Si do not move at normal operation temperatures ($< 600^oK$), they are highly mobile in III-V and, even more so in II-VI semiconductor compounds. In general, dislocation mobility at a given reduced temperature (T/T_m), where T_m is the melting temperature, increases with increasing bonding ionicity, i.e. on going from the elemental (Si, Ge) to III-V, II-VI and I-VII semiconductors. Since these materials all have zincblende (diamond) crystalline structure, the set of active dislocations in them is the same, as confirmed by experimental observations [3]. It is of great interest then, both from theoretical and practical points of view, to understand why dislocations exhibit such a wide range of mobilities in so similar crystalline structures.

Dislocations in semiconductors are very narrow and their mobilities are controlled by the structure and processes in the atomic core [101]. This is because the strong directional covalent bonding is responsible for the *high primary and secondary* Peierls barriers to dislocation motion. The conventional theory of kink diffusion due to Hirth and Lothe (HL) [10, 101] considers dislocation motion as a net result of the stress-biased thermally activated nucleation and propagation of dislocation double kinks. According to the theory, the velocity v_d of a long dislocation segment at temperature T under applied stress σ is

$$v_d = A\ \sigma e^{-(U_{DK}/2+U_m)/K_BT}\ , \tag{5.1}$$

where U_{DK} is the free energy of double-kink formation, U_m is the kink migration barrier, and A is a constant.

Although this picture captures the essential physics of dislocation motion in semiconductors, it is extremely oversimplified. It does not take into account the details of the atomic structure as the kinks move. A more complete picture of the kink motion should take into account a large number of different processes of motion and interaction with secondary defects, including APD's, point defects, and dopants. It is, therefore, natural to seek an explanation to at least some of those different processes which result in dislocation mobility in terms of variations of kink formation and migration energies within the family of diamond cubic semiconductor materials.

Of the dislocations active in the diamond cubic structure, the primary focus has been on the 30^o and 90^o partial dislocations moving in {111} glide planes. There exists strong experimental evidence of the dominant role that these two dislocations play in the observed dislocation mobility. Due to its simpler structure, it was the 90^o partial which attracted more theoretical effort [18, 93]. Recently, however, atomic mechanisms of motion of the 30^o partial were examined theoretically using empirical interatomic potentials [7] and by parameter-free first principles calculations [96]. The issue of major importance was the (2×1) atomic core reconstruction whereby the core atoms form a sequence of bonded dimers eliminating the dangling bonds and

the associated deep levels in the band gap. The picture emerging from the accurate density functional calculations [18, 96] is that the essential dislocations, i.e. the 90^o and 30^o partials, reconstruct strongly in Si with the energy gain about 0.8 eV per each reconstruction dimer bond. That partial dislocations in Si, Ge, and possibly other diamond cubic semiconductors are reconstructed is also consistent with the whole body of the available experimental and theoretical data [3]. Less clear is whether and how the core reconstruction affects the dislocation mobility. In this chapter, we examine effects of the core reconstruction on the mobility of both 90^o and 30^o partial dislocations in Si. Our goal is to establish, by direct atomistic calculations, a connection between the strength of the core reconstruction and the activation parameters of dislocation mobility in Si and, more generally, in the diamond cubic semiconductors.

This chapter is organized as follows. In Section 5.2, we give a brief description of the methods used in the calculations. Then, in Section 5.3, we show that both kink formation and kink migration energies are determined, to a very significant extent, by the energy required to break the reconstructed dimers in the strongly reconstructed partial dislocation in Si, i.e. by the reconstruction energy. Such observation implies that, although it is determined for a static dislocation, the reconstruction energy is an essential quantitative parameter of dislocation mobility.

5.2 The Model and Numerical Details

For the calculations we employ two interatomic potentials: the standard Stillinger-Weber (SW) potential [38] and the new empirical potential presented in Chapter 4. The SW potential has already been extensively used to study the mechanisms of kink formation and migration for 30^o-partial dislocations [7], and is used as a reference for the calculations using the new empirical potential.

As shown in Chapter 4, this new model gives a considerable improvement over other existing empirical potentials in describing local bonding. Specifically for dislocations, we showed in that chapter that this model gives very good agreement with *ab*

initio results in describing core reconstruction. Therefore, we expect the new potential to provide a realistic description not only of the dislocation core reconstruction but also of other defects in Si. Although the SW potential is presumably less accurate, we intend to gain additional insight by comparing results using SW and the new model for structure and energetics of dislocation core mechanisms. In this comparison, SW results are expected to reflect mostly the generic characteristics of the dislocations related to the prevalent tetrahedral bonding in the diamond cubic lattice, whereas the new model should bear more significance for the specific case of dislocations in Si.

Calculations are performed using a periodically replicated supercell with X, Y, and Z axes parallel to the $[11\bar{2}]$, [111], and $[\bar{1}10]$ directions of the diamond cubic lattice of the Si single crystal, as shown in Chapter 3. The size of the primary cell ranged from 21,000 to 23,000 atoms, depending on the specific task. The atomic positions are relaxed using a conjugate gradient relaxation algorithm until all forces on the atoms were smaller than 10^{-6} $eV/\mathring{A}$. Simultaneously, the shape of the periodic supercell was adjusted using the Parrinello-Rahman method [22] so that all six components of the internal stress would not exceed $10^{-4}eV/\mathring{A}^3$.

To examine the mechanism of kink mobility, we first identify the relevant equilibrium configurations of the kink. Then, to examine low barrier paths for kink formation and migration we use a configuration coordinate approach, as described in Chapter 3. Nevertheless, in the following we shall describe the reaction coordinates in sufficient detail for each relevant atomic mechanism of kink formation and migration. The main goal of the calculations was to examine the mechanisms involved in the motion of kinks and the effects of the core reconstructions on those mechanisms. Two series of calculations are performed for each relevant core mechanism, one for the reconstructed dislocation and another for a completely unreconstructed one. Since the latter is metastable and tends to spontaneously reconstruct in most cases, we had to devise special constraints to study the unreconstructed dislocations. In the following section we discuss the results. First, atomic structure and energy are compared for the two different variants, reconstructed and unreconstructed, of 30^o and 90^o partial

dislocations. Then the mechanisms and the energies of kink formation in the reconstructed partials are contrasted with the corresponding kink formation mechanisms in the unreconstructed dislocations. Finally, the mechanisms of kink migration in the reconstructed partials are compared against the corresponding mechanisms in the unreconstructed dislocations.

5.3 Results and Discussion

Details of atom-atom interactions in the dislocation core are responsible for wide variations of plasticity properties observed among materials belonging to the same crystallography class. Diamond cubic semiconductors, in particular, show rather substantial differences of the temperature and stress dependent plasticity. This, along with the observed strong anisotropy of the plastic flow, suggests that core effects are prominent in this material family. In a sense one can expect that, although there exists a common slip geometry in the DC materials family, much of the material specific plasticity behavior resides in the dislocation cores.

If one uses continuum elasticity solutions for displacement fields in and around the cores of the two essential partials, the resulting atomic configurations are full of dangling bonds, and the core energies are high. Core reconstruction eliminates these dangling bonds, as shown in Figures 2-2 and 2-3. Provided that the energy gain due to pairing of the dangling orbitals is larger that the additional bond distortion energy on going from the unreconstructed to the reconstructed configuration, the reconstruction is favored. That is indeed supported by experimental data [3] suggesting relatively low concentration of unpaired orbitals in the cores of partials in Si and Ge, even at high temperatures. At the same time, it is expected that the strength of the core reconstruction, measured by the reconstruction energy gain, will decrease on going from the elemental semiconductors (Si, Ge) to III-V, II-VI, and I-VII semiconductor compounds. This is because reconstructions in both partial cores occur by bonding together second nearest neighbors in the zincblende structure. Therefore,

a progressively increasing ionic bonding component can eventually suppress bonding between anions or cations and reconstruction will yield no energy gain compared to the unreconstructed core.

The core reconstruction affects the dislocation mobility in the sense that the reconstruction bonds must be broken for the dislocations to move through the lattice. This provides additional resistance to dislocation motion, over and above the usual resistance to the interatomic slip which any dislocation experiences, regardless of the reconstruction. Accurate description of this reconstruction resistance requires a fully atomistic approach, since such atomistic details are generally beyond the scope of the continuum elasticity.

5.3.1 Core reconstruction

The first parameter of interest is the reconstruction energy itself, the energy difference between unreconstructed and reconstructed dislocation cores per unit length of the straight dislocation. For the SW potential, calculations showed that the energy gain due to the 2×1 30^o partial reconstruction is substantial, at $0.81\,eV/\mathcal{B}$, where $\mathcal{B} = 3.84\,\mathring{A}$ is the length of the Burgers vector of a full $a/2[110]$ dislocation. At the same time, the asymmetric core reconstruction in a 90^o partial is not favored and the lowest energy state of this dislocation in the SW model is the symmetric core shown in Fig 2-2a. With the exception of some additional atomic displacements, this unreconstructed configuration looks very similar to what one would obtain by placing atoms in the positions predicted by the continuum solution for the displacement fields around a Volterra dislocation [10]. It can be said, then, that a 90^o partial in the SW model does not reconstruct asymmetrically, in disagreement with DFT results [18]. Using the new empirical model, on the other hand, we showed in Chapter 4 that reconstruction in both dislocations is favored, with $E_{rec}(30^o) = 0.45\,eV/\mathcal{B}$ and $E_{rec}(90^o) = 0.80\,eV/\mathcal{B}$, in very good agreement with *ab initio* results at $0.43\,eV/\mathcal{B}$ [96] and $0.87\,eV/\mathcal{B}$ [18], respectively. Since both reconstruction energies are so high, the reconstructed core configurations shown in Fig 2-3b are viewed in the following as the ground states for

the two partials.

Although structurally the two core reconstructions are quite different, both have reconstruction defects, or topological solitons (APD). These core excitations do not by themselves contribute to the dislocation transport. At the same time, APDs have been found to play an important role in dislocation mobility by mediating formation and motion of dislocation kinks [7]. Therefore, the APD formation energy is an important parameter since it determines the thermal concentration of APDs in the reconstructed cores. The formation energy of an APD in the 30^o partial was found to be $0.84\,eV$ for the SW model and $0.48\,eV$ for our new empirical model. Both numbers are very close to the values of reconstruction energy (per unit length) for this partial, at $0.82\,eV$ (SW) and $0.45\,eV$ (new model). Accordingly, we find that the unreconstructed 30^o partial (Fig. 2-3a) can be reasonably described as a sum of APDs on each atom site in the dislocation core and that the interaction between APDs is weak and short-ranged. The situation in the core of 90^o partial is somewhat different. Again, because the ground state of this core in the SW model is not reconstructed, the APD shown in Fig. 2-4b does not correspond to a core excitation in the SW model. The APD formation energy obtained for the 90^o partial wiht the new empirical potential is $0.65\,eV$ which is lower than the corresponding reconstruction energy per unit length ($0.80\,eV/\mathcal{B}$). The difference can be interpreted as resulting from a more significant interaction of two APDs in this dislocation core where, unlike the 30^o partial, two variants of the reconstruction produce recognizable shear distortions. The values for APD formation energies given above were obtained for APDs placed reasonably far apart, so that they could be considered as isolated.

5.3.2 Kink formation energy

In this section we consider effects of the core reconstruction on kink formation energies in both partials, using both the SW and the new interatomic potential. In order to calculate formation energies of kinks in unreconstructed partials we exercise great caution to prevent the unreconstructed cores from spontaneous reconstruction. These

reconstructions are driven by large energy differences between reconstructed and unreconstructed cores for both 30^o and 90^o partials. Unreconstructed cores, on the other hand, have high energy and can be either unstable or metastable. It turns out that all dislocation cores considered here are metastable in their respective unreconstructed forms, except the 90^o partial in the SW model. However, the barriers separating the metastable (unreconstructed) and stable (reconstructed) configurations are very low, typically a few hundredths of an eV, and the reconstructions often occur spontaneously during the conjugate gradient relaxations. This spontaneous reconstruction is unwanted if the task is to obtain unreconstructed *and* fully relaxed dislocations. In such cases, we prevent spontaneous reconstructions by introducing appropriate constraints in the atomistic simulation.

We begin with a 30^o partial dislocation in the SW model. The formation energy of a double kink in a fully reconstructed (Figure 5-1b) partial is computed by forming a double kink with a separation of 12 $\mathcal{B}$ between the two kinks. At this distance, the kink-kink interaction is determined by the linear elastic theory [10], and is inversely proportional to the kink separation. The double kink formation energy is $1.64\,eV$. This should be compared to $0.15\,eV$ which is required to form the same kink pair in a completely unreconstructed dislocation shown in Fig. 5-1a. The two values show that most of the double-kink formation energy in a 30^o partial (SW) comes from the energy required to break a reconstruction bond when a double-kink is formed ($1.62\,eV$). The rest comes from the long range kink-kink interaction. In other words, reconstruction resistance to double-kink formation greatly exceeds the usual resistance to atom sliding ($0.15\,eV$ in the unreconstructed case). This conclusion is further supported by the values of kink formation energy obtained with the new potential. Here, the formation energy is $1.04\,eV$ for a fully reconstructed 30^o partial and $0.44\,eV$ for the completely unreconstructed case. Therefore, the reconstruction energy per bond ($0.90\,eV$) accounts for most of the double-kink formation energy.

The contribution of reconstruction to the double-kink formation in a 90^o partial, studied for our new model only, is very similar: the energy is $1.33\,eV$ for the reconstructed case (Fig. 5-2b) and $0.70\,eV$ for the unreconstructed case (Fig. 5-2a). Here

again we compute the double kink with a separation of 12 $\mathcal{B}$ between the two kinks. The difference of $0.63\,eV$ is close to the $0.60\,eV$ difference for the case of a 30^o partial discussed above. However, the *non-reconstruction* part of the double-kink formation energy is much larger than in the case of the 30^o partial. It is worth noting that in the case of a 90^o partial, the low energy kinks are such that the sense of reconstruction in two dislocation core segments adjacent to the kinks are opposite (Fig. 5-2a and 5-2b). Such kinks were termed left-right (LR) and right-left (RL) in [93] where a 90^o partial was studied using a semi-empirical TB model. The double-kink formation energy of $1.00\,eV$ given there agrees closely with the present result of $1.33\,eV$. In the SW case, there is no stable asymmetric core configuration which can be compared to the symmetric core. For the latter, the double-kink formation energy is 1.14 eV. The values of the double-kink formation energies, as well as other relevant parameters, are listed for 30^o and 90^o partial dislocations in Tables 5.1 and 5.2, respectively.

5.3.3 Left-right dislocation asymmetry

Another interesting distinction between the two partials is that, unlike a 90^o partial where both LR and RL kinks are essentially the same, the two ends of the double-kink in the 30^o dislocation are different (see Fig. 5-1b) and are distinguished as left kink (LK) and right kink (RK), corresponding to the left and right of Fig. 5-1b. In fact, these two types of kinks have already been identified previously [7]. This left-right intrinsic asymmetry in the 30^o partial dislocation means that it is possible to predict which of the kinks would be left and which right just by considering the direction of the Burgers vector of the 30^o partial and the kink vector. Another type of LR asymmetry was suggested for a $a/2[111]$ screw dislocation in BCC materials [102]. However, the origin of LR asymmetry in BCC and DC materials is completely different. In the present case of a 30^o partial in the diamond cubic lattice the asymmetry is a derivative of the Burgers vector direction, whereas in BCC materials the asymmetry is related to the absence of the mirror symmetry with respect two a $\{111\}$ plane in the BCC lattice itself, even without any dislocations present. Henceforth, we distinguish

these two types of LR asymmetry as lattice asymmetry (BCC case) and dislocation asymmetry (DC case). Accordingly, there should be no LR lattice asymmetry for dislocations in Si which are normally confined to {110} directions ({110} is a mirror symmetry plane of the DC lattice). However, for dislocations with non-zero screw component of the Burgers vector, LR dislocation asymmetry can be observed.

In the present work we examine two essential partial dislocations running along the {110} troughs. Of the two types of partials, only the 30^o partial shows left-right asymmetry of dislocation type, although it may appear that even the 90^o partial kinks are not quite symmetric (RL and LR in Fig. 5-2b). This weak asymmetry is, however, not a function of the dislocation Burgers vector which has no screw component. Rather, it is related to the spontaneous breaking of the mirror symmetry by asymmetric core reconstruction and is, therefore, a function of the local sense of reconstruction. This sense alternates along the dislocation line on every occurrence of LR and RL kinks or reconstruction defects and is not permanently associated with any given dislocation segment. Instead, it is changed easily by passing a reconstruction defect (soliton) or a kink along the line. That this weak asymmetry is a function of the reconstruction only is also supported by the fact that both ends of the double-kink are mirror-twins in the unreconstructed dislocation (Fig. 5-2a). In contrast, the distinction between left and right kinks in a 30^o partial remains even in the unreconstructed core.

In view of the discussed left-right asymmetry in the 30^o partial, it is of interest to try to resolve the individual contributions of LK and RK to the double-kink formation energy. Although LK and RK are always formed in pairs on a straight dislocation, the single kink formation energies may be important in considering mobilities of the threading dislocations [103] near surfaces, where single kinks can form[1]. Also, formation energies of the single kinks should be considered when a dislocation line is running along directions oblique to [110]. In such cases, there should be certain density of geometrically necessary kinks of the prevailing type, left or right, contributing

[1]The problem of kink formation near the surface is a complicated one, since simultaneous formation of additional surface steps and concurrent surface reconstructions should be addressed.

to the dislocation line energy [10].

We calculate single kink formation energies for the 30^o partial dislocation using a periodic supercell which has one of its periodicity vectors along a direction vicinal to $< 110 >$. The ideal diamond cubic configuration is not affected by this choice of the periodicity vectors. At the same time, when a dislocation dipole is introduced, with the dislocations running along $< 110 >$ as usual, there appears a certain offset between the points where the dislocations exit and enter the periodic box. The angle between the vicinal and ideal $< 110 >$ direction is chosen so that the resulting lateral offset is exactly equal to the height of a single kink. Figure 5-3 shows the $\{111\}$ glide plane projection of the simulation cell. After the dipole is introduced and the configuration relaxed, the single kink formation energy is calculated by comparing the excess energy of dislocation dipoles of equal length and width calculated in the rectangular and tilted cells. It turns out that the two kinks appearing on the dislocation dipole are always of the same kind, either both left or both right (30^o partial only), depending on the sign of the offset chosen. Therefore, the single kink formation energy is obtained by dividing the extra energy of the tilted cell by two [2]. The accuracy of this procedure is validated by comparing the sum of individual kink formation energies and the double-kink formation energy presented earlier.

Energies of individual left and right kinks differ significantly for both models. In the SW model, the formation energy of the left kink (LK) is higher ($0.99\,eV$) than that of the right kink (RK, $0.65\,eV$). Their sum is 1.64 eV, exactly equal to the double kink formation energy discussed above. Similar asymmetry is observed in the new empirical potential: the LK energy of $0.65\,eV$ against the RK energy of $0.39\,eV$. The two values sum up to $1.04\,eV$, again exactly the double kink formation energy. For both model potentials, LK has higher formation energy than RK, the difference being about $0.3\,eV$ per kink for both models. This rather substantial energy difference between individual kinks of two kinds implies that, between two vicinal dislocations oriented at a small angle to a $< 110 >$ direction, the one containing

[2]The extra terms of the periodic image interaction between the kinks appear to be small for the cell sizes employed in our calculations.

geometrically necessary kinks of RK type should have lower line energy. Therefore, all other conditions being equal, such dislocations should be easier to form.

5.3.4 The effects of 2×1 core reconstruction on kinks in 30^o partial

Another interesting distinction of 30^o partials, compared to 90^o partials, is that for each kind of kinks, left and right, there are two variants, as illustrated in Fig. 5-1c. The origin of such multiplicity of kink structures is in the 2×1 reconstruction in the core of 30^o partials. Because this reconstruction doubles the repeat distance along the line to $2\mathcal{B}$, the existence of alternative kink structures is dictated by the symmetry of the reconstructed core.

We first consider the case of the left kink (LK), in which two variants were identified, corresponding to two metastable energy minima. The deeper minimum corresponds to the kink LK shown in Fig. 5-1b, and the higher energy state corresponds to the kink LK' shown in Fig. 5-1c. As is seen from the picture, the positions of the two kinks differ by $\mathcal{B}$ which is one half of the full $2\mathcal{B}$ translation period. The energy difference between the two right kinks is $0.42\,eV$ using the SW potential. The LK variant has the lower energy. Likewise, in using the new potential the two kinks are also metastable, the LK variant also being of the lower energy. In this model, however, the energy difference between LK' and LK is more substantial, at $0.84\,eV$. Because of this large energy difference, it was the lower energy form LK that entered the double kink formation energy in the 30^o partial in the discussion above, both for the SW and the new model.

The right kink is also found to have two alternative metastable configurations, RK and RK', Figs. 5-1b and 5-1c respectively. In the SW model, RK is the lower energy form of the right kink, but the energy difference is small, only $0.07\,eV$. In the new model the two kinks are also metastable, but this time it is the RK' kink that has a lower energy, and this difference in energy is significant, at $0.33\,eV$. Keeping

the focus on searching for the lowest energy forms of the kinks, we observe that the lower energy double-kink will include the RK kink in the case of the SW model and the RK' in the case of the new model. Hence, the energies of the double kinks cited above assume different compositions for the two models: DK = LK + RK in the SW model, but DK = LK + RK' in the new model. The energies of these double kinks obtained by direct calculations agree very well with the sums of the individual kink energies, as shown in Table 5.1.

5.3.5 Kink-soliton complexes

As we have already seen in the previous section, the 30^o partial dislocation is more complex than the 90^o partial in that it has four distinctly different kinds of kinks, two left ones and two right ones. The complexity of the 30^o partial does not end here, however, since each kind of kink is found to bind with reconstruction defects or solitons described in the preceding section. In principle, such binding should double again the number of possible kinks, where for each of the four kinks, LK, LK', RK, and RK', there would be a corresponding kink-soliton bound state, or complex. We find, however, that only two such complexes, one for left and one for right kink, can be regarded as stable defects. This is found using both the SW and the new potential models. Considering the fundamental differences between the two empirical potentials used, as described in Chapter 4, this gives strong indication that such defects are not just some feature of a specific empirical potential. In [7] such metastable defect species were identified, and they were termed simply left complex (LC) and right complex (RC), respectively. The other two possible forms of kink-soliton complexes are unstable and correspond to the saddle-points lying on the low energy migration paths connecting two metastable configurations, as discussed in the next section. Figure 5-4 shows (a) the left complex (LC) and (b) the right complex (RC). Altogether out of eight possibilities, we count six metastable defect species of the kink type in just 30^o partial dislocation: LK, LK', RK, RK', LC and RC.

The binding energy for each complex is calculated as the the sum of individual en-

ergies of an appropriate kink and a soliton minus the energy of the resulting complex. For the SW model binding is strong for both left and right complexes, with binding energies at $0.51\,eV$ and $0.84\,eV$ respectively. On the other hand, binding is weaker for the new potential, at $0.24\,eV$ and $0.05\,eV$ for LC and RC, respectively. Each of these kink-soliton complexes, LC and RC, contain a dangling bond which can make their motion easier compared to the regular kinks. The fraction of kinks with dangling bonds, among all kinks, can be estimated by comparing their formation energies to the formation energies of the regular kinks. Taking into account the soliton formation energies and the above cited binding energies, we find that LC has a formation energy of $1.29\,eV$ in the SW model and $0.90\,eV$ in our new model. For both models, the LC formation energy is somewhat higher than the LK formation energy but lower than the LK' formation energy. However, for the RC the two models give qualitatively different predictions: the RC formation energy of $0.63\,eV$ is lower than both the RK and RK' formation energies in the SW model, whereas in the new potential thr RC formation energy of $0.83\,eV$ is higher than both the RK and RK' formation energies.

In the case of a 90^o partial, the set of relevant kink states is significantly simpler since there is no left-right dislocation asymmetry and the reconstruction leaves the periodicity along the line unchanged. Essentially there is only one kind of kink without dangling bonds, shown in Fig. 5-2b. The only variety is brought about by the possibility of kink binding to the soliton. This configuration is only possible in the case of the new empirical potential, since the structure is a result of symmetry breaking in the reconstruction bonding, which is not possible using the SW potential. The resulting kink-soliton complex, termed LL or RR in [93], contains a dangling bond and is shown in Fig. 5-2c . The presence in this kink of a dangling bond makes it similar in that respect to the LC and RC defects in the 30^o partial, although this defect was not recognized as a kink-soliton complex in [93]. The formation energy of the complex is $0.98\,eV$, which is higher than formation energy of a single reconstructed kink, at $0.67\,eV$. Taking into account the soliton formation energy of $0.65\,eV$, the binding energy of the complex is $0.34\,eV$.

The formation of the kink-soliton complexes already shows the richness of pro-

cesses involved in the dislocation core. However, the significance of these complexes for dislocation mobility remains unclear until we examine kink mobility mechanisms in the following section. Here we recap the observed multiplicity of the kink states and their mutual relationships. Tables 5.3 and 5.4 list all the relevant core defects and their formation energies, for both 30^o and 90^o partials, using SW and our new model. Because various core defects have certain unique topological characteristics we find it useful to introduce kink and soliton charges, so that a left kink has a kink charge of -1, a right kink has a kink charge of +1, a soliton has one unit of soliton charge, and so on. The usefulness of such classification was established in [7] by observing that kink and soliton charges are conserved in various defect reactions in the dislocation core.

5.3.6 Kink migration energies

Kink migration along the dislocation line is an important mechanism of dislocation mobility in semiconductors. In particular, it is believed that it is kink migration, rather than the kink formation, which controls the overall rate of dislocation motion under stress. Various experimental observations support this point of view, generally converging on $0.6-0.8\,eV$ for kink formation energy, and $1.3-1.7\,eV$ for kink migration energy in silicon [3, 104, 105]. Here, we define the kink migration energy as the difference between the saddle-point energy and the lowest energy of the kink along a given pathway. Having just discussed the consequences of the core reconstructions in Si on kink formation processes, we present in this section the results for kink migration energies. The focus here is specifically on the kink migration mechanisms in reconstructed and unreconstructed partial dislocations.

In general we find that the core reconstructions affect the kink migration mechanisms even more than the kink nucleation mechanisms. For the 90^o partial using the new potential model, the migration energy for the low energy LR kink is $0.62\,eV$ in the reconstructed partial. Using the same model, in the unreconstructed 90^o partial this kink migration barrier is only $0.14\,eV$. Since in SW model this dislocation does

not reconstruct, we can calculate only the barrier for kink migration in the symmetric (unreconstructed) 90^o partial, at $0.51\,eV$.

The mechanism of kink mobility in the 90^o partial is presented in Figure 5-5. Kink motion along the perfectly reconstructed dislocation core involves breaking and making of reconstructed bonds. This process involves coordinated atomic rearrangements in which a bond is weakening simultaneously to a bond that is forming. In Figure 5-5, the kink motion, which involves motion of the atoms 2 and 3, may be described by breaking the bonds 1-2 and 3-4 and forming the bonds 2-4 and 1-3. The sequence (a,b,c), shown in the figure, illustrates the low energy path for the kink motion, with (b) describing the saddle point configuration for the process. In the case of unreconstructed dislocation, on the other hand, reconstructed bond 1-2 does not exist, the process therefore only involves the breaking of bonding 3-4 and forming of the bond 1-3 but no reconstructed bond. As consequence, the energy barrier for the kink motion in the unreconstructed dislocation is much lower than in the case of reconstructed dislocation.

As was discussed above, several kinks are identified for a 30^o partial: LK, LK', RK, RK', LC, and RC. Of these, only LK and RK can be found in the unreconstructed core. The others exist only because of the core reconstruction: LK' and RK' are the alternative forms of left and right kinks and LC and RC are the products of binding of the left and right kinks with the reconstruction defect (soliton). The structural period in the unreconstructed core is $\mathcal{B}$. Accordingly, both LK and RK move along the line by a series of atomic displacements resulting in kink translation by $\mathcal{B}$. On the other hand, reconstruction doubles the structural periodicity length. Consistently, we find that the motion period becomes $2\,\mathcal{B}$ too. Kink translation occurs now via a series of atomic rearrangements so that a regular kink, say LK moving to the left, transforms first into its alternative form, LK', half a period away ($\mathcal{B}$) to the left. The full translation is completed by LK' transforming back into LK but moving further to the left by another half period $\mathcal{B}$. Therefore, motion takes place in a series LK $\rightarrow$ LK' $\rightarrow$ LK, and the saddle-point states on the pathway separating LK and LK' are identical by the symmetry.

The mechanism of left kink motion in the 30^o partial is presented in Figure 5-6. Kink motion along the perfectly reconstructed dislocation core also involves breaking and making of reconstructed bonds. In Figure 5-6, the kink motion, which involves motion of the atoms 2 and 3, may be described by breaking the bonds 1-2 and 3-4 and forming the bonds 2-4 and 1-3. The sequence (a,b,c), shown in the figure, illustrates the low energy path, with (b) describing the saddle point configuration for the process.

Translation of the right kink in the reconstructed 30^o partial is by a similar series: RK $\rightarrow$ RK' $\rightarrow$ RK Again, there are two saddle points on this path that are identical by symmetry. The mechanism of right kink motion in the 30^o partial is presented in Figure 5-7. In the figure, the kink motion, which involves motion of the atoms 1 and 4, may be described by breaking the bonds 1-3 and 2-4 and forming the bonds 1-2 and 3-4. The sequence (a,b,c), shown in the figure, illustrates that motion, with (b) describing the saddle point configuration for the process.

In the unreconstructed 30^o partial, migration energy for the left kinks is $0.25\,eV$ (SW) and $0.52\,eV$ (new model). In the reconstructed partial, this energy is $0.82\,eV$ (SW) and $1.46\,eV$ (new model). Although the numerical values for the two models are different, the kink migration barrier in the reconstructed case, calculated by subtracting the energy of the LK kink from the saddle-point energy, is considerably higher (roughly three times) than the corresponding unreconstructed value. The difference is even more striking in the case of the right kink. Here, the unreconstructed barriers are only $0.08\,eV$ (SW) and $0.13\,eV$ (new model), but the reconstructed ones are much higher, at $0.74\,eV$ (SW) and $0.89\,eV$ (new model). In the reconstructed case, the lowest energy right kink is RK for the SW model, whereas for the new model it is RK'. Accordingly, the migration barriers are calculated by subtracting the appropriate kink energy, RK for SW and RK' for the new model, from the saddle-point energies.

5.4 Summary

In this chapter, we studied the dislocation mobility by kink mechanisms in Si. We showed, by atomistic calculations, that there is a significant additional resistance to dislocation motion in Si associated with the core reconstructions. The way this resistance comes about is manifold. First, reconstructions change the bonding topology in the core and are responsible for the existence of the whole set of new core defects, or secondary excitations. These include various kinds of kinks and reconstruction defects, as well as their complexes. Therefore, dislocation motion is a complex process not reducible to just formation and motion of one type of kink. Instead, the motion occurs by a series of defect formations, motions, annihilations, and several other defect reactions, that all take place simultaneously and may even compete with each other. The second aspect of the core reconstruction which bears importance for dislocation motion is that the formation energy of the core defects is determined, to a large extent, by the reconstruction energy. The third instance where reconstruction matters is in the kink migration energy most of which is associated with the core reconstruction.

Generally, both kink formation and migration mechanisms involve breaking the reconstruction bonds in the core. If these reconstruction bonds are strong, as they are in Si, the net reconstruction contribution to the resistance to dislocation motion is large. Among the two interatomic potential models employed here, the SW model shows greater effects of core reconstruction on kink formation and migration energies. This might be explained by the known tendency of the SW model to over-penalize any bonding arrangement other than tetrahedral. On the other hand, the new empirical model has been shown to describe various non-tetrahedral bonding environments, including dislocation cores, in a more realistic manner. Nevertheless, core reconstructions determine a major part of resistance to dislocation mobility in Si, even within the more realistic model. We conclude that, even though the reconstruction energy is a static parameter, it is directly related to dislocation mobility in semiconductors. Furthermore, we stipulate that, since reconstructions in the partial dislocation cores

in zincblende materials requires that bonds be formed between anions or between cations, reconstruction should be weakened and eventually suppressed by increasing bond ionicity on going from IV-IV to III-V and further to II-VI and I-VII semiconductors. This effect may be partly responsible for the observed significant variations of dislocation mobility in the zincblende semiconductor family.

Another relevant observation is that, regardless of the strength of core reconstruction in a given material, core excitations with dangling bonds participate actively in dislocation motion. These include various reconstruction defects (solitons) and kink-soliton complexes. Such defects are responsible for the existence of deep levels in the gap and can determine the observed sensitivity of dislocation mobility to doping. Concentration of such "soft" spots in the dislocation core is also determined by the strength of the core reconstructions. Therefore, it is very important, in view of all the reconstruction effects discussed above, that energetics of interatomic interactions in the dislocation core and, in particular, the strength of the core reconstructions, are examined using more accurate state-of-the-art methods of condensed matter theory across the family of diamond cubic semiconductors.

Table 5.1: Reconstruction effects on energetics of core defects in 30^o-partial dislocation.

Model Potential	Line Energy (eV/$\mathcal{B}$)		Double kink formation energy		Left kink migration energy		Right kink migration energy	
	unrec	rec	unrec	rec	unrec	rec	unrec	rec
new model	0.45	0	0.44	1.04	0.52	1.46	0.13	0.89
SW	0.81	0	0.15	1.64	0.25	0.82	0.08	0.74

Table 5.2: Reconstruction effects on energetics of core defects in 90^o-partial dislocation.

Model Potential	Line Energy ($eV/\mathcal{B}$)		Double–kink formation energy		Kink migration energy	
	unrec	rec	unrec	rec	unrec	rec
new model	0.80	0	0.70	1.33	0.14	0.62
SW	———		1.14		0.51	

Table 5.3: Topological charges, formation and migration energy of the core defects in 30^o-partial dislocation (notation as in [7]).

	Soliton charge	Kink charge	Formation energy		Migration energy	
			SW	new model	SW	new model
Soliton	1	0	0.82	0.49	0.17	
LK	0	−1	0.98	0.65	0.82	1.46
LK′	0	−1	1.40	1.49	0.40	1.44
LC	1	−1	1.29	0.90	0.22	
RK	0	+1	0.65	0.72	0.74	0.56
RK′	0	+1	0.72	0.39	0.67	0.89
RC	1	+1	0.63	0.83	1.04	

Table 5.4: Topological charges, formation and migration energy of the core defects in 90°-partial dislocation (notation as in [93]) new model only.

	Soliton charge	Kink charge	Formation energy	Migration energy
Soliton	1	0	0.49	
LR or RL kink	0	±1	0.67	0.62
RR or LL kink	1	±1	0.98	

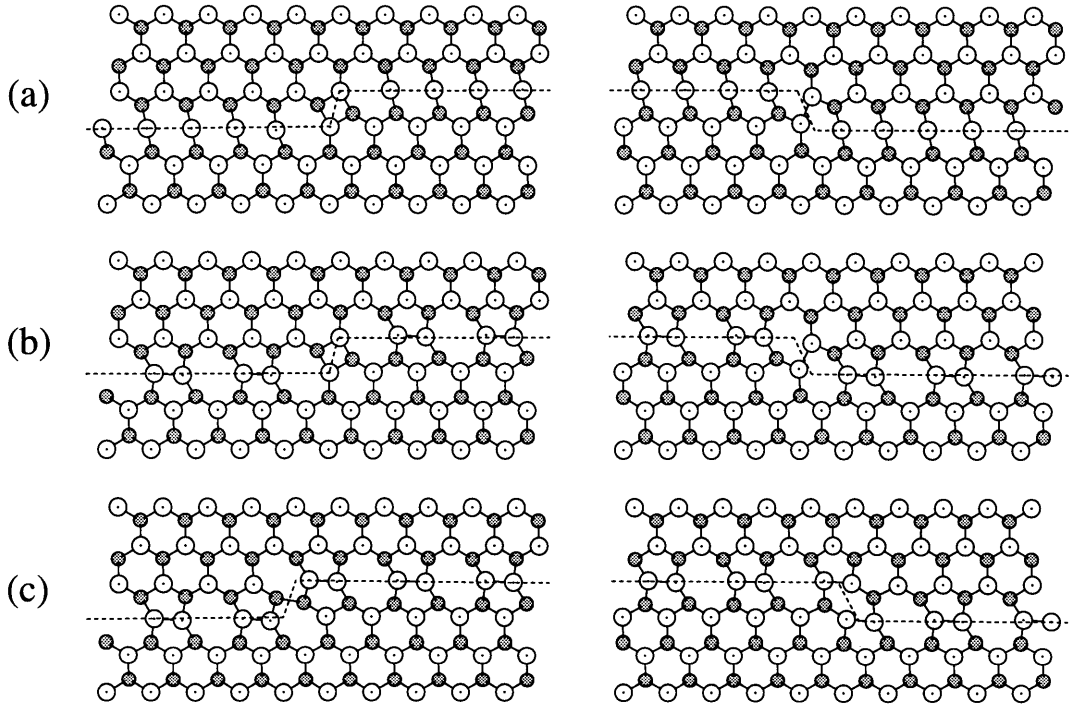

Figure 5-1: Double kink in a 30^o-partial dislocation. The figure on the left and right correspond to the LK and RK respectively. (a) unreconstructed double kink, (b) reconstructed double kink (LK+RK) and (c) reconstructed double kink (LK'+RK').

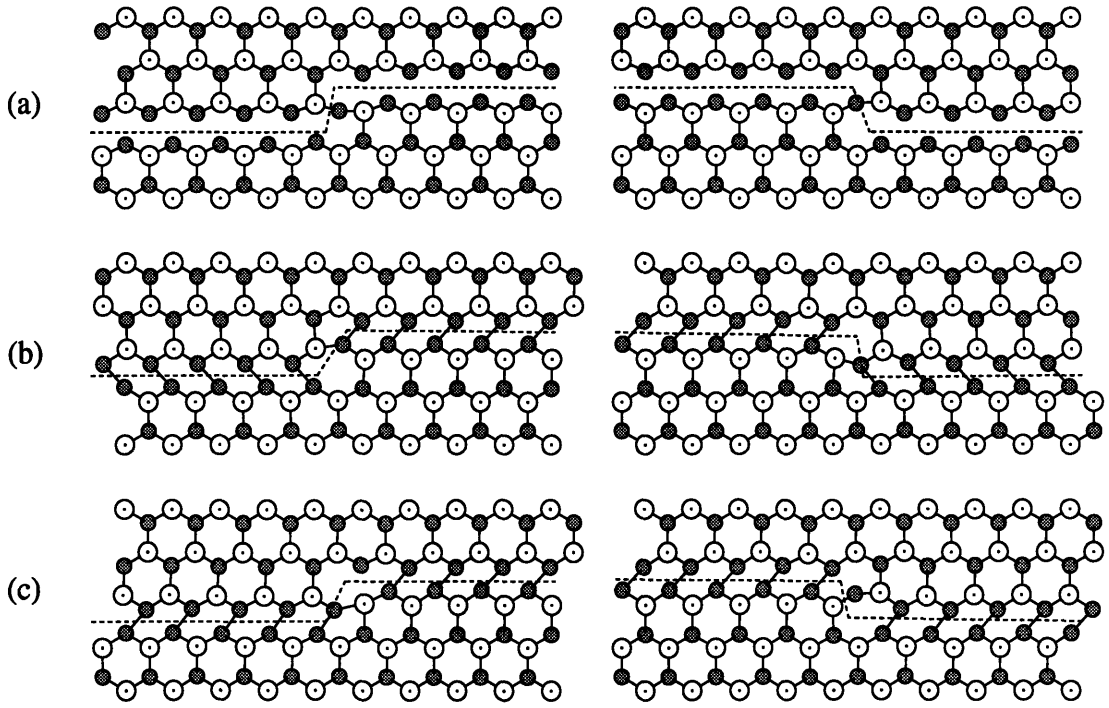

Figure 5-2: Double kink in a 90°-partial dislocation. The figure on the left and right correspond to the LR and RL respectively. (a) unreconstructed double kink, (b) reconstructed double kink (LR+RL) and (c) complexes (LL+RR).

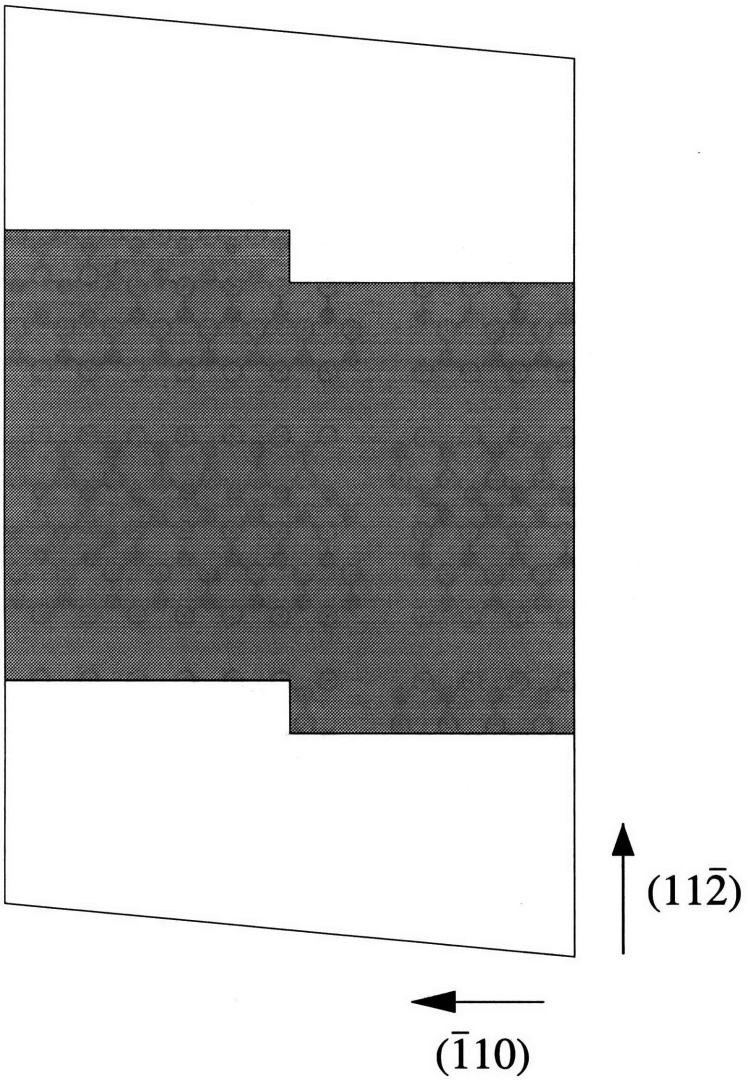

Figure 5-3: Projection of the simulation cell in the the {111} glide plane for calculation of the single kink formation energy. The shaded area represents the stacking fault formed between the two dislocations.

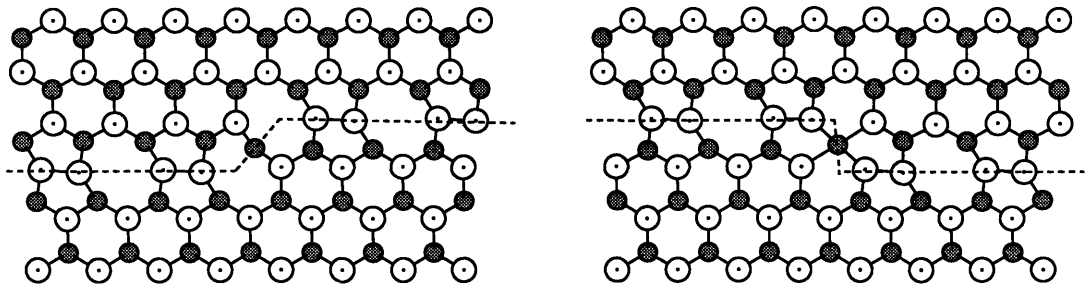

Figure 5-4: Structure of left complex (LC) (a) and right complex (RC) (b) found for both the SW potential and the new model.

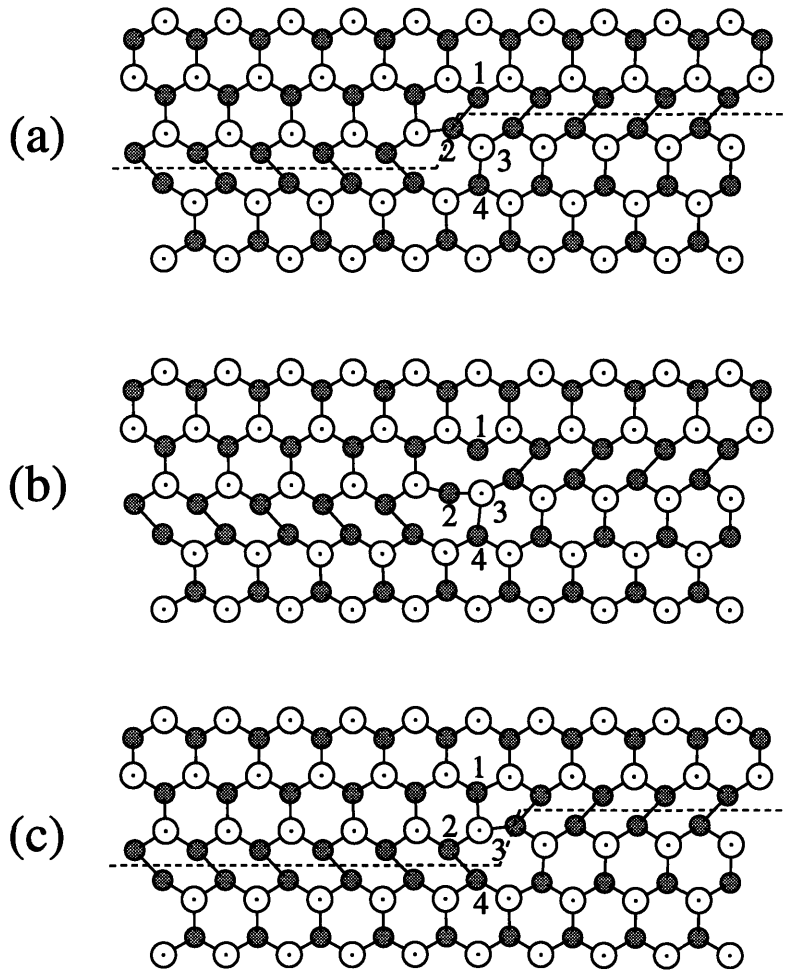

Figure 5-5: Lowest energy path for the motion of LR kink in 90^o partial dislocation.

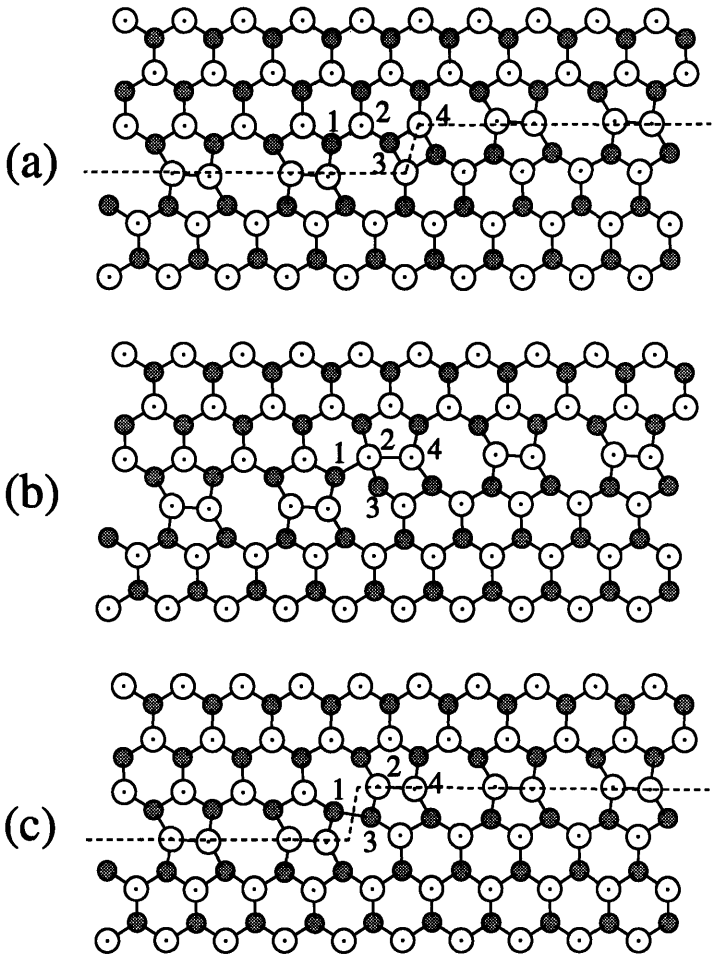

Figure 5-6: Lowest energy path for the motion of left kink (LK $\rightarrow$ LK') in 30^o partial dislocation.

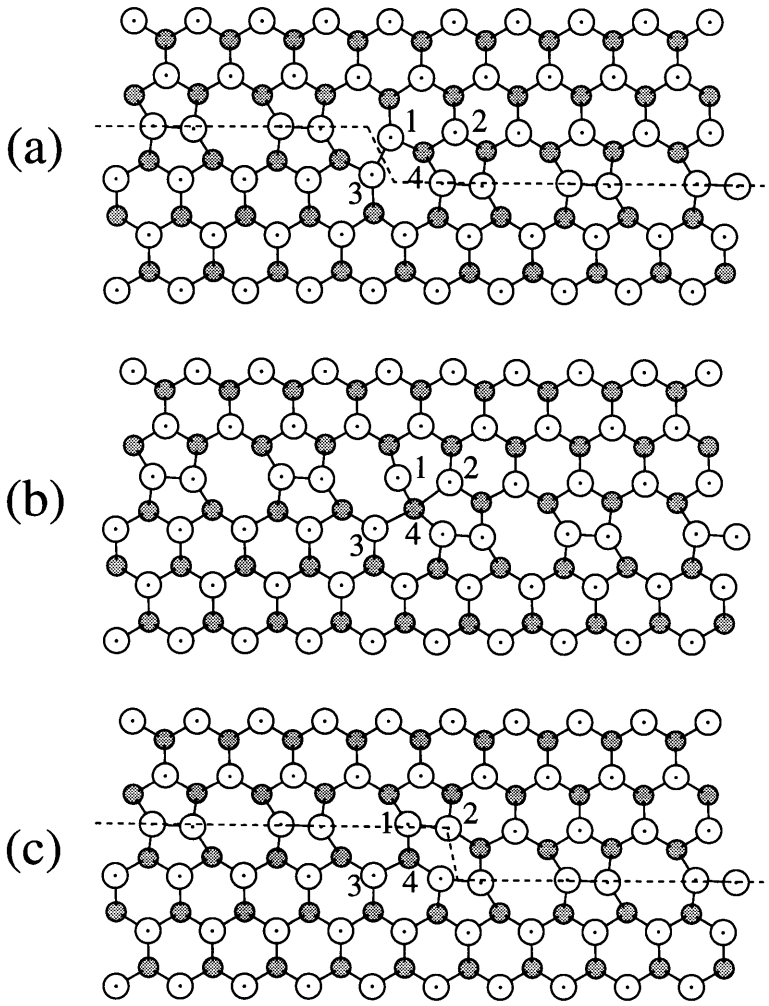

Figure 5-7: Lowest energy path for the motion of right kink (RK $\rightarrow$ RK') in 30^o partial dislocation.

Chapter 6

Core Effects in Dislocation Intersection

6.1 Introduction

As discussed in earlier chapters, dislocations move by formation and propagation of kinks. As dislocations move in the crystal, they intersect with other dislocations, which results in the formation of jogs. These defects resulting from the intersection contribute to resistance to the motion of the dislocation, and play an important role in material plasticity. For example, the rate of strain hardening is controlled, to a large extent, by the interactions of mobile dislocations with forest dislocations [106]. While traditional continuum theory [10] has been successful in describing the long-range elastic strain fields of two intersecting dislocations, the highly nonlinear processes, such as the formation of jogs, kinks, and junctions, which occur during the close encounter of two dislocations have defied quantitative analysis. It has been realized for some time that the core aspects of dislocation intersections can be treated only in an atomistic approach [101]. In this chapter, we consider atomic-level mechanisms of dislocation intersection in Si [107] using the Stillinger and Weber potential [38] and energy minimization methods [7].

Dislocations in semiconductors have high energy barriers for mobility due to the strong covalent bonding. Therefore, at room temperature dislocations essentially do not move. On the other hand, it is known that dislocations are created not only during crystal growth, but also during device operation at higher temperatures [4]. Since dislocations in semiconductors are very narrow with core radius of a few Angstrons, in contrast to metals where dislocation cores are much wider, the region of nonlinear effects involves only a few atomic rows. At the same time, the processes in the core determine a lion's share of the net energetics of dislocation mobility [7]. Considering silicon as a prototype material for a study of dislocation intersection, therefore, has the following advantages: (1) because of the narrow core, dislocations can be packed into relatively small simulation volumes, and (2) the core effects are expected to be prominent in the intersection process of dislocations.

Two issues are addressed in this chapter to some extent: (1) the magnitude of the distance between the intersecting dislocations at which nonlinear interactions become important, and (2) the role of the atomic core reconstruction in the intersection process. Specifically, we consider the intersection of two partial dislocations (both 30^o- or 90^o-partials) lying in two non-parallel planes of the $\{111\}$ type. We observe that the formation of jogs resulting from the intersection is a gradual process, owing to the strong core-core interaction of the two dislocations. We also find that core reconstruction plays an important role in the intersection process. This Chapter is organized as follows. In Section 6.2 we describe the methodology used in the simulations. In Section 6.3, we present the results of the simulations.

6.2 Methodology

To study the intersection of two dislocations we use the Stillinger-Weber empirical potential [38] and energy minimization methods of conjugate gradient and simulated annealing at constant stress [7, 22]. Periodic boundary conditions were used to simulate the bulk of a silicon crystal. Figure 6-1 shows the simulation cell with three

vectors from the $< 110 >$ family, so that all the faces of the resulting trigonal cell are of the same $\{111\}$ type. Two dislocation dipoles are introduced in the glide subsystems of two non-parallel (111) and $(\overline{1}\overline{1}1)$ planes respectively. The shaded regions in the figure represent the stacking faults between the two dislocations in each dipole. This geometry ensures that the glide planes for both dislocation dipoles are parallel to the supercell faces and that all four dislocations are essentially infinite. The convenience of PBC comes with a price: dislocations in the primary cell interact not only with each other but also with all the periodic images of themselves. Since dislocation-dislocation interaction is of long range character [10], the best way to mitigate these unphysical interactions is to use a supercell with dimensions large enough to avoid significant overlap of the non-linear cores of the primary and image dislocations, as well as jogs and kinks that should result from the intersection. The narrowness of the dislocation cores and kinks in Si [15] allows the above requirement to be satisfied using a relatively small supercell defined by the following three basis vectors:

$$\underline{a}_1 = 18\ a\ [\overline{1}10] \qquad \underline{a}_2 = 6\ a\ [\overline{1}0\overline{1}] \qquad \underline{a}_1 = 6\ a\ [01\overline{1}]$$

where $a = 5.43\mathring{A}$ is the lattice parameter of diamond cubic Si. Since the smallest repeat vector of the lattice is $b = a/2 < 110 >$, the dimensions of the supercell, expressed in units of b, are $36 \times 12 \times 12$. In the initial configuration before the intersection (Figure 6-1a), and in the final configuration after the intersection (Figure 6-1b), the distance between any two dislocations in the supercell is no less than 6 b. As found earlier [92], such dimensions are sufficient to avoid core-core overlap, and correspond to a relatively small supercell with only 10368 atoms.

The intersection process was enacted by starting with the two dipoles and moving the leading edge of the dipole in glide plane 1 across the leading dislocation in glide plane 2. Systematic atomistic simulations are performed for dislocation 1 at various equilibrium distances (x) from dislocation 2 before and after their intersection. Here x is defined as the distance (in glide plane 1) between the center of the two intersecting dislocations. At each equilibrium configuration, a conjugate gradient energy

minimization is performed to allow configuration and stress relaxation. Then a simulated annealing calculation is performed only on atoms inside the dislocation cores, so as to account for reconstruction and other rebonding. After allowing core relaxation, another conjugate gradient minimization is performed to fully relax the atoms outside the core in response to core rebonding. The intersection of two dislocations will create defects (kinks and jogs) in both dislocations as given by the geometry of the dislocations [108]. This geometry is defined by the sense of the intersecting dislocations, i.e. by the unit vectors $\underline{\xi}_1$ and $\underline{\xi}_2$ tangent to the dislocation lines, and their Burgers vectors $\underline{b}_1$ and $\underline{b}_2$. After the dislocations cross, each one of them acquires a step ($\underline{d}_i$, $i = 1, 2$) equal in magnitude to the Burgers vector of the other dislocation. If this step lies in the dislocation glide plane it is a kink, otherwise it is a jog. A formal procedure for determining the sign of the intersection kinks (and jogs) was developed by Hornstra [109].

A jog formed on a glissile dislocation may be either glissile or sessile [10]. In the latter case, dislocation mobility is limited by the rate of non-conservative motion of the jog which requires production or absorption of point defects (vacancies or interstitials). On the other hand, motion of kinks and glissile jogs is conservative and does not involve point defects.

To describe the geometry of the intersection process and the defect formed as a result of the intersection for dislocations in the cell described in Figure 6-1, we use the Thompson's tetrahedron shown in Figure 6-2. Thompson's tetrahedron describes all four planes of the $\{111\}$ family in which dislocations glide in the diamond cubic lattice, all six slip directions of the $< 110 >$ family, and Burgers vectors for full and partial dislocations. Partial dislocations have Burgers vectors of $\frac{a}{6} < 112 >$ type. Now considering the geometry of Figure 6-1, the intersection process may be described by a dislocation gliding in a (111) plane until intersection with another dislocation in a $(\bar{1}1\bar{1})$ plane. Figure 6-3 shows two scattering processes of (a) two 30^o-partial dislocations, and (b) two 90^o-partial dislocations intersecting each other. From Thompson's tetrahedron we can obtain the type (kink or jog) of the resulting defect. For example, if the Burgers vector of dislocation 1 ($\underline{b}_1$) belongs to the glide

plane of dislocation 2, then the defect created in dislocation 2 is only a kink, otherwise it is a jog. Table 6.1 lists all possible defects which may form as a result of intersection of two dislocations in the geometry shown in Figure 6-1. Here we consider only two combinations from that list as represented by Figure 6-3: (a) intersection of two non-parallel 30°-partial dislocations, and (b) intersection of two 90°-partials. In both processes, the defects formed in the two dislocations are glissile jogs.

6.3 Results and Discussion

Figure 6-4 shows the formation of in-plane (d_x) and out-of-plane (d_y) components of a jog on dislocation 1 as it moves in its glide plane towards and past dislocation 2 lying in the intersecting plane. Because both dislocations and the jogs are rather narrow in Si, the defect dimensions are reasonably represented by the disregistry acquired, as the two dislocations cross each other, between the two atoms in the same dislocation core but just on opposite sides of the defect. Figure 6-5 shows the final disregistry of the core atoms (in dislocation 1) for both intersection processes (30°-30° and 90°-90°) relative to the geometric center of the defect. Figure 6-4 shows that the defect begins to form even before the dislocation cores intersect and completes only after the dislocations are several Peierls valleys past each other (each point in the figure corresponds to a specific number of Peierls valleys separating the intersecting dislocations). At the geometrical intersection point ($x = 0$) the defect size is only half of the fully formed defect ($x < 0$). This suggests that the defects start to form when the inelastic cores of the intersecting dislocations begin to overlap, i.e. at a distance equal to two core radii, and the process is completed when the dislocations are separated by the same distance. Indeed, the half-widths of the intersection profiles shown in Figure 6-1 are 8$\mathring{A}$ and 14$\mathring{A}$ for the 30°- and 90°-partial pairs respectively. These values may be considered as the distance between dislocations in which nonlinear interactions become important. The latter values correlate rather well with the dislocation core widths of 3.1$\mathring{A}$ and 3.7$\mathring{A}$ calculated earlier for the 30°- and 90°-partials in Si [110].

We conclude that, although there are legitimate concerns about the validity of the Peierls-Nabarro (PN) model [111] for narrow dislocations, the atomistically derived picture of dislocation intersection in Si is consistent with the basic assumption of the PN model, i.e. that dislocations can be represented by distributed dislocation densities spread in their respective glide planes. If so, the defects resulting from the intersection can be viewed as a convolution of two dislocation densities on the two non-parallel glide planes in which the intersecting dislocations are spread. Therefore, it is of interest to attempt to develop a continuum PN-like approach for dislocation intersection.

Table 6.2 gives the final value for the magnitude of the step in dislocation 1 as compared to $\underline{b}_2$. We note that the atomistic step dimensions are smaller than the ideal ones for both dislocation pairs and both in-plane and out-of-plane jog components. This can be attributed to spreading of the fully formed defects along the dislocation lines. The half-widths of the defects in 30^o-partial dislocations are smaller than the corresponding values for 90^o-partials, in agreement with the mentioned narrowness of the 30^o-partials compared to 90^o-partials [110]. That the step size never reaches the ideal amplitude in the calculations is an effect of the PBC, since the two points where each dislocation exits and re-enters the primary supercell are related by a translational vector of the superlattice and, therefore, the disregistry of the two atoms next to the exit/re-entry is forced to be zero. Because the length of this super-translation is not very large, 12 b in the present simulations, the step never reaches the asymptotic ideal dimensions. To mitigate such effects, we use PBC with the Parrinello-Rahman scheme [22] in which the supercell translational vectors can change in order to keep the atomic stress at a given value (zero stress in this case). In the geometry shown in Figure 6-1, the dislocations are initially parallel to the cell edges, i.e. super-translation vectors. After intersection, two of the four dislocations acquire steps which are accommodated by corresponding changes of the box shape taking place in response to the additional stress associated with the changes in those dislocations. Still, this accommodation is incomplete and the defects remain partially suppressed. On the other hand, the suppressive effect of PBC is much greater when no relaxation of the box shape is

allowed. In the latter case, we have to use larger supercells to avoid suppression of the intersection defect. We emphasize that the choice of PBC with variable box shape was instrumental in obtaining a reasonable description of dislocation intersection.

As pointed out earlier, the atomistically derived picture of dislocation intersection is consistent, in general, with the distributed nature of dislocations in the PN model. At the same time, details of atomic structure, such as core reconstructions, can not be described within such model. Since it was found that the Stillinger-Weber (SW) potential describes satisfactorily the core reconstruction for 30^o-partials [6], we proceed to study the effect of core reconstruction in the 30^o-30^o process. (2×1) reconstruction results in the formation of atomic pairs (dimers) in the core of 30^o-partials [6], eliminating the dangling bonds which would be otherwise present in the core. Considering the intersection of two reconstructed 30^o-partials, there are different final situations: (1) both dislocations cut through each other through the reconstruction dimers, (2) only one dislocation cuts through while the other one cuts between the dimers, and (3) both dislocations cut between the dimers. The last situation was found to be the energetically favored one since the energy required to break a dimer bond is very large ($1.64\,eV$ for the SW model). Figure 6-6a shows the atomic core structure of a 30^o-partial dislocation just before intersection with another 30^o-partial dislocation (not shown). The same dislocation is shown just after the intersecting dislocation cuts through a dimer bond in Figure 6-6b and between two dimers Figure 6-6c. The energy of the last configuration (in which the defect forms between two dimers) is lower by $1.48\,eV$ than the energy of the configuration shown in Figure 6-6b. We interpret this appreciable energy difference as an indication that only cutting between reconstruction dimers (as in Fig. 6-6c) is a plausible scenario of intersection for two 30^o-partials, due to the relative ease with which the dimerization sequence changes within each dislocation. Indeed, as found in [7], the dimerization sequence (reconstruction phase) changes from one alternative (Fig. 6-6b) to another (Fig.6-6c) by fast moving reconstruction defects always present in the core at equilibrium concentrations. Because the activation barrier for motion of reconstruction defects is low, at 0.2 eV, the phase of the reconstruction should adjust to the approaching dislocation

so that a configuration similar to the one shown in Fig. 6-6c results. This shows that the reconstruction plays an important role in the intersection of two dislocations.

6.4 Summary

In summary, we have demonstrated the feasibility of atomistic simulations for the study of dislocation intersections. Through the specific examples of partial dislocations in Si, we have examined the mechanisms of intersection in full atomistic detail. We have also shown that formation of the intersection defects can be viewed as a convolution of two dislocation densities distributed in two non-parallel glide planes, in agreement with the quasi-continuum Peierls concept. On the other hand, energetics of the intersections is strongly dependent on the details of atomistic structure in the core, such as core reconstruction, which can be addressed only within a fully atomistic approach.

Table 6.1: Scattering processes between two dislocations, based on the Tompson's Tetrahedra [10] for two dislocations in the planes shown in Fig. 6-1 . K and J denote respectively the kink and jog formed in a dislocation as result of the intersection.

dislocation 1	dislocation 2	d_1	d_2
30^o	30^o	J	J
30^o	90^o	J	J
30^o	60^o	K	J
		J	J
30^o	screw	J	J
90^o	90^o	J	J
90^o	60^o	K	J
		J	J
90^o	screw	J	J
60^o	60^o	J	J
		K	K
		J	K
		K	J
60^o	screw	J	K
		J	J
screw	screw	J	J

Table 6.2: Comparison of simulation results for defect formation with the value expected theoretically (d^{th}). Here the x- and y-components give the in-plane and out-of-plane contributions respectively in the defect on dislocation 1.

dislocations	d_x^{th} ($\mathring{A}$)	d_x ($\mathring{A}$)	d_y^{th} ($\mathring{A}$)	d_y ($\mathring{A}$)
$30^o - 30^o$	-1.47	-1.28	-1.04	-0.63
$90^o - 90^o$	1.84	1.02	-1.04	-0.53

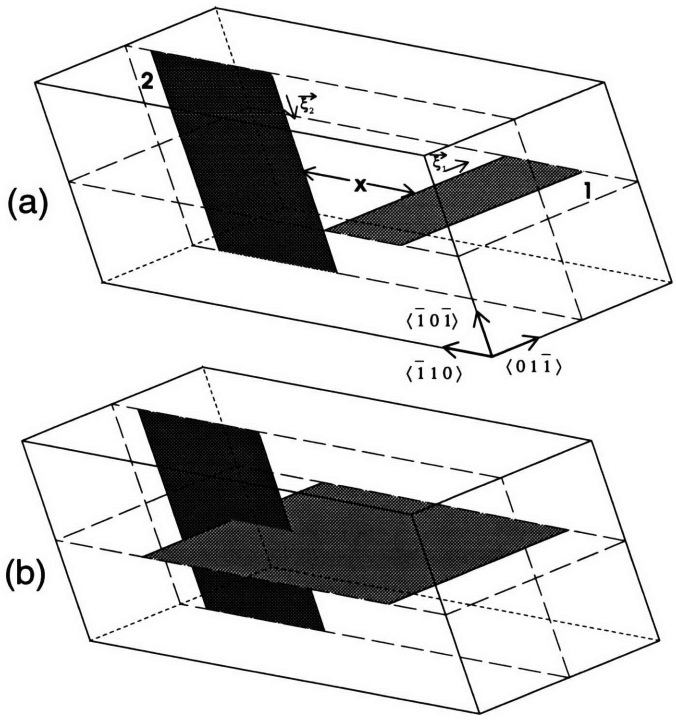

Figure 6-1: Cell construction for the intersection process. Dislocation 1 with Burgers vector b_1 and dislocation line vector ξ_1 is created in glide plane 1, similarly dislocation 2 in glide plane 2, before the intersection (a) and in the process of intersection (b). In a cartesian coordinate system, the dislocation dipole 1 is in the XZ plane and dislocation 1 lies in Z-direction.

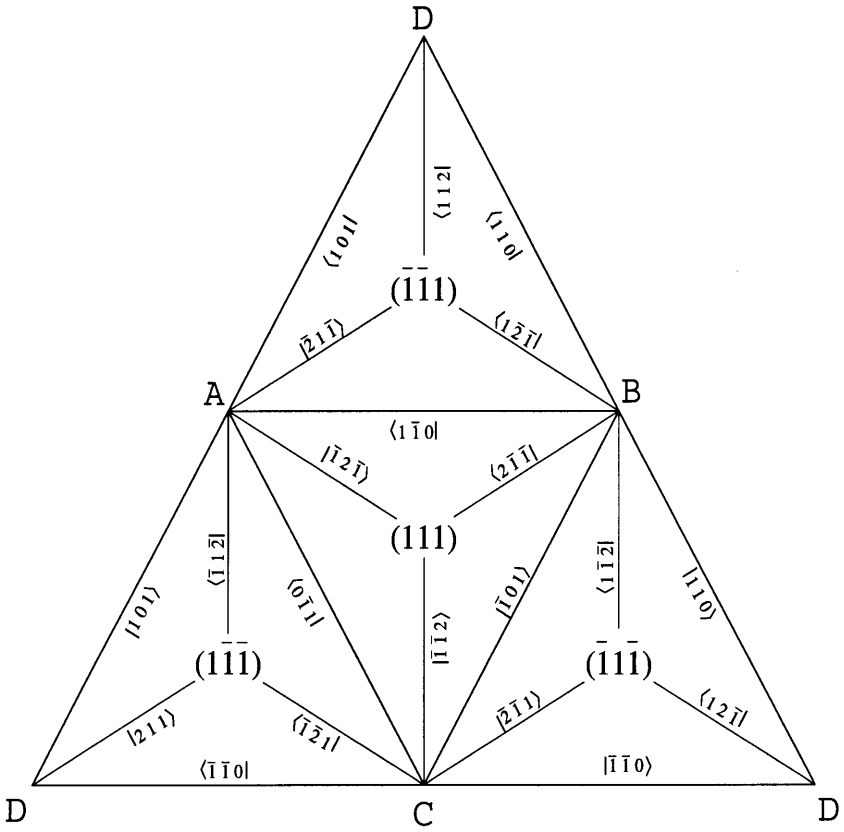

Figure 6-2: Thompson's tetrahedron.

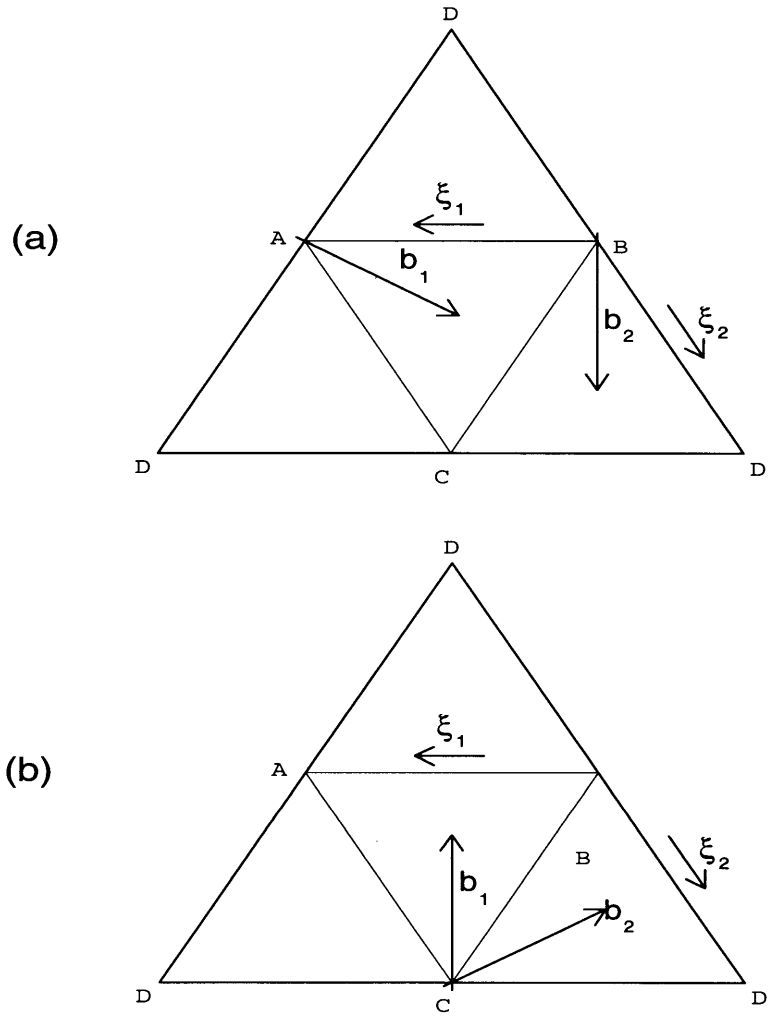

Figure 6-3: Scattering process of two dislocation represented in Thompson's tetrahedron. (a) $30^o - 30^o$ partial dislocation process, and (b) $90^o - 90^o$ partial dislocation process.

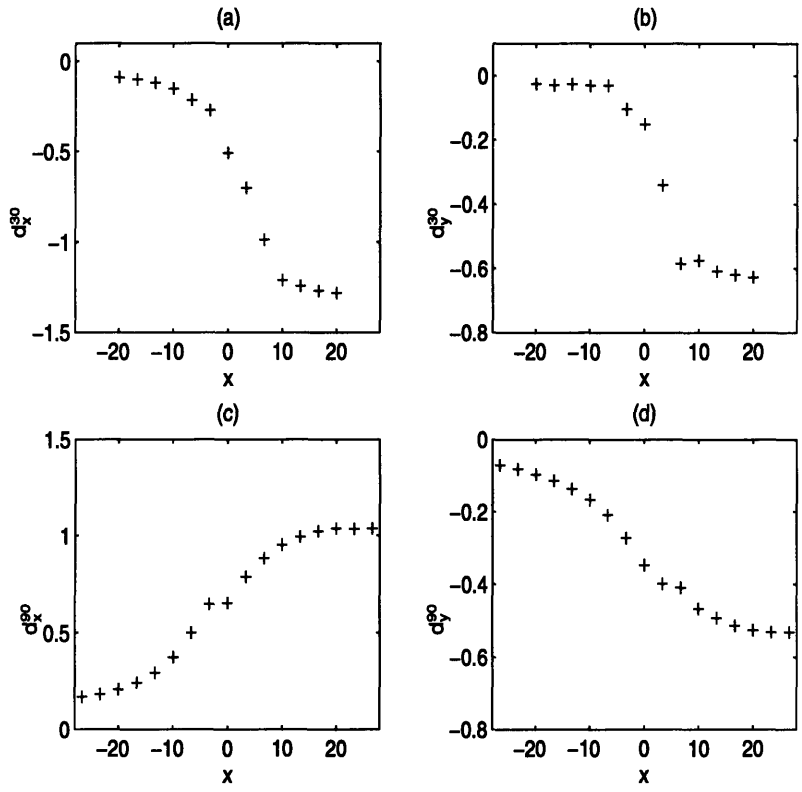

Figure 6-4: Defects formed in dislocation 1 in the 30^o-30^o (a,b) and 90^o-90^o (c,d) intersection processes. In the present geometry, d_x and d_y give the in-plane and out-of-plane components respectively. Distances are given in Angstrons.

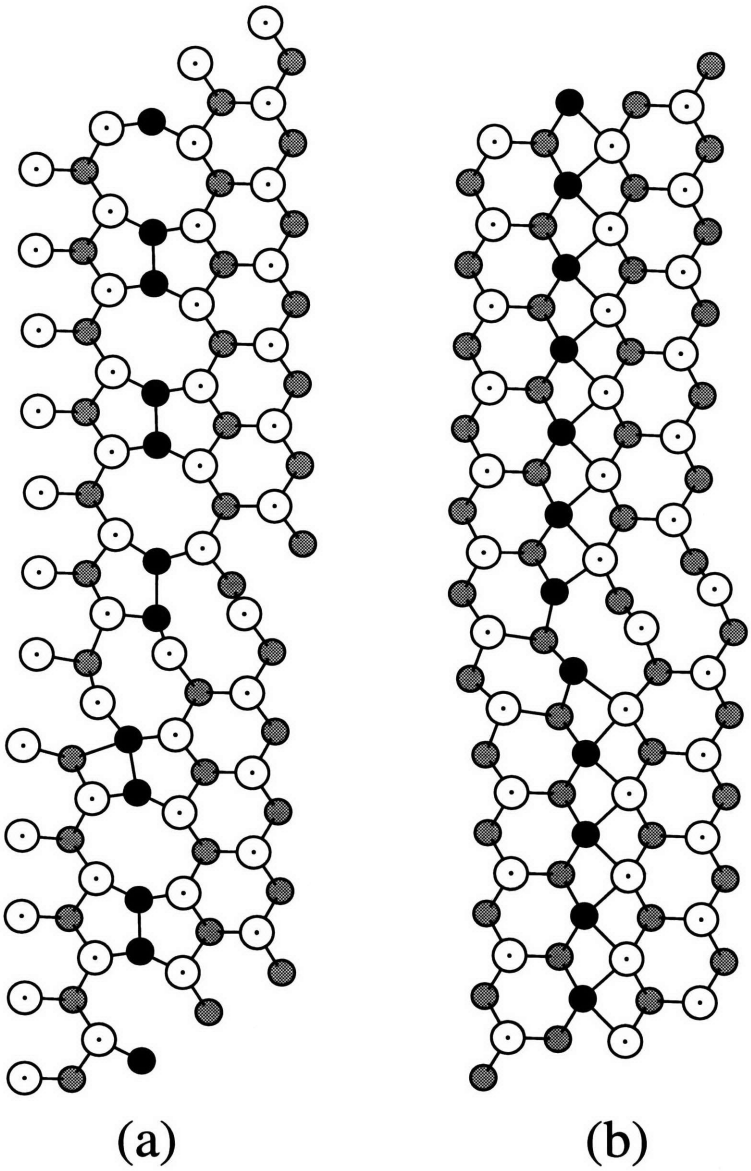

Figure 6-5: Final configurations for (a) the 30^o-30^o and (b) the 90^o-90^o intersection processes in dislocation 1 in glide plane 1. The core atoms are represented in black.

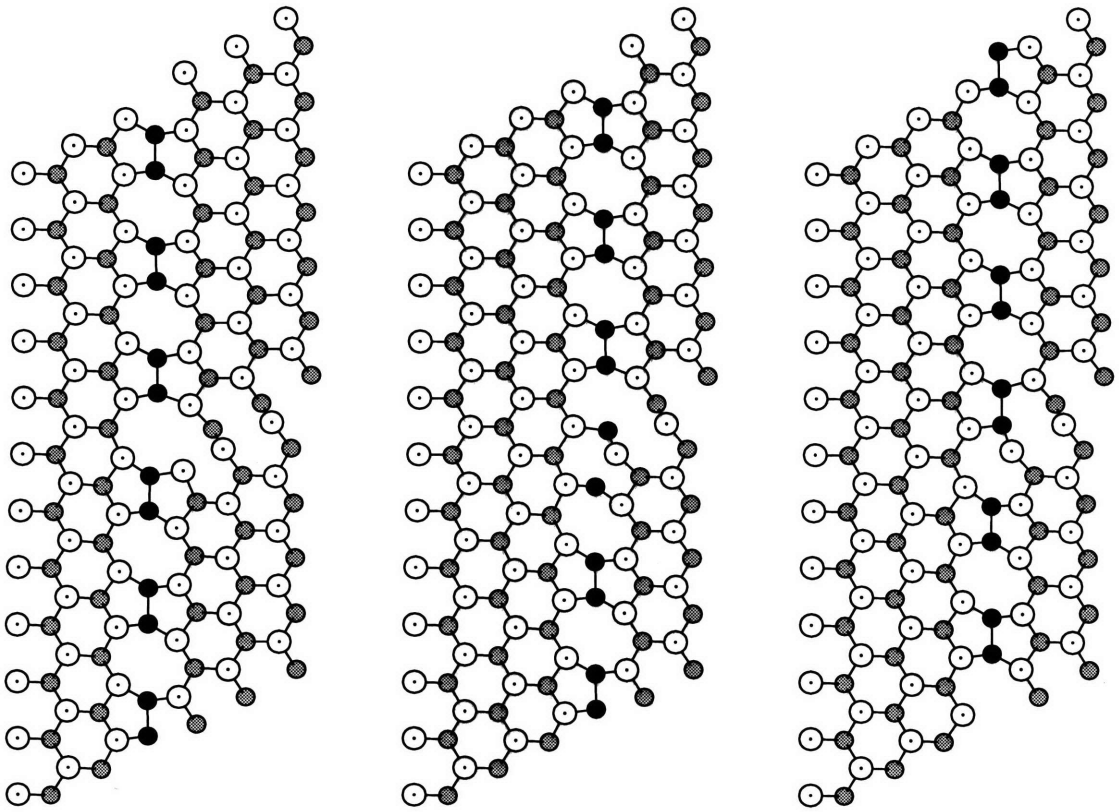

Figure 6-6: The 30^o-30^o interaction process as two dislocations just intersect. The figure shows the evolution of the dislocation core of dislocation 1 (a) before and (b,c) after intersection with dislocation 2 in another glide plane. Two different final results are shown, (b) the defect is formed by breaking a reconstruction bond and (c) the defect is formed between two different reconstruction bonds. The core atoms are represented in black.

Chapter 7

Conclusions

In this work, we have developed a theoretical analysis of the properties of dislocations in semiconductors. The atomistic picture of the dislocation interactions was brought about as a result of atomistic simulations using empirical interatomic potentials combined with energy minimization methods. The major results from this study are the following. We developed a new empirical potential for silicon which was applied throughout the analysis of core properties of dislocations. The study of the mechanisms of dislocation mobility revealed the importance of the core reconstruction effects. We also explored the mechanisms of core-core interaction in dislocation intersection.

A first requirement to study dislocations in silicon at the atomistic level is to have a reliable interatomic potential. Among the available empirical models for silicon, no model has been reliable enough for the several important structures related to dislocation interactions, such as reconstruction, core defects (APD), and kinks. Therefore, we have developed our own empirical model for silicon, which represents a considerable improvement over the existing models in describing dislocation properties.

The empirical potential for silicon was developed using a combination of a theoretically motivated functional form and a specific database of *ab initio* calculations. The functional form depicts the bonding using coordination dependent functions. Therefore, the functional form describes the chemical and physical trends of bonding as

coordination changes, for example, as the material follows a phase transition from covalent to metallic bonding. In the two-body interaction, we used a SW-like functional form, but we introduced a bond-order term in the attractive interaction. As coordination increases, the attractive term is screened out. In the three-body interaction, we incorporated several coordination dependent functions to stabilize the structure for different coordinations. The model represents a considerable improvement over the existing models in describing local structure. Specifically, this model gives a superior description of mechanical properties and point defects in Si.

For core properties of dislocations, the new empirical potential provided a reasonable description of the core reconstructions: it predicted the correct reconstruction for both 90°- and 30°-partials and the reconstruction energies are in excellent agreement with the *ab initio* results. The bond stretching and angle deformations are also in good agreement with *ab initio* results, pointing to the fact that this model not only predicts energies but also describes well the local bonding configurations of the atoms in the core. Overall, this new model provides a considerable improvement over existing empirical models in describing core properties of dislocations.

We studied dislocation mobility by the mechanisms of kink formation and propagation. The mechanisms of kink motion in silicon are unveiled by the calculation of kink formation and migration energies. We showed that there is a significant additional resistance to dislocation motion in Si associated with the core reconstruction. Also, dislocation motion is found to be a complex process which involves not only formation of simple kinks, but also a series of defect formations, motions, annihilations, and various other defect reactions, which all take place simultaneously and may even compete with each other. Furthermore, the core reconstruction plays a central role in dislocation motion, in that formation and migration energies of kinks are function, to a large extent, of the reconstruction energy.

Kink formation and migration mechanisms involve breaking the reconstruction bonds in the core. If these reconstruction bonds are strong, as they are in Si, the net reconstruction contribution to the resistance to dislocation motion is large. We conclude that, even though the reconstruction energy is a static parameter, it is directly

related to dislocation mobility in semiconductors. This is revealed by the considerable changes in the kink formation and migration energies depending on the reconstructed state of the dislocation. Furthermore, since reconstructions in the partial dislocation cores in zincblende materials require that bonds be formed between anions or between cations, reconstruction should be weakened and eventually suppressed by increasing bond ionicity on going from IV-IV to III-V and further to II-VI semiconductors. This effect may be responsible for the significant variations in dislocation mobility for the zincblende semiconductor family. It was also observed that regardless of the strength of core reconstruction in a given material, core excitations with dangling bonds participate actively in dislocation motions. These excitations, such as APD centers, form complexes with kinks, which change considerably the kinetics of that kink.

The effects of the core properties in the mechanisms of dislocation intersection were also studied in full atomistic detail. Again, the core reconstruction plays an important role in increasing the resistance of the dislocations to intersect. The formation of jogs in the dislocation, resulting from the intersection, is typically a consequnce of core-core interactions. As the intersecting dislocations approach each other, the atomic deformations are the result of large stress fields of core-core interactions. This is revealed by the fact that the jogs start to form when there is overlap between the cores of the intersecting dislocations, even before the dislocations geometrically intersect each other.

Although there are concerns about the validity of the Peierls-Nabarro (PN) model for narrow dislocations, the atomistic picture of intersection in Si is consistent with the basic assumption of the PN model, i.e. that dislocations can be represented by distributed dislocation densities spread in their respective glide planes. Therefore, it is of interest to attempt to develop a continuum PN-like approach for dislocation intersection.

The energetics involved in the intersection of two dislocations is strongly dependent on the details of atomistic structure in the core, such as core reconstruction, which can be addressed only within a fully atomistic approach. Therefore, the new intersection mechanisms unveiled here give additional complexity to picture of dislo-

cation mobility, beyond the existing picture of mobility involving kink formation and migration.

Although we showed that the mechanisms of dislocation motion are complex, it is still a considerable simplification of the more realistic scenario. A more complete, and considerably more complex, picture should include interaction of the dislocation core with intrinsic defects [112], and dopants. The study of dislocation motion was performed with energy minimization methods, therefore temperature effects (such as entropy) were never considered. It would be desirable to extend such work to compute the free energy of all these mechanisms, therefore, presenting a more realistic picture.

This work, therefore, has unveiled some important mechanisms involved in dislocation motion in silicon. Although this study was performed using empirical potentials, it already gives some insights in to the core effects in dislocation motion. On the other hand, it is desirable to describe these mechanisms using quantum mechanical calculations, therefore also including electronic effects involved.

Appendix A

Force Expression for the New Empirical Potential

A.1 Energy Calculation

The interatomic potential presented in chapter 4 is describe as an expansion of two- and three-body terms

$$E = \sum_{\substack{i,j \\ (i \neq j)}} V_2(ij, Z_i) + \sum_{\substack{i,j,k \\ (i<j<k)}} V_3(ijk, Z_i) \quad , \tag{A.1}$$

where $V_2(ij, Z_i)$ is the interaction between atoms i and j, $V_3(ijk, Z_i)$ is the interaction between atoms i, j and k centered at atom i (with coordination Z_i).

The coordination at an atom i is defined by:

$$Z_i = \sum_m f(r_{im}) \quad , \tag{A.2}$$

where $f(r_{im})$ is the individual contribution of atom m to the coordination of atom i.

This individual contribution to Z of each neighbor is given by:

$$f(r) = \begin{cases} 1 & \text{if } r < c \\ e^{\frac{\alpha}{1-1/x^3}} & \text{if } c < r < b \\ 0 & \text{if } r > b \end{cases} , \tag{A.3}$$

where $x = \frac{(r-c)}{(b-c)}$.

The two body interaction is given by:

$$V_2(ij, Z_i) = A\left[\left(\frac{B}{r_{ij}}\right)^{\rho} - e^{-\beta Z_i^2}\right] e^{\sigma/(r_{ij}-a)} \tag{A.4}$$

and the three body interaction is given by:

$$V_3(ijk, Z_i) = \lambda e^{\gamma/(r_{ij}-b)} e^{\gamma/(r_{ik}-b)} \left[1 - e^{-Q(Z_i)(\cos(\theta_{jik})+\tau(Z_i))^2}\right] \tag{A.5}$$

The coordination dependence in the three body interactions is introduced through the functions $\tau(Z)$ and $Q(Z)$.

$$\tau(Z) = u_1 + u_2(u_3 e^{-u_4 Z} - e^{-2u_4 Z}) , \tag{A.6}$$

and

$$Q(Z) = Q_0 e^{-\mu Z} . \tag{A.7}$$

Table 4.3 gives the parameters for this model.

A.2 Force Calculation

The force on an atom p is given by the gradient of the potential energy with respect to $\underline{r}_p$:

$$\underline{F}_p = -\nabla_p E \tag{A.8}$$

$$= -\sum_{\substack{i,j \\ (i \neq j)}} \nabla_p V_2(ij, Z_i) - \sum_{\substack{i,j,k \\ (i<j<k)}} \nabla_p V_3(ijk, Z_i) \tag{A.9}$$

$$= \sum_{\substack{i,j \\ (i \neq j)}} \underline{F}_{pj} + \sum_{\substack{i,j,k \\ (i<j<k)}} \underline{F}_{pjk} \tag{A.10}$$

To compute the force, consider the term $V_2(ij, Z_i)$ as the interatomic interaction between atoms i and j with coordination Z_i. The two-body force on atom i is written as:

$$\underline{F}_{pj} = -\frac{\partial V_2(ij, Z_i)}{\partial r_{pj}} \frac{\partial r_{pj}}{\partial \underline{r}_p} \tag{A.11}$$

For a given pair of atoms i and j centered at atom i (with coordination Z_i), the force in each atom is given as: On atom i, the force is:

$$\underline{f}_i = A[\rho \frac{B^\rho}{r_i j^{\rho+1}} + \frac{\sigma}{(r_{ij}-a)^2}(\frac{B^\rho}{r_{ij}^\rho} - e^{-\beta Z_i^2})] \exp[\sigma/(r_{ij}-a)]\underline{n}_{ij}$$
$$-2A\beta Z_i e^{-\beta Z_i^2} \sum_m f'(r_{im})\underline{n}_{im} \exp[\sigma/(r_{ij}-a)]$$

where the sum is over all m neighbors of atom i that contribute to Z_i and $\underline{n}_{ij} = \frac{\underline{r}_{ij}}{r_{ij}}$.

On atom j, it is: $p = j$

$$\underline{f}_j = A[\rho \frac{B^\rho}{r_i j^{\rho+1}} + \frac{\sigma}{(r_{ij}-a)^2}(\frac{B^\rho}{r_{ij}^\rho} - e^{-\beta Z_i^2})] \exp[\sigma/(r_{ij}-a)]\underline{n}_{ij}$$
$$-2A\beta Z_i e^{-\beta Z_i^2} f'(r_{ij})\underline{n}_{ij} \exp[\sigma/(r_{ij}-a)]$$

and for $l \neq i, l \neq j$ which is a neighbor of atom i:

$$\underline{f}_l = -2A\beta Z_i e^{-\beta Z_i^2} f'(r_{il}) \underline{n}_{il} \exp[\sigma/(r_{ij} - a)]$$

The three body force F_{pjk} is given as follow. For atoms i, j, k, the term centered in atom i gives the contribution:

Consider $h = V_3(i, j, k, Z_i)$ The force on atom i is given by:

$$\begin{aligned} \underline{f}_i &= \left[\frac{\partial h}{\partial r_{ij}} + \left(\frac{1}{r_{ik}} - \frac{\mu_i}{r_{ij}} \frac{\partial h}{\partial \mu_i}\right)\right] \underline{n}_{ij} \\ &+ \left[\frac{\partial h}{\partial r_{ik}} + \left(\frac{1}{r_{ij}} - \frac{\mu_i}{r_{ik}} \frac{\partial h}{\partial \mu_i}\right)\right] \underline{n}_{ik} - \frac{\partial h}{\partial Z_i} \sum_m f'(r_{im}) \underline{n}_{im} \end{aligned}$$

where the sum is over all m neighbors of atom i.

The force on atom j is given by:

$$\underline{f}_j = \left[-\frac{\partial h}{\partial r_{ij}} + \frac{\mu_i}{r_{ij}} \frac{\partial h}{\partial \mu_i}\right] \underline{n}_{ij} - \frac{\partial h}{\partial \mu_i} \frac{1}{r_{ij}} \underline{n}_{ik} - \frac{\partial h}{\partial Z_i} f'(r_{ij}) \underline{n}_{ij}$$

The force on atom k is given by:

$$\underline{f}_k = \left[-\frac{\partial h}{\partial r_{ik}} + \frac{\mu_i}{r_{ij}} \frac{\partial h}{\partial \mu_i}\right] \underline{n}_{ik} - \frac{\partial h}{\partial \mu_i} \frac{1}{r_{ik}} \underline{n}_{ij} - \frac{\partial h}{\partial Z_i} f'(r_{ik}) \underline{n}_{ik}$$

Now, for an atom $l \neq i$, $l \neq j$, $l \neq k$, the force is given by:

$$f_l = -\frac{\partial h}{\partial Z_i} f'(r_{il}) \underline{n}_{il}$$

Bibliography

[1] D.J.Eaglesham, MRS Bulletin, Vol. 19, num. 12, pag. 57 (1994).

[2] *Polycrystalline Semiconductors*, Eds. J. H. Werner and H.P. Strunk (Springer Verlag, Berlin, 1991).

[3] H. Alexander and H. Teichler, in *Materials Science and Technology*, Eds. R. W. Cahn, P. Haasen, and E. J. Kramer, Vol. 4 (VCH Weinheim, 1991), pag. 249-319.

[4] H. Alexander, in *Dislocation in Solids*, edited by F. R. N. Nabarro, Vol 7, (North Holland, Amsterdam, 1986), p. 115.

[5] J. R. Chelikowsky and J. C. H. Spence, Phys. Rev. B **30**, 694 (1984).

[6] M. S. Duesbery, B. Joos, D. J. Michel, Phys. Rev. B **43**, 5143 (1991).

[7] V. V. Bulatov, S. Yip, and A. S. Argon, Phil. Mag. A **72**, 453 (1995).

[8] G. H. Gilmer, Comp. Mat. Sci. **2**, 49 (1994).

[9] M. C. Payne, M. P. Teter, D. C. Allan, T. A. Arias, and J. D. Joannopoulos, Rev. Mod. Phys. **64**, 1045 (1992).

[10] P. Hirth and J. Lothe, *Theory of Dislocations*, 2nd. ed. (Wiley, 1982).

[11] N. W. Ashcroft, N. D. Mermin, *Solid State Physics*, (Saunders, Pliladelphia, 1976).

[12] E. Orowan, Z. Phys. **89**, 605, 634 (1934); M. Polanyi, Z. Phys. **89**, 660 (1934); G. I. Taylor, Proc. Roy. Soc. A **145**, 362 (1934).

[13] T. Suzuki, S. Takeuchi, and H. Yoshinaga, in *Dislocation Dynamics and Plasticity* (Springer, New York, 1991), p. 99.

[14] E. Depraetère, D. Vignaud, J. L. Farvacque, and B. Sieber, Phil. Mag. A **61**, 893 (1990).

[15] B. Joós, Q. Ren, and M. S. Duesbery, Phys. Rev. B **50**, 5890 (1994).

[16] J. M. Haile, *Molecular Dynamics Simulation - Elementary Methods* (John Wiley & Sons, New York, 1992).

[17] E. H. Yoffe, Phil. Mag. **6** 1147 (1961); P. P. Groves and D. J. Bacon, Phil. Mag. **22**, 83 (1970); and Y. Maurissen and L. Cappela, Phil. Mag. **29**, 1227 (1974).

[18] J. R. K. Bigger *et. al.*, Phys. Rev. Lett. **69**, 2224 (1992).

[19] L. B. Hansen, K. Stokbro, B. I. Lundqvist, K. W. Jacobsen, and D. M. Deaven, Phys. Rev. Lett. **75**, 4444 (1995).

[20] H. C. Andersen, J. Chem. Phys. **72**, 2384 (1980).

[21] S. Nosé, Mol. Phys. **52**, 255 (19984); J. Chem. Phys. **81**, 511 (1984).

[22] M. Parrinello and A. Rahman, J. Appl. Phys. **52**, 7182 (1981).

[23] J. R. Ray and A. Rahman, J. Chem. Phys. **80**, 4423 (1984).

[24] J. R. Ray, Computer Reports **8** 109 (1988).

[25] W. Press, B. Flannery, S. A. Teukolsky, and W. Vetterling, *Numerical Recipes*, (Cambridge University Press, Cambridge, 1986).

[26] for example J. Huang, M. Meyer, and V. Pontikis, Phys. Rev. Lett. **63**, 628 (1989); and Phil. Mag. A **63**, 1149 (1991).

[27] M. S. Duesbery, D. J. Michel, and B. Joos, Mat. Res. Soc, Symp. Proc. **163**, 941 (1990).

[28] E. A. Carter, G. Cicotti, J. T. Hynes, and R. Kapral, Chem. Phys. Lett. **156**, 472 (1989).

[29] S. Kirkpatrick, C. D. Gelatt, and M. P. Vecchi, Science **220**, 671 (1983); and S. Kirkpatrick, J. Stat. Phys. **34**, 975 (1984).

[30] S. Bell and J. S. Crighton, J. Chem. Phys. **80**, 2464 (1984).

[31] R. Elber and M. Karplus, Chem. Phys. Lett. **139**, 375 (1987).

[32] M. Nastar, V. V. Bulatov, and S. Yip, Phys. Rev. B **53**, 13521 (1995).

[33] V. V. Bulatov, M. Nastar, J. F. Justo, and S. Yip, to be published.

[34] C. R. A. Catlow and W. C. Mackrodt, *Computer Simulation of Solids* (Springer, New York, 1982).

[35] M. S. Daw, in *Many Body Interactions in Solids*, Ed. R. M. Nieminen, M. J. Puska, and M. J. Manninen (Springer-Verlag, Berlin, 1990), Vol. 48, p. 48.

[36] H. Balamane, T. Halicioglu, and W. A. Tiler, Phys. Rev. B **46**, 2250 (1992).

[37] S. J. Cook and P. Clancy, Phys. Rev. B **47**, 7686 (1993).

[38] F. H. Stillinger and T. A. Weber, Phys. Rev. B **31**, 5262 (1985).

[39] J. Tersoff, Phys. Rev. Lett. **56**, 632 (1986).

[40] J. Tersoff, Phys. Rev. B **37**, 6991 (1988).

[41] J. Tersoff, Phys. Rev. B **38**, 9902 (1988).

[42] X. P. Li, G. Chen, P. B. Allen, and J. Q. Broughton, Phys. Rev. B **38**, 3331 (1988).

[43] I. P. Batra, F. F. Abraham, and S. Ciraci, Phys. Rev. B **35**, 9552 (1987).

[44] J. Q. Broughton and X. P. Li, Phys. Rev. B **35**, 9120 (1987).

[45] P. C. Kelires and J. Tersoff, Phys. Rev. Lett. **61**, 562 (1988).

[46] W.D. Luedtke and U. Landman, Phys. Rev. B **37**, 4656 (1988); Phys. Rev. B **40**, 1164 (1989).

[47] K.E. Khor and S. Das Sarma, Phys. Rev. B **36**, 7733 (1987).

[48] F. F. Abraham and I. Batra, Surf. Sci **163**, L752 (1985).

[49] X. P. Li, G. Chen, P. B. Allen, and J. Q. Broughton, Phys. Rev. B **38**, 3331 (1988).

[50] T. W. Poon, S. Yip, P. S. Ho, and F. F. Abraham, Phys. Rev. Lett. **65**, 2161 (1990).

[51] U. Landeman, W. D. Luedtke, M. W. Ribarsky, R. N. Barnett, and C. L. Cleveland, Phys. Rev. B **37**, 4637 (1988); Phys. Rev. B **37**, 4647 (1988).

[52] E. T. Gawlinski and J. D. Gunton, Phys. Rev. B **36**, 4774 (1987).

[53] K. Ding abd H. C. Andersen, Phys. Rev. B **34**, 6987 (1986).

[54] Z. Q. Wang and D. Stroud, Phys. Rev. B **38**, 1384 (1988).

[55] Z. Q. Wang and D. Stroud, Phys. Rev. B **42**, 5353 (1990).

[56] Z. Q. Wang,D. Stroud, and A. J. Markworth, Phys. Rev. B **40**, 3129 (1989).

[57] F. H. Stillinger and T. A. Weber, Phys. Rev. Lett. **62**, 2144 (1989).

[58] Z. Jiang and R. A. Brown, Phys. Rev. Lett. **74**, 2046 (1995); and Chem. Eng. Sci. **49**, 2991 (1994).

[59] G. C. Abell, Phys. Rev. B **31**, 6184 (1985).

[60] B. C. Bolding and H. C. Andersen, Phys. Rev. B **41**, 10568 (1990).

[61] K. Mizushima, S. Yip, and E. Kaxiras, Phys. Rev B **50**, 14952 (1994).

[62] L. J. Porter, S. Yip, M. Yamaguchi, H. Kaburaki, and M. Tang, to apear at J. Appl. Phys. .

[63] J. Tersoff, Phys. Rev. Lett. **61**, 2879 (1988).

[64] J. Tersoff, Phys. Rev. B **39**, 5566 (1989).

[65] M. Tang, Phys. Rev. Lett **75**, 2738 (1995).

[66] M. V. Ramana Murty and H. A. Atwater, Phys. Rev. B **51**, 4889 (1995).

[67] K. E. Khor and S. Das Sarma, Phys. Rev. B **38**, 3318 (1988); Phys. Rev. B **39**, 1188 (1989); Phys. Rev. B **40**, 1319 (1989).

[68] S. Kodiyalam, K. E. Khor, N. C. Bartelt, E. D. Williams, and S. Das Sarma, Phys. Rev. B **51**, 5200 (1995).

[69] E. Kaxiras and K. C. Pandey, Phys. Rev. B **38**, 12736 (1988).

[70] K. C. Pandey, Phys. Rev. Lett. **57**, 2287 (1986).

[71] A. Antonelli, S. Ismail-Beigi, E. Kaxiras, and K. C. Pandey, Phys. Rev. B **53**, 1310 (1996).

[72] A. D. Mistriotis, N. Flytzanis, and S. C. Farantos, Phys. Rev. B **39**, 1212 (1989).

[73] M. P. Allen and D. J. Tildesley, *computer Simulation of Liquids* (Clarendon Press, Oxford, 1987).

[74] M. Z. Bazant and E. Kaxiras, Phys. Rev. Lett. **77**, 4370 (1996).

[75] A. E. Carlssom, P. A. Fedders, and C. W. Myles, Phys. Rev. B **41**, 1247 (1990).

[76] S. Ismail-Beigi and E. Kaxiras, Harvard University, Hoopes Prize for Undergraduate Research Paper (1993).

[77] R. Biswas and D. R. Hamann, Phys. Rev. Lett. **55**, 2001 (1985).

[78] E. Kaxiras and M. S. Duesbery, Phys. Rev. Lett. **70**, 3752 (1993).

[79] G. Simmons and H. Wang, *Single Crystal Elastic Constants and Calculated Aggregate Properties: A Handbook* (MIT, Cambridge, MA, 1971).

[80] C. Z. Wang, C. T. Chan, and K. M. Ho, Phys. Rev. B **39**, 8586 (1989).

[81] D. C. Wallace, *Thermodynamics of Crystals* (Wiley, New York, 1972).

[82] J. Wang, S. Yip, S. R. Phillpot, and D. Wolf, Phys. Rev. Lett. **71**, 4182 (1993).

[83] J. P. Hansen and I. R. McDonald, *Theory of Simple Liquids* (Academic, London, 1976).

[84] L. J. Porter, J. F. Justo, and S. Yip, to be published.

[85] C. H. Xu, C. Z. Wang, C. T. Chan, and K. M. Ho, Phys. Rev. B **43**, 5024 (1991).

[86] H. Ibach, Phys. Status Solidi **31**, 625 (1969).

[87] K. G. Lyon, G. L. Salinger, C. A. Swenson, and G. K. White, J. Appl. Phys. **48**, 865 (1977).

[88] S. Wei, C. Li, and M. Y. Chou, Phys. Rev. B **50**, 14587 (1994).

[89] H. Teichler, in *Polycrystalline Semiconductors*, ed. J. Wener, H. J. Möller, and H. P. Strunk, Springer Proceedings in Physiscs, Vol. 35, 25 (1989).

[90] P. Flubacher, A. J. Leadbetter, and J. A. Morrison, Phil. Mag. **4**, 273 (1959).

[91] Y. M. Huang, J. C. H. Spence, and O. F. Sankey, Phys. Rev. Lett **74**, 3392 (1995).

[92] T. A. Arias and J. D. Joannopoulos, Phys. Rev. Lett. **73**, 680 (1994).

[93] R. W. Nunes, J. Bennetto, and D. Vanderbilt, Phys. Rev. Lett. **77**, 1516 (1996).

[94] U. Trinczek and H. Teichler, Phys. Sta. Sol. A **137**, 577 (1993).

[95] A. S. Nandedkar and J. Narayan, Phil. Mag. A **61**, 873 (1990).

[96] T. A. Arias, V. V. Bulatov, S. Yip, and A. S. Argon, to be published.

[97] I. Kwon, R. Biswas, C. Z. Wang, K. M. Ho, and C. M. Soukoulis, Phys. Rev. B **49**, 7242 (1994).

[98] P. E. Blöchl, E. Smargiassi, R. Car, D. B. Laks, W. Andreoni, and S. T. Pantelides, Phys. Rev. Lett. **70**, 2435 (1993).

[99] C. Z. Wang, C. T. Chan, and K. M. Ho, Phys. Rev. B **42**, 11276 (1990).

[100] M. S. Duesbery, D. J. Michel, E. Kaxiras, and B. Joos, Mat. Res. Soc. Symp. Proc. **209**, 125 (1991).

[101] M. S. Duesbery and G. Y. Richardson, CRC Crit. Rev. Solid State Mater. Sci. **17**, 1 (1991).

[102] H. Suzuki, in *Dislocation Dynamics*, Eds. A. R. Rosenfeld, G. T. Hahn, A. L. Bement, and R. I. Jaffe (McGraw-Hill, New York, 1968), pag. 679.

[103] W. D. Nix, Metall. Trans. **20A**, 2117 (1989).

[104] B. Y. Farber, Y. L. Iunin, V. I. Nikitenko, Phys. Stat. Sol. A **97**, 469 (1986).

[105] H. R. Kolar, J. C. H. Spence, and H. Alexander, Phys. Rev. Lett. **77**, 4031 (1996).

[106] C. Barret, W. Nix, and A. Tetelman, *The Principles of Engineering Materials*, 1st. ed. (Prentice-Hall, 1973).

[107] J. F. Justo, V. V. Bulatov, and S. Yip, to appear at *Scripta Materiallia.*

[108] W. T. Read, in *Dislocations in Crystals*, (McGraw Hill, 1953) p. 80.

[109] J. Hornstra, Acta Met. **10**, 987 (1962).

[110] Y. M. Juan and E. Kaxiras (unpublished).

[111] R. Miller and R. Phillips, Phil. Mag. A **73**, 803 (1996).

[112] R. W. Balluffi and A. V. Granato, in *Dislocations in Solids*, Ed. F. R. N. Nabarro (North-Holland, Amsterdan, 1979), vol. 4, pag. 1 .

[113] A. S. Argon, in *Physical Metallurgy*, ed. R. W. Cahn and P. Haasen (Nort-Holland, Amsterdam, 1996), pag. 1877.